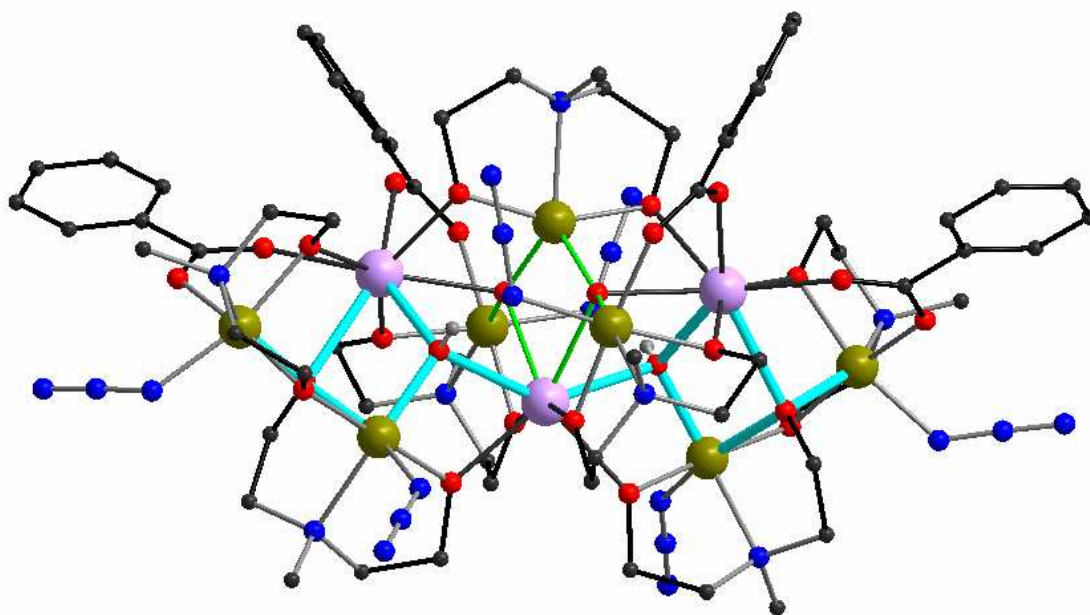


Synthesis and Characterisation of $4f$ and $3d-4f$ Molecular based Magnets

DISSERTATION

Von

GHULAM ABBAS



Karlsruhe im April 2009

Synthesis and Characterisation of $4f$ and $3d-4f$ Molecular based Magnets

Zur Erlangung des akademischen Grades eines

DOKTORS DER NATURWISSENSCHAFTEN

(Dr. rer. nat.)

der Fakultät für Chemie und Biowissenschaften der
Universität Karlsruhe (TH)
angenommene

DISSERTATION

Von

GHULAM ABBAS

M.Phil

aus **SIALKOT, PAKISTAN**

Dekan: Prof. Dr. Stephan Bräse

Referent: Prof. Dr. Annie K. Powell

Korreferent: Dr. Andreas Schnepf

Tag der mündlichen Prüfung: 24 April 2009

*My wealth set sons and brethren part. Some things they cannot share: my work
well done, my noble heart — these are mine own to wear.*

Abu Musa Jabir ibn Hayyan al azdi

To

Prof. Dr. Rashid Iqbal (Late)

*Moqaam ay guftgoc kia hai agar mein chemia gar hoon
Yehi soz ay nafas hai aur meri chemia kia hai
(Iqbal)*

Die vorliegende Arbeit wurde in der Zeit von Jan.2006 bis April 2009 am Institut für Anorganische Chemie der Universität Karlsruhe (TH) unter Anleitung von Prof. Dr. Annie K. Powell angefertigt.

Contents

Chapter 1	Introduction	1
1.1	From magnet to Single Molecule Magnet (SMM)	1
1.2	Introduction to magnetic susceptibility	2
1.2.1	Basic theoretical approach of magnetism	2
1.3	Types of magnetic behaviour	3
1.3.1	Diamagnetism	4
1.3.2	Paramagnetism	4
1.3.3	Ferromagnetism	4
1.3.4	Antiferromagnetism	5
1.3.5	Ferrimagnetism	5
1.4	Determination of magnetic behaviour	5
1.4.1	Curie-Weiss paramagnetism	6
1.5	Single Molecule Magnets (SMMs)	8
1.6	Synthetic strategies for making polynuclear complexes	13
1.7	Introduction to iron chemistry	14
1.7.1	An octanuclear Fe(III) cluster	15
1.7.2	[Fe ₁₉ (methedi) ₁₀ (OH) ₄ O ₆ (H ₂ O) ₁₂](NO ₃), the largest nuclearity and spin Fe SMM	16
1.7.3	[Fe ₄ (OMe) ₆ (dpm) ₆], the smallest nuclearity Fe SMM	16
1.8	Introduction to rare-earth metal chemistry	17
1.8.1	A mononuclear compound showing SMM or single ion magnetisation behaviour	18
1.8.2	The dysprosium triangles [Dy ₃ (μ ₃ -OH) ₂ L ₃ Cl(H ₂ O) ₅]Cl ₅ ·19H ₂ O	19
1.9	Introduction to 3d-4f (Fe-Ln) complexes	20
1.9.1	[Fe ₂ Ln ₂ (OH) ₂ (teaH) ₂ (O ₂ CPh) ₆], A tetranuclear SMM	21
1.9.2	A binuclear single molecule magnet (SMM)	21
1.10	Ligand selection	22
1.11	Co-ligand selection	23
1.12	Thesis overview	24
Chapter 2	Research objectives	25

Chapter 3	Structure and magnetic properties of lanthanide aggregates	27
3.1	Introduction	27
3.2	Structure and magnetic properties of $[\text{Ln}_2(\text{mdeaH}_2)(\text{piv})_6]$	27
3.2.1	Structure of $[\text{Ln}_2(\text{mdeaH}_2)(\text{piv})_6]$ (1-6).	28
3.2.2	Magnetic properties of $[\text{Ln}_2(\text{mdeaH}_2)(\text{piv})_6]$ (Compounds 1-6).	31
3.3	Structure and magnetic properties of $[\text{Ln}_4(\mu_3\text{-OH})_2(\text{mdeaH})_2(\text{piv})_8]$ (7-11).	34
3.3.1	Structure of $[\text{Dy}_4(\mu_3\text{-OH})_2(\text{mdeaH})_2(\text{piv})_8]$ (8)	34
3.3.2	Magnetic properties of $[\text{Ln}_4(\mu_3\text{-OH})_2(\text{mdeaH})_2(\text{piv})_8]$ (Ln = Tb, Dy Ho, Er, Tm) (7-11).	37
3.4	Structure and magnetic properties of $[\text{Ln}_4(\text{mdea})_2(\text{mdeaH})_2(\text{PhCO}_2)_6]$	43
3.4.1	Structure of $[\text{Dy}_4(\text{mdea})_2(\text{mdeaH})_2(\text{PhCO}_2)_6] \cdot 4\text{MeCN}$ (13a)	45
3.4.2	Magnetic properties of $[\text{Ln}_4(\text{mdea})_2(\text{mdeaH})_2(\text{PhCO}_2)_{6-x}(\text{NO}_3)_x]$ (12-15)	47
3.5	Conclusion	54
Chapter 4	Structure and magnetic properties of iron-lanthanide aggregates	56
4.1	Introduction	56
4.2	Structure and magnetic properties of decanuclear complexes (16-22)	57
4.2.1	Structure of $[\text{Dy}_3^{\text{III}}\text{Fe}_7^{\text{III}}(\mu_4\text{-O})_2(\mu_3\text{-OH})_2(\text{N}_3)_6(\text{mdea})_7(\text{PhCO}_2)_4] \cdot 7\text{MeOH}$ (18)	57
4.2.2	Magnetic properties of $[\text{Ln}_3^{\text{III}}\text{Fe}_7^{\text{III}}(\mu_4\text{-O})_2(\mu_3\text{-OH})_2(\text{N}_3)_6(\text{mdea})_7(\text{PhCO}_2)_4]$ (Ln = Gd, Tb, Dy, Er) (compounds 16-19)	60
4.2.3	Structure of $[\text{Tm}_4^{\text{III}}\text{Fe}_6^{\text{III}}(\mu_3\text{-OH})_4(\text{mdea})_6(\text{mdeaH})_2(\text{N}_3)_8(\text{PhCO}_2)_4(\text{OH}_2)_2] \cdot 4\text{MeCN}$ (22)	69
4.2.4	Magnetic properties of $[\text{Ln}_4^{\text{III}}\text{Fe}_6^{\text{III}}(\mu_3\text{OH})_4(\text{mdea})_6(\text{mdeaH})_2(\text{N}_3)_8(\text{PhCO}_2)_4(\text{H}_2\text{O})_2] \cdot 4\text{MeCN}$ (Ln = Er, Ho, Tm) (20-22)	72
4.3	Structure and magnetic properties $[\text{Er}^{\text{III}}\text{Fe}_4^{\text{III}}(\mu_3\text{-O})(\text{mdea})_3(\text{mdeaH})(\text{O}_2\text{CPh})_2(\text{N}_3)_4] \cdot 2.5 \cdot \text{MeCN}$ (23)	75
4.3.1	Structure of $[\text{Er}^{\text{III}}\text{Fe}_4^{\text{III}}(\mu_4\text{-O})(\text{mdea})_3(\text{mdeaH})(\text{O}_2\text{CPh})_2(\text{N}_3)_4]$	

	·2.5MeCN (23)	75
4.3.2	Magnetic properties of [Er ^{III} Fe ₄ ^{III} (μ ₃ -O)(mdea) ₃ (mdeaH)(O ₂ CPh) ₂ (N ₃) ₄]·2.5MeCN (23)	77
4.4	Conclusion	80
Chapter 5	Summary	82
Chapter 6	Experimental	86
6.1	Preparation of inorganic materials	86
6.1.1	Preparation of [La ₂ (mdeaH ₂)(Piv) ₆] (1)	82
6.1.2	Preparation of [Ce ₂ (mdeaH ₂)(Piv) ₆] (2)	86
6.1.3	Preparation of [Pr ₂ (mdeaH ₂)(Piv) ₆] (3)	86
6.1.4	Preparation of [Nd ₂ (mdeaH ₂)(Piv) ₆] (4)	87
6.1.5	Preparation of [Sm ₂ (mdeaH ₂)(Piv) ₆] (5)	87
6.1.6	Preparation of [Gd ₂ (mdeaH ₂)(Piv) ₆] (6)	87
6.1.7	Preparation of [Tb ₄ ^{III} (μ ₃ -OH) ₂ (mdeaH) ₂ (piv) ₈] (7)	88
6.1.8	Preparation of [Dy ₄ (μ ₃ -OH) ₂ (mdeaH) ₂ (piv) ₈] (8)	88
6.1.9	Preparation of [Ho ₄ (μ ₃ -OH) ₂ (mdeaH) ₂ (piv) ₈] (9)	88
6.1.10	Preparation of [Er ₄ (μ ₃ -OH) ₂ (mdeaH) ₂ (piv) ₈] (10)	89
6.1.11	Preparation of [Tm ₄ (μ ₃ -OH) ₂ (mdeaH) ₂ (piv) ₈] (11)	89
6.1.12	Preparation of [Tb ₄ (mdea) ₂ (mdeaH) ₂ (PhCO ₂) _{4.5} (NO ₃) _{1.5}] (12)	89
6.1.13	Preparation of [Dy ₄ (mdea) ₂ (mdeaH) ₂ (PhCO ₂) ₆]·solv (13)	89
6.1.14	Preparation of [Ho ₄ (mdea) ₂ (mdeaH) ₂ (PhCO ₂) _{4.5} (NO ₃) _{1.5}] (14)	90
6.1.15	Preparation of [Er ₄ (mdea) ₂ (mdeaH) ₂ (PhCO ₂) ₆]·0.3(mdeaH ₂) ·1.7MeCN·1.4H ₂ O (15)	90
6.1.16	Preparation of [Gd ₃ Fe ₇ (μ ₄ -O) ₂ (μ ₃ -OH) ₂ (N ₃) ₆ (mdea) ₇ (PhCO ₂) ₄]·5MeCN (16)	90
6.1.17	Preparation of [Gd ₃ Fe ₇ (μ ₄ -O) ₂ (μ ₃ -OH) ₂ (N ₃) ₆ (mdea) ₇ (PhCO ₂) ₄] ·5MeCN (16)	91
6.1.18	Preparation of [Dy ₃ Fe ₇ (μ ₄ -O) ₂ (μ ₃ -OH) ₂ (N ₃) ₆ (mdea) ₇ (PhCO ₂) ₄] ·2H ₂ O·7MeOH (18)	91
6.1.19	Preparation of [Er ₃ ^{III} Fe ₇ ^{III} (μ ₄ -O) ₂ (μ ₃ -OH) ₂ (N ₃) ₆ (mdea) ₇ (PhCO ₂) ₄]	

	·5MeOH (19).	91
6.1.20	Preparation of $[\text{Ho}_4\text{Fe}_6(\mu_3\text{-OH})_4(\text{mdea})_6(\text{mdeaH})_2(\text{N}_3)_8(\text{PhCO}_2)_4(\text{OH}_2)_2] \cdot 4\text{MeCN}$ (20)	91
6.1.21	Preparation of $[\text{Er}_4\text{Fe}_6(\mu_3\text{-OH})_4(\text{mdea})_6(\text{mdeaH})_2(\text{N}_3)_8(\text{PhCO}_2)_4(\text{OH}_2)_2] \cdot 4\text{MeCN}$ (21)	92
6.1.22	Preparation of $[\text{Tm}_4\text{Fe}_6(\mu_3\text{-OH})_4(\text{mdea})_6(\text{mdeaH})_2(\text{N}_3)_8(\text{PhCO}_2)_4(\text{OH}_2)_2] \cdot 4\text{MeCN}$ (22)	92
6.1.23	Preparation of $[\text{ErFe}_4(\mu_4\text{-O})(\text{mdea})_3(\text{mdeaH})(\text{O}_2\text{CPh})_2(\text{N}_3)_4] \cdot 2.5\text{MeCN}$ (23)	92
Chapter 7	Methods of characterisation	94
7.1	FT-IR spectroscopy	94
7.2	Elemental analysis	94
7.3	X-ray powder diffraction	94
7.4	X-ray crystallography	94
7.5	Magnetic measurements	95
Chapter 8	Crystallographic data	96
Chapter 9	Bibliography	100
Appendix A	List of inorganic compounds	108
Appendix B	List of organic compounds	108
Appendix C	List of abbreviations	109
Appendix D	List of figures	110
Appendix E	List of tables	115
Appendix F	List of schemes	116

Chapter 1: Introduction

1.1 From magnet to Single Molecule Magnet (SMM)

Historically, magnetism has been recognised for thousands of years. An account, that is probably apocryphal, tells of a shepherd called Magnes in Crete who around 900 B.C discovered the naturally occurring magnet lodestone (a form of magnetite, Fe_3O_4) in a region later named Magnesia. Supposedly, while he was walking over a deposit, the lodestone pulled the nails out of his sandals and the metal tip from his staff. This phenomenon was firstly discovered by the Greeks and later used by the Chinese to create the floating compass.^[1] Later, the understanding of the magnetic phenomenon was significantly influenced by many people over many years.^[2] In 1269 Petrus Peregrinus de Maricourt identified that magnets have poles called North and South magnetic poles. He noted that opposite poles attracted while similar magnetic poles repelled and that also breaking a magnet was not destructive. Years later, in the 16th century, William Gilbert created a new synthetic magnetic-iron that lost its magnetic force on heating and regained upon cooling.

In the 19th century, additional key developments occurred and the understanding of the phenomenon of magnetism was greatly influenced by pivotal contributions. Hans Christian Ørsted observed that electricity affected magnets (1819); Michael Faraday invented the electromagnet (1823), and the use of magnets enabled the production of low-cost electricity. Heinrich Rudolf Hertz (1885) clarified and expanded the electromagnetic theory of light that had been put forward by Maxwell. In 1907 French physicist, P. Weiss, developed the theory of ferromagnetism based on the assumption that the interaction between magnetic molecules could be described empirically considering an internal molecular field. Niels Bohr identified the underlying physics from which magnetism results, *i.e.* the minute spin associated with an unpaired electron (1913).^[3] Conventional magnetic materials are prepared at high temperatures using metallurgical methodologies. These materials are atom-based magnets which means that their active spins are located in the atomic orbitals of the constituent metal ions.^[4] These classical magnets are two- or three-dimensional arrays of inorganic atoms, transition metals and/or lanthanide metals, providing spin units.^[4,5] Later on further development to design molecule-based magnets with bulk magnetism led to a new field called Molecular Magnetism.^[6] These magnetic materials can no longer be synthesised in the metallurgical manner because molecular

magnets comprise purely organic and organic/inorganic hybrid materials for which high temperature conditions usually inhibit their formation.^[6] These magnets are thus prepared using conventional organic and inorganic synthetic methodologies.

Molecular magnetism has been fueled by the discovery of Single Molecule Magnet (SMM) behaviour first reported in 1991.^[7] It was discovered that the $[\text{Mn}_{12}\text{O}_{12}(\text{O}_2\text{CMe})_{16}(\text{H}_2\text{O})_4]$ complex (Mn12Ac) first synthesised in 1980^[8] exhibits slow relaxation of magnetisation at low temperatures and thus represents a molecular approach to nanomagnets. Their special characteristics arise from purely molecular properties. These molecules possess a spin ground state (S), where $S = 0$ or $\geq \frac{1}{2}$ and a uniaxial magnetoanisotropy, where $D < 0$. The combination of these properties can lead to an energy barrier to the thermal relaxation of magnetisation.

The magnetic bistability arising from this energy barrier indicates potential applications for these materials in information storage devices, whereby a single molecule could act as the smallest possible unit of magnetic memory. They have many important advantages over conventional nanoscale magnetic particles composed of metal, metal alloys and metal oxides because of their uniform size, solubility in organic solvents and readily alterable peripheral ligands. In order to obtain new SMMs, polynuclear metal compounds which contain interacting metal centres held together by bridging units, such as oxygen atoms derived from oxides, hydroxide, alkoxide and carboxylates, have been synthesised. Extended networks of magnetically coupled SMMs can lead to new magnetic behaviour induced by the intrinsic properties of the magnetic units, such as the high-spin state, the Ising-type anisotropy and quantum effects.

1.2 Introduction to magnetic susceptibility

In electromagnetism the magnetic susceptibility (Latin: *susceptibilis* “receptiveness”) is the degree of magnetisation of a material in response to an applied magnetic field. Magnetic measurements can give information about the electronic structure and magnetic exchange interactions and stereochemistry of transition metal complexes. This section provides a brief overview of how magnetic measurements can be applied to this area of inorganic chemistry. More detailed accounts are given in standard texts by Carlin,^[9] Mabbs and Machin,^[10] O’Connor,^[11] Kahn^[12] and Kittel.^[13]

1.2.1 Basic theoretical approach of magnetism

Movement of an electrical charge (which is the basis of electric currents) generates a magnetic field in a material. Magnetism is therefore a characteristic property of all materials that contain electrically charged particles and for most purposes can be considered to be entirely of electronic origin. In an atom, the magnetic field is due to the coupled spin and orbital magnetic moments associated with the motion of electrons. There are three principal origins for the magnetic moment of a free atom. First, the spin magnetic moment this is due to the precession of the electrons about their own axis. Second, the orbital magnetic moment which is due to the motion of electrons around the nucleus and, finally, the change in the orbital moment induced by an applied magnetic field. The first two effects give rise to paramagnetic contributions and the latter gives a diamagnetic contribution. The magnetisation, M , is defined as the magnetic moment per unit volume. The magnetic susceptibility, χ , is the degree to which a material can be magnetised in an external magnetic field. The magnetic susceptibility per unit volume is then:

$$\chi = M/H \text{ (cgs)} \quad \text{or} \quad \chi = \mu_0 M/H \text{ (SI)} \quad \text{Eq. 1.1}$$

where H is the macroscopic magnetic field in Ørsted, Gauss or Tesla. It is convenient to refer to M/H as the susceptibility without specifying the system units. Susceptibility can be referred with respect to volume, unit mass or to a mole of the substance, hence the molar susceptibility is written as χ_M and the magnetic moment per gram is sometime written as σ .^[11]

Generally χ is the algebraic sum of two contributions:

$$\chi = \chi^D + \chi^P \quad \text{Eq. 1.2}$$

where χ^D and χ^P represent the diamagnetic and paramagnetic susceptibilities, respectively. χ^D is negative and χ^P is positive. When χ^D dominates, the sample is called diamagnetic with the magnetisation opposite to the applied magnetic field. Similarly, when χ^P dominates, the sample is called paramagnetic with the magnetisation in the direction of the applied magnetic field.^[12]

1.3 Types of magnetic behaviour

The origin of magnetism lies in the orbital and spin motion of electrons and the interaction of these electrons with one another. The best way to introduce the different kinds of magnetism is to describe the response of the susceptibility in an applied magnetic field. The main distinction is that in some materials there are no collective interactions of atomic magnetic moments, whereas

in others there is very strong magnetic interaction between atomic moments. Therefore the magnetic behaviour of a molecular magnetic material can be described on the atomic or ionic level, in terms of diamagnetism and paramagnetism.^[9,12]

1.3.1 Diamagnetism

Diamagnetism is a fundamental property of matter which is always present, even when it is masked by the paramagnetism. It is due to the interaction of the magnetic field with the motion of electrons in their orbitals. Diamagnetic susceptibility χ^D is usually independent of the temperature and the strength of the applied field. When this is the only response, these substances are composed of atoms which have no net magnetic moments because all the orbitals are filled. When a magnetic field is applied, a negative magnetisation is produced and the susceptibility is negative.

1.3.2 Paramagnetism

Any atom, ion or molecule that has one or more unpaired electrons is paramagnetic and possesses a net magnetic moment. These substances are attracted into a magnetic field due to partial alignment of the atomic magnetic moments in the direction of the field resulting in positive magnetisation and positive magnetic susceptibility. Paramagnets do not retain any magnetisation in the absence of an externally applied magnetic field because thermal motion causes the spins to become randomly oriented. Thus the total magnetisation will drop to zero when the applied field is removed.

1.3.3 Ferromagnetism

Substances which have magnetic interactions between the neighbouring paramagnetic centres leading to an increase in the magnetic moment are designated as ferromagnets. In a ferromagnet, the individual moments are perfectly aligned parallel to each other below a critical temperature, called the Curie temperature. A ferromagnetic substance usually divides into domains to minimise its total free energy. A spontaneous magnetisation arises in each domain even in the absence of a magnetic field. Saturation of the magnetisation corresponds to the complete alignments of all magnetic domains.

1.3.4 Antiferromagnetism

Antiferromagnetism is also a consequence of cooperative interactions leading to long-range order like ferromagnetism. When the magnetic interaction between paramagnetic centres lead to an antiparallel alignment of the moments, the substance is referred to as an antiferromagnet. There is complete cancellation of the magnetic moments and it does not have any spontaneous magnetisation.

1.3.5 Ferrimagnetism

The behaviour of ferrimagnets qualitatively resembles that of ferromagnets because these materials also exhibit spontaneous magnetisation. The magnetic moments in ferrimagnets, however, tend to align antiparallel to each other, as in case of antiferromagnets, but there is incomplete cancellation of the spins. Ferrimagnets differ from ferro- and antiferromagnets in that they involve two or more magnetic species possessing different magnitudes of magnetic moment. These species may be just two different valence states of the same ion or they may be different elements or even a combination of an ion and a free radical. The spontaneous magnetisation is the consequence of a lack of cancellation of the magnetic moments.

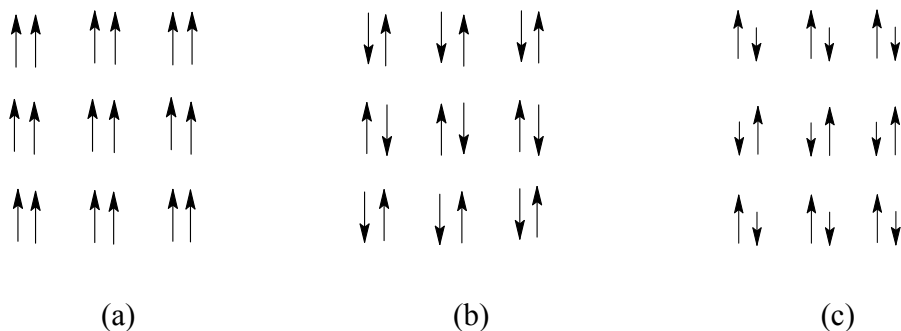


Fig. 1.1 The alignment of magnetic moments (a) ferromagnets, (b) antiferromagnets and (c) for ferrimagnets.

1.4 Determination of magnetic behaviour

It was shown by Pierre Curie that for most paramagnetic substances with isolated sites the magnetisation follows a Curie law to a good approximation:

$$M = C \cdot H / T \quad \text{Eq. 1.3}$$

where M is the resulting magnetisation, H is the applied field, T is absolute temperature and C is Curie constant. Since the magnetic susceptibility is defined as $\chi = M/H$, in this case:

$$\chi = C/T \quad \text{Eq. 1.4}$$

This equation is known as the Curie Law. This law indicates that the susceptibility, χ , of paramagnetic materials is inversely proportional to their temperature. Curie's law is only valid under conditions of low magnetisation, since it does not consider the saturation of magnetisation that occurs when the atomic dipoles are all aligned in parallel. After everything is aligned, increasing the external field will not increase the total magnetisation since there can be no further alignment. However such saturation typically requires very strong magnetic fields. Furthermore, the law is not valid at very low temperature because the magnetic moments may order. Therefore, the susceptibility should be measured with sufficiently low applied fields and the $1/\chi$ versus T plots fitted for the higher temperature region with the straight line extrapolated to the low temperature region to confirm whether the substance is an isolated paramagnet (intercept at 0 K) or coupled and thus with a non-zero intercept and obeying a Curie-Weiss law as explained next.

1.4.1 Curie-Weiss paramagnetism

In some cases where the paramagnetic atoms or ions interact, Curie's law is no longer valid and the magnetic exchange between spin carriers needs to be included in the model. As a result, in ferromagnets and antiferromagnets the Curie-Weiss law is applicable, which is:

$$M = C \frac{H}{T - \theta} \quad \text{with} \quad C = \frac{Ng^2\mu_B^2}{4k_B} \quad \theta = \frac{zJ}{2k_B} \quad \text{Eq. 1.5}$$

where θ is the Weiss constant, and the magnetic susceptibility is:

$$\chi = C/(T - \theta) \quad \text{Eq. 1.6}$$

There are three ways to plot the temperature dependence of the magnetic susceptibility which are shown in Fig. 1.2 and 1.3. These plots give information about the kind of magnetic interactions present in a compound.

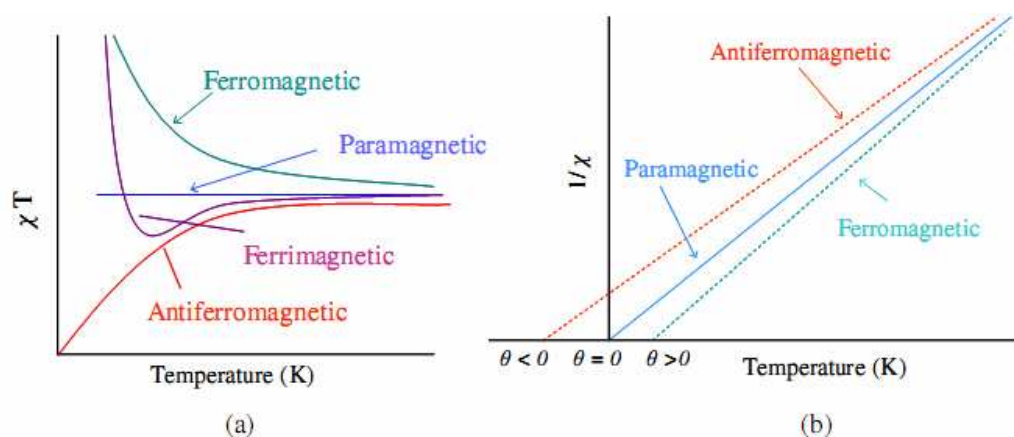


Fig. 1.2 (a) The plot of χT and (b) the plot of $1/\chi$ as a function of temperature for paramagnetic, ferromagnetic, antiferromagnetic and ferrimagnetic materials.

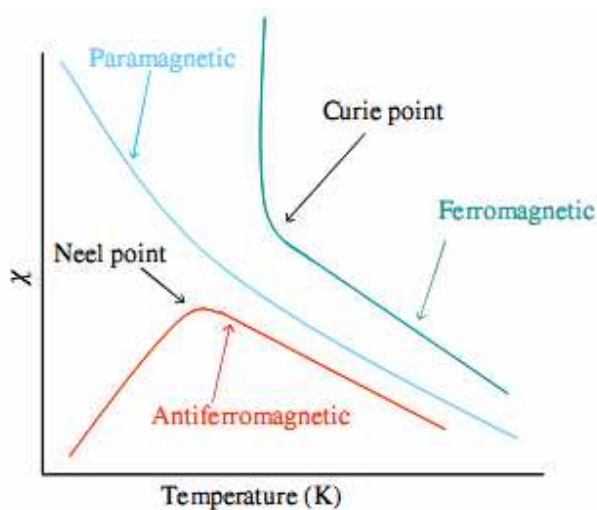


Fig. 1.3 The plot of magnetic susceptibility as a function of temperature for paramagnetic, ferromagnetic, antiferromagnetic materials.

Magnetic interactions are typically characterised by their responses to variations in temperature and applied magnetic field. Each of these classes of magnetism, described above, has a characteristic response to temperature and applied magnetic field which is used to determine the type and strength of the magnetic interaction in a molecular material. The most informative plot is the thermal variation of the product of the temperature and magnetic susceptibility. The value of the Weiss constant, θ , can be obtained directly by plotting $1/\chi$ versus T plot where θ is the negative intercept on the temperature axis for antiferromagnetic and ferrimagnetic materials and the positive intercept on the temperature axis for ferromagnetic materials (Fig. 1.2). For a true paramagnetic material, the Weiss constant is zero and the χT product as a function of temperature

is a horizontal line. On the other hand, variations of the χT values in the low temperature range exist for antiferromagnets, ferromagnets and ferrimagnets. At high temperatures, the χT product varies little or remains unvaried due to the effective paramagnetic behaviour of magnetic materials. When the Weiss constant is positive, which indicates the presence of ferromagnetic interactions, the χT product displays an upward deviation from the curve on lowering the temperature. When the Weiss constant is negative, a decrease in the χT product is observed. This indicates the presence of antiferromagnetic interactions; therefore a downward curvature is displayed. For ferrimagnetic materials, the χT versus T curve presents a slight downward curvature and then an increase in the low temperature range.

In ferromagnets, even though electronic exchange forces are very large, thermal energy eventually overcomes the exchange and produces a randomising effect. This occurs at a particular temperature called the Curie temperature (T_C) shown in the χ versus T plot (Fig. 1.3). Above T_C an ideal ferromagnet becomes a paramagnet that obeys the Curie-Weiss law,^[14] but below this temperature magnetic susceptibility increases rapidly. An exchange integral, J , is used to define the degree of coupling at any temperature and is given in units of cm^{-1} or K. For ferromagnetic coupling J is positive. In an antiferromagnet, above a critical temperature, known as the Néel temperature, T_N , thermal agitation destroys magnetic ordering and a material become a paramagnet, but below this temperature, its magnetic susceptibility decreases with decreasing temperature. A negative J value indicates antiferromagnetic coupling. Ferrimagnets, like ferromagnets, hold spontaneous magnetisation below the Curie temperature and show no magnetic order (paramagnetic) above this temperature.

1.5 Single Molecule Magnets (SMMs)

A single molecule magnet (SMM) is a molecule that shows slow relaxation of the magnetisation of purely molecular origin. It is a molecule that can be magnetised in a magnetic field and that will remain magnetised even after switching off the magnetic field. This is a property of the molecule itself. No interaction between the molecules is necessary for this phenomenon to occur. This makes SMMs fundamentally different from traditional bulk magnets. SMMs can be dissolved in a solvent or put in some other matrix, like a polymer, and will still show this property. The prerequisites for such a system are (a) a high-spin ground state (S), (b) a high zero-field splitting (due to high magnetic anisotropy) and (c) negligible magnetic interaction between molecules.

The combination of these properties can lead to an energy barrier so that at low temperatures the system can be trapped at the bottom of one of two high-spin energy wells (Fig. 1.5). The spin anisotropy manifests itself as an energy barrier that spins must overcome when they switch from an “all up” alignment to an “all down” alignment. This barrier (U) is defined as:

$$U = S^2 |D|$$

where S is the dimensionless total spin state and D is the zero-field splitting parameter in cm^{-1} or K. The selection rule $\Delta M_S = \pm 1$ for an allowed spin transition, results in energy barrier U which separates the two lowest energy levels of $M_S = \pm S$. A positive D value would result in the $M_S = 0$ level being lowest in energy, such that there is no energy cost for losing direction of the spin *i.e.* in going from $M_S = +S$ to $M_S = -S$). This means that for a molecule to behave as an SMM, it should have a negative D value. Theoretically the higher the barrier the longer a material remains magnetised, and a high barrier is obtained when the molecule contains many unpaired electrons and also when its zero-field splitting value is large. An example is the $(\text{Mn}_{12}\text{-Ac})^{[8]}$ cluster (Fig. 1.4) which is composed of a central $\text{Mn(IV)}_4\text{O}_4$ cube surrounded by a ring of 8 Mn(III) units connected through bridging oxo ligands. It has a spin state of 10 (involving 20 unpaired electrons) and $D = -0.05 \text{ cm}^{-1}$ resulting in a barrier of 50 cm^{-1} (Fig. 1.5).

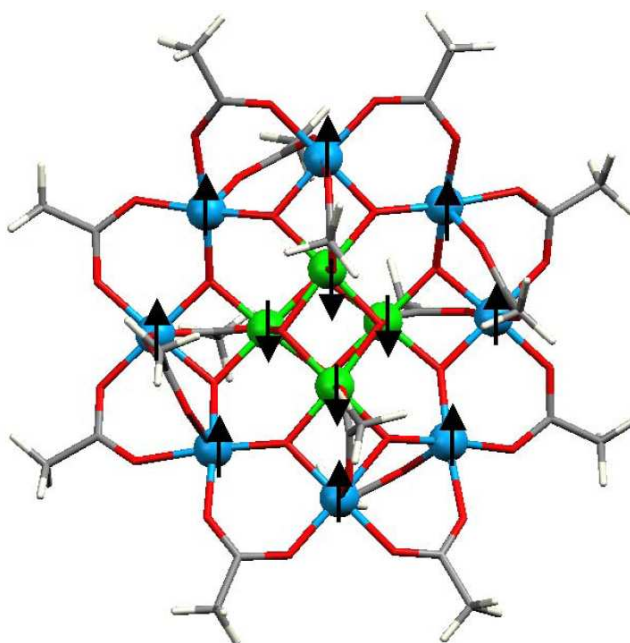


Fig. 1.4 Structure of $[\text{Mn}_{12}\text{O}_{12}(\text{CH}_3\text{COO})_{16}(\text{H}_2\text{O})_4] \cdot 2\text{CH}_3\text{COOH} \cdot 4\text{H}_2\text{O}^{[8]}$ Colour code: blue Mn^{3+} , green Mn^{4+} , red oxygen, grey carbon and white hydrogen.

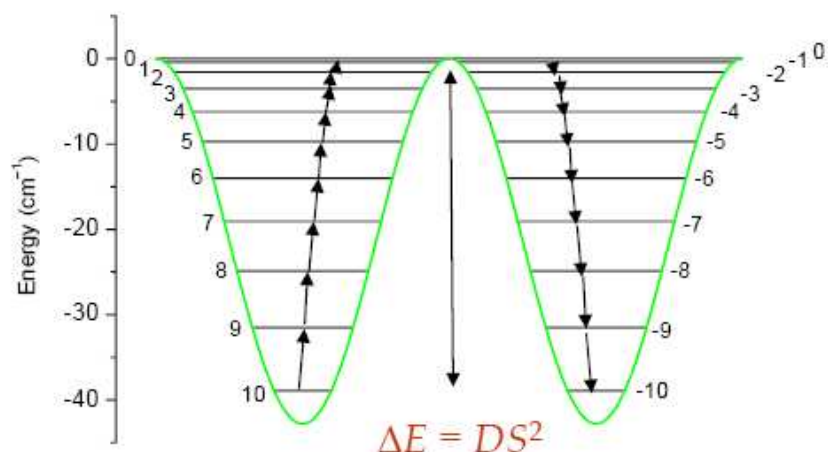


Fig. 1.5 Energy diagram showing the relative positions of the zero-field split M_S levels of an $S_T = 10$ system, and the barrier mediating between the $M_S = +10$ and the $M_S = -10$ states.

SMM behaviour is characterised by a hysteresis seen when magnetisation is measured in a magnetic field sweep: on lowering the magnetic field again after reaching the maximum magnetisation, the magnetisation remains at high levels and it requires a reversed field to bring magnetisation back to zero (Fig. 1.6). It has been reported that the energy barrier U is slightly dependent on Mn_{12} -Ac crystal size/morphology, as well as the magnetisation relaxation times, which varies as function of particle size and size distributions.^[15]

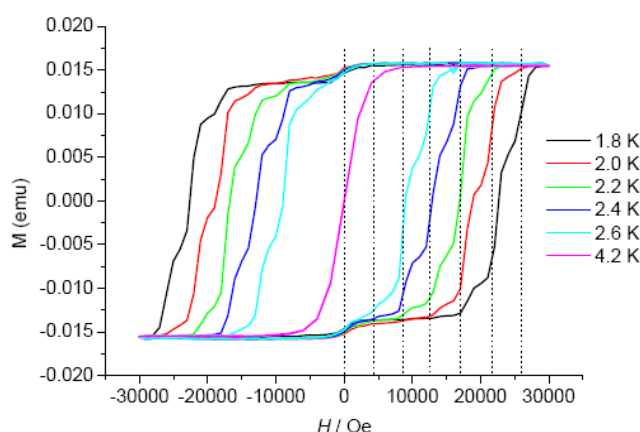


Fig. 1.6 The magnetic hysteresis loops of Mn_{12} -Ac are shown at the indicated temperatures.^[16]

The effect of single molecule magnetism is readily probed through ac magnetic susceptibility measurements, which provide a direct means of gauging the relaxation rate. Here the magnetic susceptibility of a sample is measured using a weak magnetic field that switches

direction at a fixed frequency. If the effective barrier to magnetisation relaxation is significant in comparison to the thermal energy, then the measured susceptibility referred to as the in-phase or real component (χ') of the ac susceptibility begins to diminish. Accordingly, the portion of the susceptibility that cannot keep up with the switching field, the out-of-phase or imaginary component of the ac susceptibility, χ'' , increases. When a magnetisation reversal barrier exists, then χ' and χ'' are also frequency-dependent. If the net magnetisation relaxes fast enough to keep up with the oscillating ac field, then there is no imaginary (out-of-phase) susceptibility (χ'') and the real (in-phase) susceptibility (χ') is equal to the dc susceptibility (Fig. 1.7).

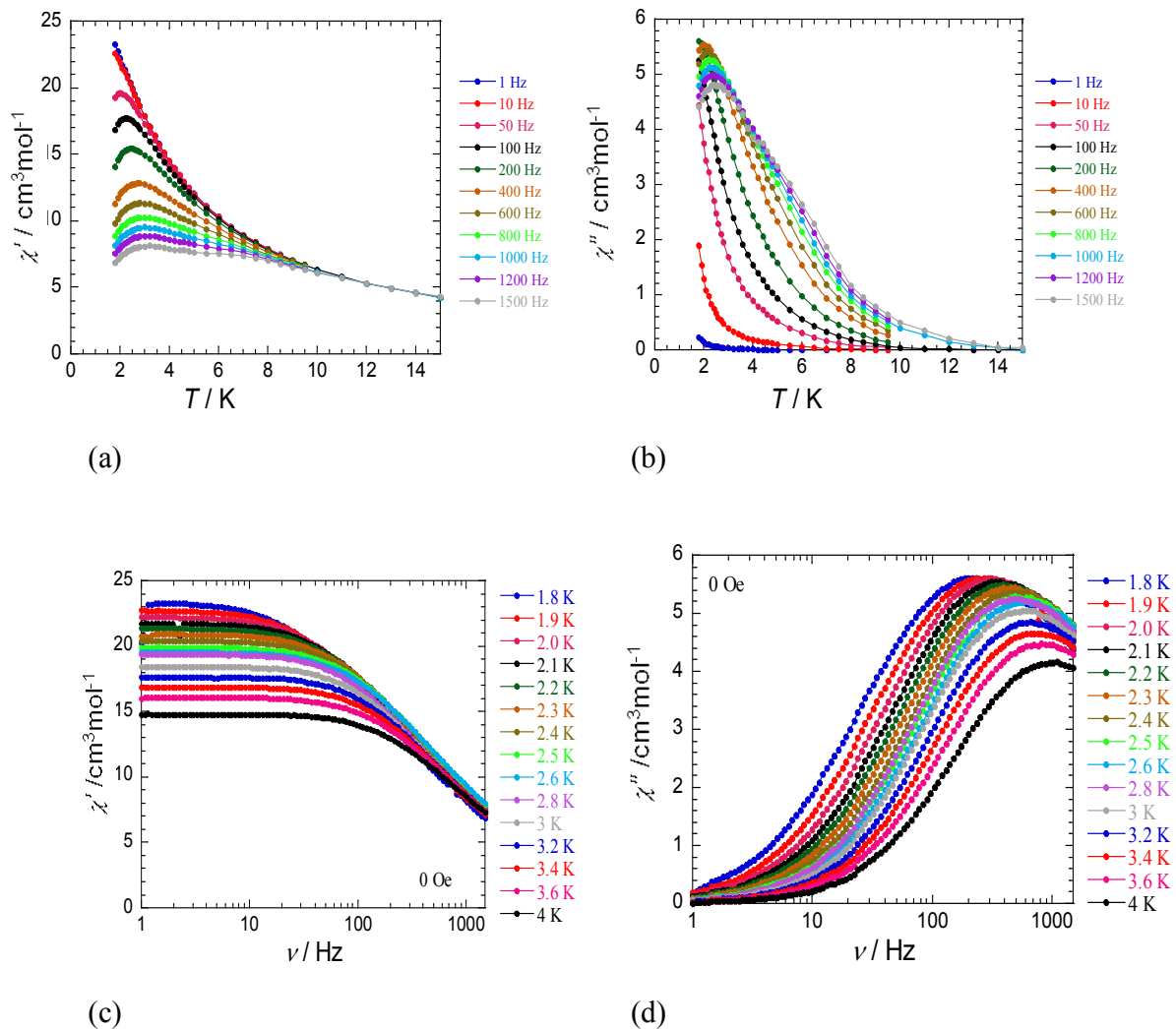


Fig.1.7 An example of ac susceptibility measurements as a function of temperature at different frequencies, and as a function of frequency at different temperatures: (a, c) in-phase and (b, d) out-of-phase signals.

If just a single relaxation process is operational, then a plot of χ'' versus temperature will display a peak with a maximum at the temperature where the switching of the magnetic field matches the relaxation rate, $1/\tau$. Furthermore, since $1/\tau$ increases with temperature, this peak should shift to higher temperature when the switching frequency is increased. The relaxation time for the magnetisation in a single molecule magnet can be expressed by the Arrhenius relationship:

$$\tau = \tau_0 \cdot e^{(U_{\text{eff}}/k_B T)}$$

where the pre-exponential term τ_0 can be thought of as the inverse of the relaxation attempt frequency. A plot of $\ln(\tau)$ versus $1/T$ should be linear, with the slope and intercept permitting evaluation of U_{eff} and τ_0 respectively (Fig. 1.8).

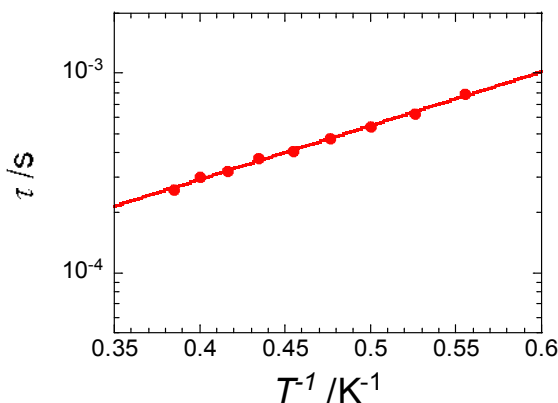


Fig. 1.8 An example of τ versus $1/T$ plot obtained from both temperature and frequency dependent ac susceptibility measurements under zero dc field.

It has also been recognised that there can be additional influences on the SMM behaviour such as quantum effects^[17] or inter-complex magnetic interactions.^[18] Indeed at low enough temperature, quantum tunnelling of the magnetisation can be experimentally observed as it becomes faster than the thermally activated relaxation involving U_{eff} . When two M_S microstates on either side of the energy barrier have similar energies, then there is an increased probability of quantum tunnelling of the magnetisation (QTM). SMM complexes appear to be unique systems for studying fundamental phenomenon such as quantum spin tunnelling and quantum interference. These may find uses in future application in molecular electronics.

1.6 Synthetic strategies for making polynuclear complexes

Several synthetic routes are being pursued to construct new magnetic materials that, ideally, satisfy the criteria for SMMs. In one route, rigid ligands such as cyanide are used as the bridging ligands; in the second, serendipitous or self assembly has been used for the construction of molecular magnetic materials.

Complexes that contain cyanide bridges have been constructed by blocking suitable coordination sites on metal fragments. An early synthetic success using this approach was the formation of a heptanuclear complex made by Verdaguer and Mallah.^[19] Significant progress has been attained in the construction of metallocyanides using different blocking ligands which generated a range of topologies, nuclearities and spin states. Hashimoto^[20] and Decurtins^[21] reported Mn_9M_6 cages ($M = W$ or Mo) which display fascinating magnetic properties with high-spin ground states for the molecules. Construction of interesting cages has been pursued with some of the metal units having a restricted number of coordination sites and others are completely free.^[22]

The second strategy can be termed as self-assembly. A prerequisite for the successful application of self-assembly is to accept the impossibility of understanding the influence of all factors involved in a reaction on the resulting product. Therefore a wide range of conditions for any specific reaction is explored. The substitution pattern of the ligand or ligands, the metal salt, the metal:ligand ratio, the crystallisation solvent, the solution concentration and the crystallisation temperature may all play a role in the formation of a complex. Although this synthetic approach produces unpredictable results, minor variations in the ligands may influence the structure and solubility. The use of mixtures of organic ligands can form complexes of higher nuclearities.^[23]

Another approach is to use co-ligands having carboxylate or hydroxyl groups to construct large polynuclear clusters. The functional groups can coordinate to more than one metal centre. In order to have N-donor atom and O-donor atoms, several coligands such as pivalic acid, carboxylic acid and azide were used along with the *N*-methyldiethanolamine ($mdeaH_2$) ligand. Varying the co-ligand by increasing the number of donor groups might lead to the incorporation of more metal centres. When alcohol-based solvents (ROH or H_2O) were employed, solvolysis reactions can occur, forming hydroxyl, alkoxy or oxo bridges.

Heterometallic complexes can be obtained by using two types of metal ions along with co-ligands. The presence of two different metal centres can give rise to interesting magnetic

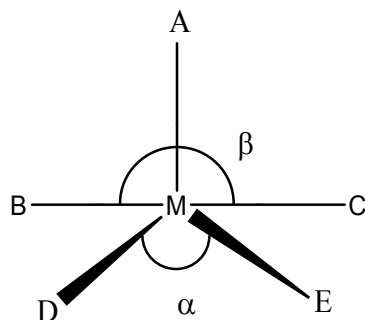
properties and can allow further investigations of the exchange interaction between two different metal ions. This can involve using two different transition metals or a combination of transition and lanthanide metal ions. The lanthanides behave as hard acids preferring O- rather than N-donors, while transition metal ions are borderline acids, having the tendency to coordinate to N-donors as well as O-donors. Consequently, a typical approach to construct *3d-4f* complexes is by self assembly of different metal ions with ligands containing both O- and N-donors.

1.7 Introduction to iron chemistry

Iron is a vital constituent of plant and animal life, and is the key component of haemoglobin. It is widely distributed in the Earth's crystal rocks as oxide and oxyhydroxide minerals such as *haematite*, *limonite*, *magnetite*, *goethite*, *lepidocrocite*, *akaganite*, *carbonate siderite* and also in sulfur-containing minerals such as iron pyrites. It has great significance in geological, environmental, industrial and biological fields. A major feature of Fe(III) chemistry is its hydrolysis leading to iron hydroxides such as rust or Fe(OH)₃. The most common oxidation states of iron are 2+ and 3+, and it forms a variety of coordination complexes. Most of these have distorted octahedral geometry.^[24] The studies on high-nuclearity iron clusters were motivated by the desire to understand biomineralisation processes, such as those in iron-storage protein ferritin,^[25] and the use of the synthetic analogue approach for the study of iron-containing enzymes.^[26a]

Iron-containing coordination clusters are the second largest family of SMMs after manganese aggregates. In contrast to Mn₁₂-Ac (which is a mixed-valance SMM), a diamagnetic ground state is common for iron complexes, especially with an even number of metals. Homovalent cages containing the predominant oxidation state Fe(III) lead to the expected dominant antiferromagnetic interactions. A few polynuclear complexes of iron in the oxidation state 2+ have also been shown to exhibit slow relaxation of the magnetisation. Five coordinate complexes tend to lie between trigonal bipyramidal (D_{3h}) and square based pyramidal (C_{4v}) geometries in the latter of which, the axial bond is normally longer. In five coordinate systems, such as that represented below (scheme 1), ideal square pyramidal geometry is associated with $\alpha = \beta = 180^\circ$, for A as the axial ligand β is the greater of the basal angles subtended by BMC in scheme 1. For perfectly trigonal bipyramidal geometry, α becomes 120° and BMC the principal axis. In the majority of real square pyramidal systems M is displaced out of the BCDE plane

towards A, so that these C_{4v} geometries usually have $\alpha = \beta < 180^\circ$ and can be characterised by the value of $(\beta - \alpha)$, which is 0° for C_{4v} , and 60° for a D_{3h} coordination polyhedron.^[26b,c]



Scheme 1. ML_5 five coordinate geometry complex.

1.7.1 An octanuclear Fe(III) cluster

The complex cation $[Fe_8O_2(OH)_{12}(tacn)_6]^{8+}$ was reported^[27] more than a decade before it was declared as the first properly identified SMM of iron.^[28,29] The structure shows a “butterfly” arrangement of a central tetrameric unit linked to four peripheral Fe(III) ($S = 5/2$) ions by two μ_3 - O^{2-} hydroxo bridges. The analysis of the temperature dependence of the magnetic susceptibility provided evidence for a ground $S = 10$ state, which can occur if six spins point up and two down. It shows slow magnetic relaxation in the Mössbauer spectra at *ca.* 30 K and magnetic hysteresis below 1 K.^[28] Steps in the hysteresis curve are observed due to $\Delta S = \pm 1$ transitions as the applied magnetic field is changed and it also has $D = -0.19\text{cm}^{-1}$.

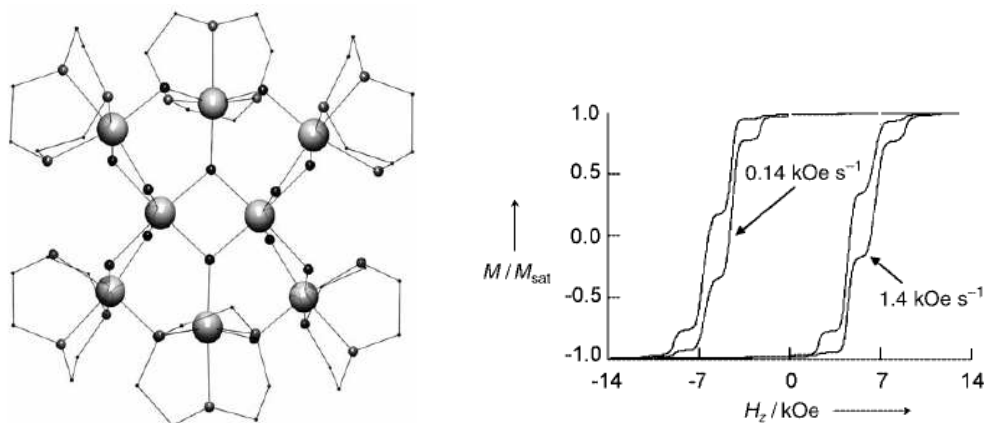


Fig. 1.9 $[Fe_8O_2(OH)_{12}(tacn)_6]^{8+}$ (left). Hydrogen atoms are omitted for clarity and tacn = 1,4,7-triazacyclononane. Magnetic studies (right).

1.7.2 [Fe₁₉(metheidi)₁₀(OH)₄O₆(H₂O)₁₂](NO₃), the largest nuclearity and spin Fe SMM

[Fe₁₉(metheidi)₁₀(OH)₄O₆(H₂O)₁₂](NO₃) belongs to a family of [Fe₁₉^{III}] clusters whose first example was reported in 1992.^[30] The first Fe₁₉ was found within a pair of co-crystallised Fe₁₇ and Fe₁₉ species. Later it was possible to isolate the Fe₁₉ cluster by using H₃metheidi instead of H₃heidi which simplified the interpretation of the magnetic behaviour.^[31]

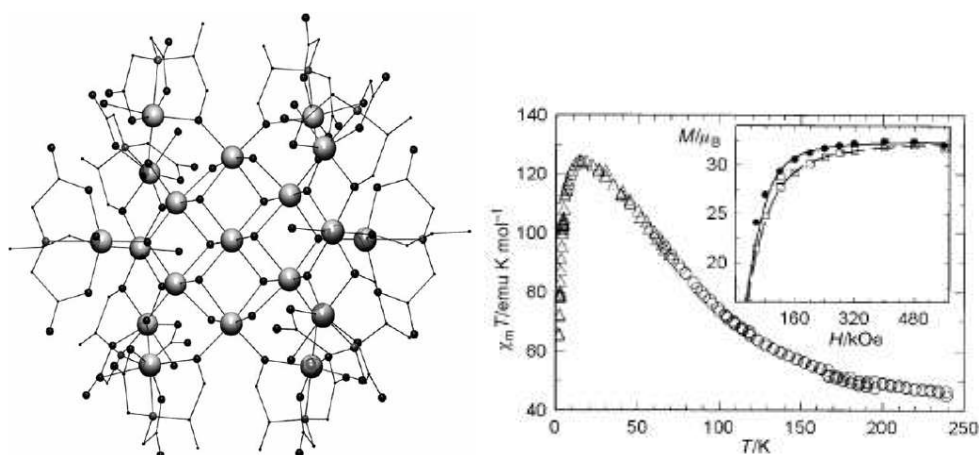


Fig. 1.10 [Fe₁₉(metheidi)₁₀(OH)₄O₆(H₂O)₁₂](NO₃) (left). Hydrogen atoms are omitted for clarity and metheidi = *N*-(1-Hydroxymethylethyl)iminodiacetic acid. Magnetic studies (right): Temperature dependence of the product of the magnetic susceptibility with temperature reported per mole of Fe₁₉ cluster, measured at 10 kOe down to 60 K (circles) and 500 Oe below 60 K (triangles). The inset shows the magnetisation measured at 2.45 (●) and 4.4 K (□). The lines have been calculated using $S = 33/2$, $D = -0.04 \text{ cm}^{-1}$ and $g = 1.96$.

1.7.3 [Fe₄(OMe)₆(dpm)₆], the smallest nuclearity Fe SMM

The tetranuclear Fe(III) cluster [Fe₄(OMe)₆(dpm)₆] is the Fe SMM with the smallest nuclearity.^[32] The cluster comprises a centred triangle of four Fe(III) ions bridged by six μ_2 -OMe⁻ ligands with the peripheral Fe ions each chelated by two dpm⁻ ligands. An antiferromagnetic interaction mediated by methoxide bridges is observed leading to ground state $S = 5$ and $D = -0.2 \text{ cm}^{-1}$.

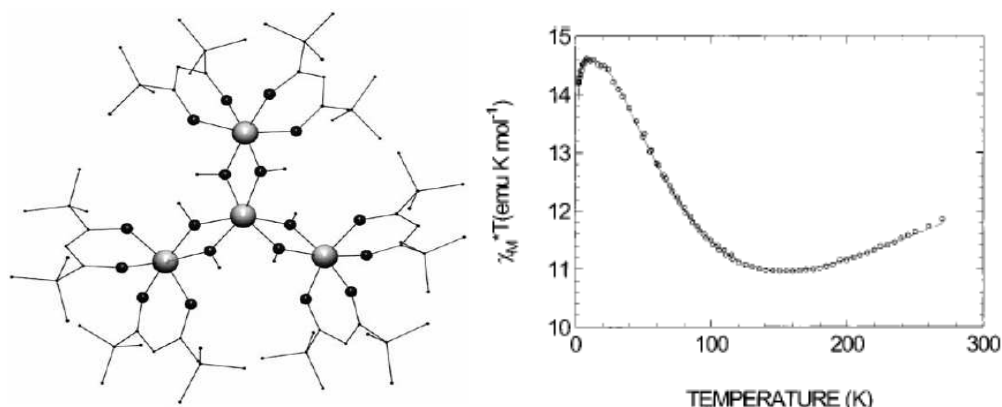


Fig. 1.11 $[\text{Fe}_4(\text{OMe})_6(\text{dpm})_6]$ (left). Hydrogen atoms are omitted for clarity and dpm = dipivaloylmethane. Magnetic studies (right).

1.8 Introduction to rare-earth metal chemistry

The lanthanides are unusual in that they are all found together in natural ores. The most common ores are *Bastnasite* and *Monazite*. In both ores, two general observations can be made about relative abundance. The abundance of the even atomic-numbered elements is greater than the odd atomic-numbered elements and abundance diminishes with increasing atomic number, odd or even. The rare-earth metals are all electropositive with a remarkable uniformity of chemical properties. Frequently the only significant difference between two lanthanides is their size; the ability to choose a rare-earth metal of a particular size often leads to the possibility to “tune” the properties of their compounds. The elements favour the oxidation state Ln(III) with a uniformity that is unprecedented in the periodic table. Other properties vary significantly *e.g.* the radii of the Ln^{3+} ions contract steadily from 116 pm for La^{3+} to 98 pm for Lu^{3+} . The decrease in ionic radius is attributed in part to the increase in Z_{eff} as electrons are added to the 4*f* subshell, but detailed calculations indicate that subtle relativistic effects also make a substantial contribution. A Ln^{3+} ion is a hard Lewis acid, as indicated by its preference for F^- and oxygen-containing ligands and its occurrence with PO_4^{3-} in minerals.

The relatively large Ln^{3+} ions can have high coordination numbers and a variety of coordination environments in the solid state which are also observed in solution. The spatially buried *f* electrons have no significant stereochemical influence and consequently ligands adopt positions that minimise the ligand-ligand repulsions. The study of the coordination chemistry of lanthanide elements is a rapidly growing area of interest because of the potential applications of their complexes as magnetic resonance imaging (MRI)^[33] contrast agents as catalysts in organic

synthesis,^[34] as molecular magnetic materials,^[35] as luminescent species^[36] and as single molecule magnets.^[37] In contrast to the advances in the synthesis and study of the magnetic properties of polynuclear complexes of the *d*-block metals,^[38,39,40] rather little attention has been devoted to exploring the systematic synthesis and study of the magnetic properties of Ln(III) clusters.^[41-50] In the lanthanide series, the inner 4*f* electron shell is filled from lanthanum to lutetium. Lanthanides (Ln) have the advantages that they can have a large number of unpaired *f*-electrons and considerable single-ion anisotropy.

The origin of SMM behaviour in lanthanide containing compounds is, however, more complicated than that of most *d*-block transition metal ions since there is likely to be a significant orbital component. The effect of spin-orbit coupling increases as the atomic number increases, with the exception of the 4*f*⁷ configuration, which has no first order angular momentum. As a result it is useful to synthesise Gd(III) analogues of Ln(III) complexes in order to interpret the magnetic properties. The limited magnetic investigations have focussed on Gd(III)-Gd(III) coupling because of the relative simplicity as compared to the rest of the Ln(III) ions where both orbital and crystal field effects have to be considered in the interpretation of results. In general, the complexity of lanthanide systems is based on the characteristics of the magnetic centres and the type of structural links between them. The magnetic interactions between paramagnetic centres can take place not only through single atoms but also through multi-atomic bridges such as those provided by carboxylato and other O–C–O ligands. The latter have been proved to be effective for the transmission of magnetic information through a variety of bridging conformations *e.g.* bidentate or tridentate bridging. Usually, when the lanthanide centres are functionalised with these kinds of ligands, the resulting structural motifs are complicated; however they present potentially interesting magnetic properties.^[51,52] According to the literature, weak ferromagnetic^[53-55] or weak antiferromagnetic^[34,45,49,56-58] interactions can be found in polynuclear Ln(III) clusters. High-nuclearity clusters of paramagnetic metal ions are of the interest in view of the fact that they can exhibit SMM phenomenon.^[8] However, little attention has been devoted to pure lanthanide systems.^[36,39,59] Two examples are provided below.

1.8.1 A mononuclear compound showing SMM or single ion magnetisation behaviour

Ishikawa reported single metal ion lanthanide complexes, functioning as magnets at the single molecule level.^[60] Ac magnetic susceptibility measurements have been reported for

bis(phthalocyaninato)terbium and bis(phthalocyaninato)dysprosium anions in the sub-kelvin temperature range indicating quantum tunnelling of magnetisation in these single-ion SMMs.^[59]

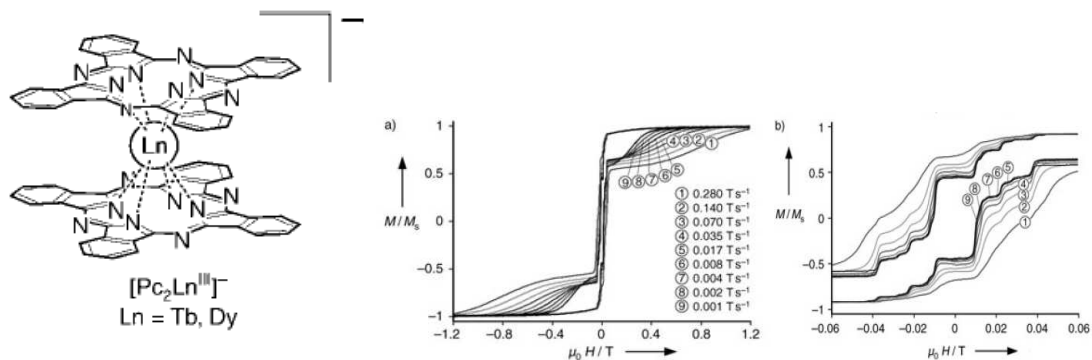


Fig.1.12 TBA[(Pc)₂Tb_{0.02}Y_{0.98}] (left). Hydrogen atoms are omitted for clarity and Pc = phthalocyanine. Magnetic studies (right).

1.8.2 The dysprosium triangles [Dy₃(μ₃-OH)₂L₃Cl(H₂O)₅]Cl₅·19H₂O

Dysprosium triangles exhibiting a vanishing susceptibility at low temperature were investigated. Such behaviour is unprecedented in systems which are comprised of an odd number of unpaired electrons. In spite of the almost non-magnetic ground state, features typical of SMM behaviour are observed for the thermally populated excited state, suggesting that a resonant under-barrier relaxation process is also active. This observation is strongly relevant to molecular nanomagnetism because the presence of a large spin ground state appears not to be a necessary condition to observe slow relaxation of the magnetisation.^[39]

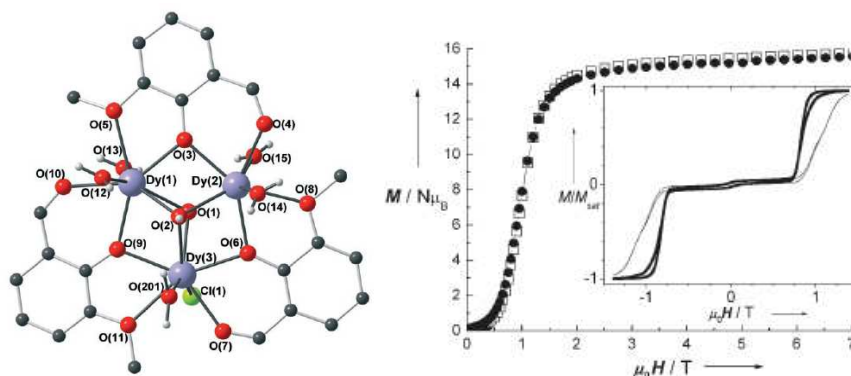


Fig.1.13 [Dy₃(μ₃-OH)₂L₃Cl(H₂O)₅]Cl₅·19H₂O (left). Hydrogen atoms are omitted for clarity. Magnetic studies (right).

1.9 Introduction to 3d-4f (Fe-Ln) complexes

Using a lanthanide element in permanent magnets is hardly a new concept. The first work in this area was published in 1935, when Urbaine, *et al.* reported that gadolinium is ferromagnetic.^[61] Some of the lanthanides have record magnetic moments, but unfortunately their Curie temperatures are at or far below room temperature. In the 1940's, scientists and engineers had access to reasonable quantities of high purity lanthanide elements and have systematically studied the many unique properties, not just magnetic, of these elements and their alloys.

The magnetic properties of the binary lanthanide-iron alloy compounds, including Nd-Fe, were examined at about the same time as the lanthanide-cobalt systems, in the 1960's and early 1970's. However, all the binary lanthanide-iron alloys have at least one of the following problems, making them unsuitable as permanent magnets:

- (1) A Curie temperature near or below room temperature,
- (2) Unfavourable anisotropy, usually an easy cone or an easy plane and
- (3) Antiferromagnetic coupling between the lanthanide and the iron magnetic moments, resulting in low saturation magnetisation.

Lanthanide ions have radii that vary between 116 and 98 pm; by comparison, Fe³⁺ has an ionic radius of 64 pm. Thus the volume occupied by a Ln³⁺ ion is typically 10 times greater than that occupied by a 3d-metal ion. Unlike the 3d-metal atoms, which rarely exceed a coordination number of 6, compounds of lanthanide ions often have high coordination numbers and a wide variety of coordination environments. Contrary to lanthanide-transition metal alloys, SMMs, which are molecular superparamagnets, derive their properties from the combination of a large ground state spin (*S*) value and a large and negative magnetoanisotropy (negative zero-field splitting parameter, *D*). In the case of mixed metal 3d-4f systems, the presence of lanthanide ions provides both large spin and considerable single-ion anisotropy. As reflected in the large *D* values, these systems could generate SMMs with properties significantly different from those of pure transition metal SMMs.^[62-66] This combination results in a significant energy barrier to magnetisation reversal, and hence slow relaxation of the magnetisation is observed at low temperatures. The latter can be detected as (i) frequency-dependent signals in ac susceptibility measurements, or as (ii) hysteresis in magnetisation versus applied dc field sweeps.^[13,76] There are now many homometallic SMMs, most of them Mn species,^[77] and new approaches aimed at producing heterometallic species have been more recently explored as a route to distinctly

different properties. As a result of such work, some mixed transition metal/lanthanide SMMs have recently been reported.^[63,64,69] However a goal of this research is also to construct Fe-Ln clusters which are valuable new additions to the growing family of mixed $3d-4f$ clusters. They possess a variety of structural motifs and various properties and the anisotropy of the lanthanides can be investigated by gauging their effect on Fe^{3+} using, for example, Mössbauer spectroscopy.

1.9.1 $[\text{Fe}_2\text{Ln}_2(\text{OH})_2(\text{teaH})_2(\text{O}_2\text{CPh})_6]$, A tetranuclear SMM

Examples of Fe-Ln clusters include the tetranuclear mixed $3d-4f$ complexes containing Fe and lanthanides reported by Murugesu *et al* which display interesting magnetic properties.^[70] Although the magnetic properties are complicated by the large spin-orbital coupling effects of most Ln(III) ions, hysteresis loops in the magnetisation behaviour have established them as an additional example of SMMs.

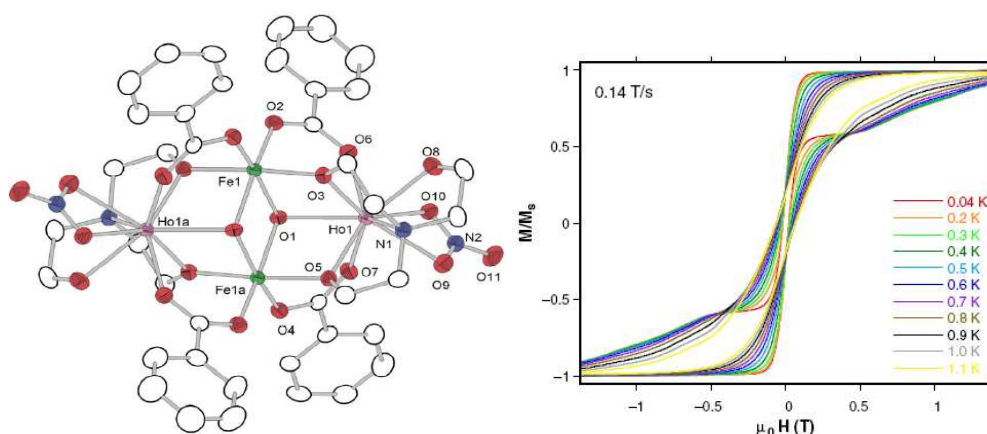


Fig. 1.14 $[\text{Fe}_2\text{Ho}_2(\text{OH})_2(\text{teaH})_2(\text{O}_2\text{CPh})_6]$ (left). Hydrogen atoms are omitted for clarity and tea = triethanolamine. Magnetic studies were carried out for Dy analogue (right).

1.9.2 A binuclear single molecule magnet (SMM)

Another example is a binuclear Fe(III)Dy(III) single molecule magnet reported by Yamashita's group in 2006.^[71] Low-temperature magnetisation measurements at fast sweeping pulsed field revealed hysteresis loops and step-like magnetisation, indicating quantum tunnelling effects. The Arrhenius fit yielded the relaxation barrier $\Delta = 8.98 \text{ cm}^{-1}$ and the pre-exponential term $\tau_0 = 7.77 \times 10^{-8} \text{ s}$.

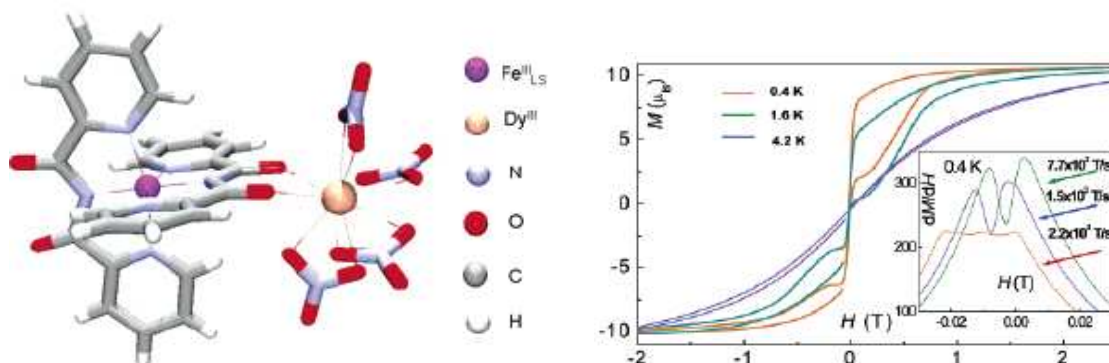
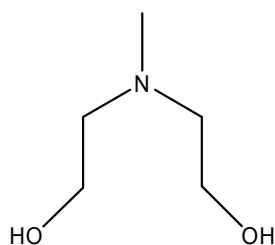


Fig. 1.15 Structure of $[\text{Fe}(\text{bpca})(\mu\text{-bpca})\text{Dy}(\text{NO}_3)_4]$ (left). Hydrogen atoms are omitted for Clarity and bpca = bis(2-pyridylcarbonylamine). Magnetic studies (right).

1.10 Ligand selection

N-methyldiethanolamine (mdeaH₂) has been reported in reaction systems with 3d transition metal elements, such as Mn,^[72-75] Fe^[75-79] and Ni,^[79,80] but the intersection of 3d transition metal elements and lanthanide is a field of chemical research requiring more attention. As a result, the mdeaH₂ ligand was selected to investigate 3d transition metal complexes, 3d-4f mixed metal clusters and 4f complexes. Coordination complexes containing the mdeaH₂ ligand along with different co-ligands (*e.g.* pivalic acid, benzoic acid) will be presented in the forthcoming chapters. In Fig 1.16, all the known coordination modes of this ligand are depicted and it is obvious that mdeaH₂ is a very useful means to build high-nuclearity clusters.



N-methyldiethanolamine (mdeaH₂)

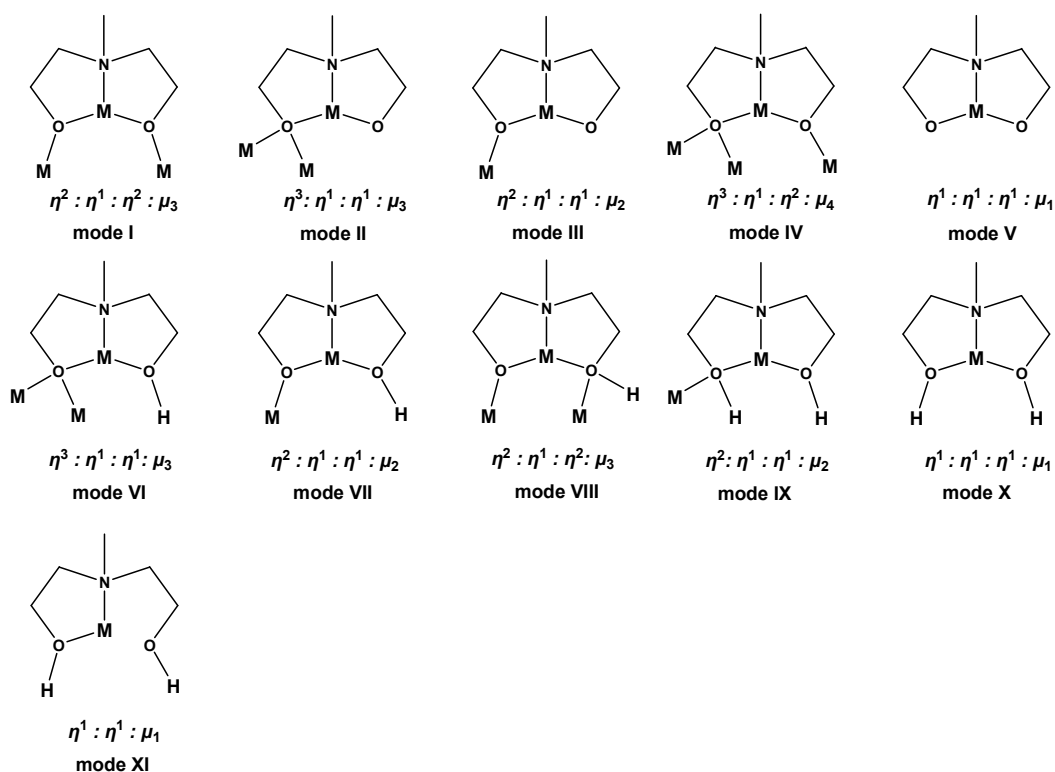


Fig. 1.16 Some reported coordination modes of ligand mdeaH₂ (mode I,^[73-77,79,81,82] mode II,^[80] mode III,^[78,83] mode IV,^[72] mode V,^[84] mode VI,^[73,79,85] mode VII,^[85] mode VIII,^[85] mode IX,^[85,86] mode X,^[83])

1.11 Co-ligand selection

After the discovery of the SMM phenomenon, various synthetic techniques were applied in order to synthesise compounds that would exhibit this behaviour. One of these techniques demands careful selection of a metal / ligand / co-ligand system, in which the co-ligand is a useful tool to construct high-nuclearity complexes. Carboxylate moieties are one of the most studied multibridging groups in inorganic chemistry. They can undergo self-assembly complexation reactions with metal ions to produce polynuclear metal compounds in which they can assume various coordination modes and can bridge many metal centres. Therefore pivalic acid and benzoic acid have been used as co-ligands to obtain novel *4f* and *3d-4f* metal aggregates. Polynuclear metal carboxylates are good candidates for the investigation of magnetic exchange coupling interactions between neighbouring metal ions. In Fig.1.17, common coordination modes for carboxylate groups are given.

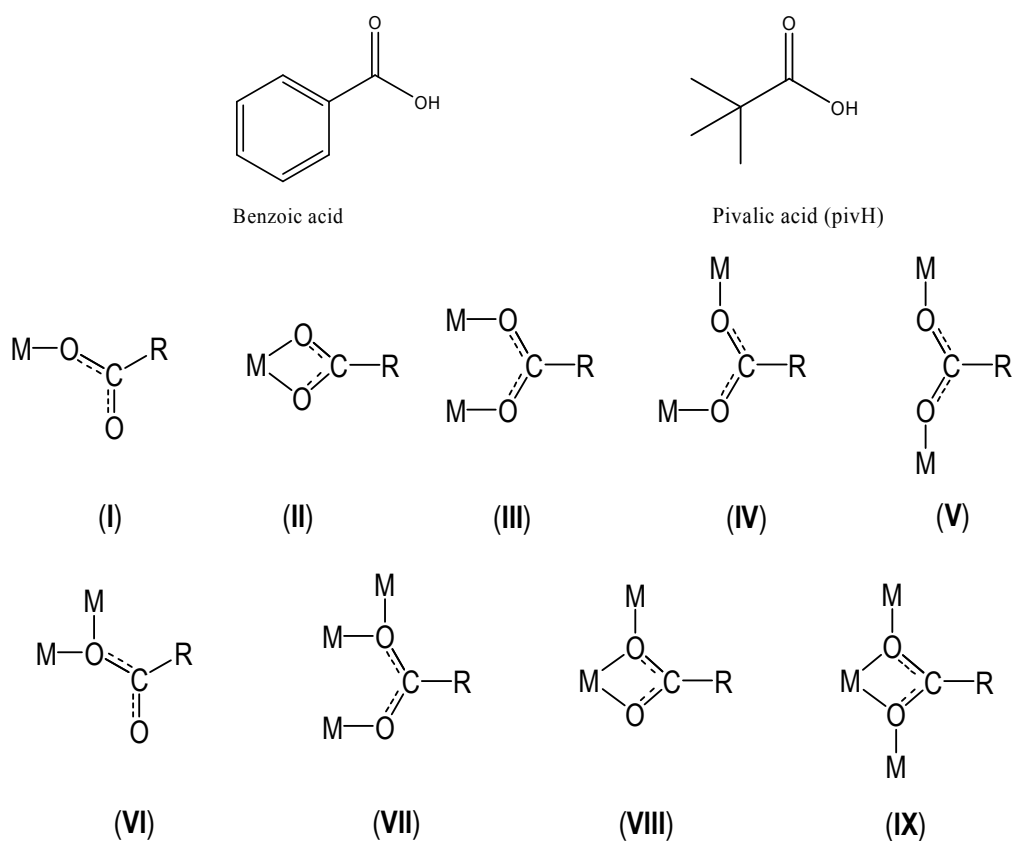


Fig. 1.17 Common coordination modes of the carboxylate group.

1.12 Thesis overview

This thesis describes the synthesis of homo- and heterometallic complexes which have been crystallographically characterised and magnetically investigated. The research results are divided into 2 chapters. Chapter 3 is concerned with the synthesis, characterisation of homometallic lanthanide complexes using the mdeaH₂ ligand along with different co-ligands (*e.g.* pivalic acid and benzoic acid). The fourth chapter presents the synthesis of heteronuclear Fe-Ln clusters by using mdeaH₂ and benzoic acid and their magnetic studies.

Chapter 2: Research Objectives

Small molecular aggregates of paramagnetic centres have revealed that they can possess non-zero ground state spins, hysteresis and tunnelling effects, which lead to them being single molecule magnets (SMM). The aim of this research work was to design and synthesise molecule-based materials and characterise their magnetic behaviour. In order to construct such polynuclear complexes, the concept of self-assembly of the paramagnetic metal ions with suitable ligands like *N*-methyldiethanolamine (mdeaH₂) was applied. This ligand (mdeaH₂) has been used in reaction systems with 3*d* transition metals such as Mn, Fe, and Ni. Based on the resulting structure and magnetic properties, further attempts were made to extend the system to explore interesting magnetic properties in Fe aggregates.

Secondly, despite the advanced synthetic methods and magnetic properties of polynuclear complexes of the *d*-block metals, less attention has been devoted to the synthesis of Ln(III) clusters. The construction of new 4*f*-metal clusters by the development of new reaction systems with *N*-methyldiethanolamine (mdeaH₂) is one area of research interest. The research focused on the formation of lanthanide clusters which exhibit fascinating magnetic properties leading to SMM behaviour.

Finally, in the combination of these two approaches the quest for new SMMs displaying high blocking temperatures has focused the interests of synthetic chemists towards development of 3*d*-4*f* heterometallic systems. For example, polynuclear clusters which combine high-spin and/or single-ion anisotropy have been reported with a barrier to reorientation of the spin, Δ_{eff} . From the synthetic point of view, the *N*-substituted diethanolamine and related ligands represent useful tools in the synthesis of polynuclear clusters possessing SMM behaviour. Sparked by the structural diversity and interesting properties of heterometallic 3*d*-4*f* compounds, the research was extended to investigate mixed 3*d*-4*f* (Fe-Ln) compounds as a means of enhancing anisotropy and/or spin state using *N*-methyldiethanolamine (mdeaH₂) as a ligand.

The synthesis of polynuclear metal clusters is achieved, in principle, by controlling the hydrolysis of metal ions either in an aqueous solution or in a mixture of organic solvents in the presence of the supporting ligands. A finite aggregate of oxygen-bridged metal ions is thus trapped within a shell of organic ligands, rather than proceeding to the formation of an extended oxide or hydroxide mineral structure. In order to explain in an appropriate way the magnetic interactions in these compounds, crystalline materials are the desirable products because they can

be well-characterized by X-ray crystallography. It is well known that the solvent, the concentration of the reactants, the temperature at which the reaction takes place, the ratio of the reactants and the pH of the final solution affect the final product. Bearing all these in mind, metal salts, ligands and co-ligands were carefully selected in order to synthesise high-nuclearity metal clusters.

Chapter 3: Structure and magnetic properties of lanthanide aggregates

3.1 Introduction

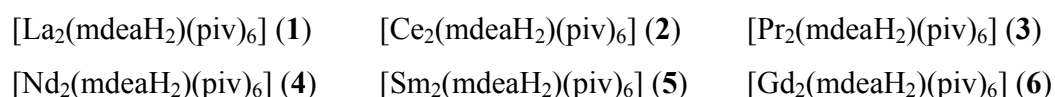
Lanthanide coordination complexes are very interesting from both a theoretical and a practical point of view. In the lanthanide series the electrons of $4f$ sub-shells are practically part of the core; therefore the $3+$ oxidation state dominates their chemistry. Gradual changes can be observed between the elements, which can be attributed to the ionic radius decreasing with the atomic number due to lanthanide contraction along the series. The similar chemical properties of the lanthanide elements are due to shielded $4f$ electrons. Electrostatic interactions play an important role in complex formation, and the most stable complexes are formed with ligands bound via O and N atoms. Lacking geometry constraints imposed by ligand field effects, they form complexes with high coordination number, often eight-coordinated with either bicapped trigonal-prismatic (BCTP) or dodecahedral (Dod) geometry or nine coordinated with tricapped trigonal-prismatic (TCTP) geometry.^[89] Recently, studies of a dysprosium triangle system displayed a vanishing susceptibility at low temperature, which is unprecedented in systems comprising an odd number of unpaired electrons.^[37] In spite of the diamagnetic ground state, features typical of single molecule magnet (SMM) behaviour were observed for the thermally-populated excited state, suggesting that a resonant under-barrier relaxation process is also active.^[37] Inspired from these results, more efforts have been devoted to lanthanide chemistry. Here, structure and magnetic studies carried out on three series of complexes are reported. The first series comprises dinuclear lanthanide (Ln) compounds containing the early lanthanides (La-Gd) whereas the second series consists of isostructural tetranuclear Ln(III) complexes containing the later lanthanides (Tb-Tm). The third series was obtained by using a different co-ligand, and it comprises another set of tetranuclear Ln(III) complexes containing the late lanthanides. These series allow the changes in magnetic properties on varying the lanthanide within a series of isostructural complexes to be evaluated.

3.2 Structure and magnetic properties of $[\text{Ln}_2(\text{mdeaH}_2)(\text{piv})_6]$

As discussed in Chapter 1, *N*-methyldiethanolamine (mdeaH_2) has been used in reaction systems with $3d$ transition metal elements, but surprisingly it has been so far completely ignored

in Ln(III) chemistry. A significant degree of control can be exerted over the formation of low-nuclearity molecular cluster-aggregates by using selected polyfunctional ligands and Ln(III) salts in acetonitrile.

The reactions of $\text{Ln}(\text{NO}_3)_3 \cdot x\text{H}_2\text{O}$ ($\text{Ln} = \text{La, Ce, Pr, Nd, Sm}$) with mdeaH_2 and pivalic acid (pivH) with a ratio of (1:5:3) in acetonitrile and in the absence of base yielded the dinuclear compounds $[\text{Ln}_2(\text{mdeaH}_2)(\text{piv})_6]$. The analogous Gd complex was obtained by using a $\text{Gd}(\text{NO}_3)_3 \cdot x\text{H}_2\text{O}:\text{mdeaH}_2:\text{pivH}$ ratio of (1:3:3) in a mixture of $\text{CH}_2\text{Cl}_2/\text{MeCN}$ (1:1). Using this method, the following pivalate-bridged dinuclear clusters have been synthesised:



3.2.1 Structure of $[\text{Ln}_2(\text{mdeaH}_2)(\text{piv})_6]$ (1-6)

The structures of **3** and **6** were determined by single-crystal X-ray diffraction. These two compounds are isomorphous, crystallising in the monoclinic space group $P2_1/n$ with $Z = 2$. X-ray powder diffraction indicated that all six compounds in the series were isomorphous (Fig. 3.2). Selected bond distances of both compounds are given in Table 3.1 and the structure of **3** is discussed in detail here. The crystal structure of **3** showed the formation of the dinuclear complex $[\text{Pr}_2(\text{mdeaH}_2)_2(\text{piv})_6]$ (Fig. 3.1). The two halves of the complex are related by a crystallographic inversion centre at the midpoint of the Pr---Pr vector. The Pr atoms are each chelated by a diethanolamine ligand, in which both oxygens are still protonated (mode IX in Fig. 1.10),^[85,86] with a Pr(1)-O(1) bond and a Pr(1)-O(2) bond of 2.5714(12) Å and 2.5754(13) Å, respectively. The Pr centres are then bridged by two pairs of pivalate ligands. One of these forms a rather symmetrical *syn-syn* bridge: Pr(1)-O(5) = 2.4647(12) and Pr(1)-O(6) = 2.3860(12) Å. The second pair of pivalates are best described as chelating semibridging, since in addition to the two typical Pr-O bonds, Pr(1)-O(3) = 2.3850(12) and Pr(1)-O(4) = 2.4714(12) Å, there is now a further weak Pr-O interaction, with Pr(1)-O(3') = 2.9047(13) Å and a Pr(1)-O(3')-Pr(1') angle of 102.71(4)°. The coordination sphere around Pr(1) is completed by a further monodentate pivalate ligand. The metal coordination geometry can best be described as a tri-capped trigonal prism. As expected, the Pr-O distances to the uncharged diethanolamine oxygens are significantly longer than those to the pivalate oxygens, while the Pr-N distance is longer still, reflecting the lower affinity of lanthanide cations for nitrogen. The Pr(1)---Pr(1') distance is 4.1440(2) Å. The structure of **3** is

stabilised by hydrogen bonds from the mdeaH₂ ligands. The hydroxyl group of O(1) makes an intramolecular hydrogen bond to the non-coordinated carboxyl oxygen atom O(8) of the monodentate pivalate ligand coordinated to the same Pr centre, while that of O(2) makes an intermolecular hydrogen bond to O(8) of the neighbouring molecule at $\{-x + 1/2, y + 1/2, -z + 1/2\}$. Each binuclear complex is thus linked by hydrogen bonds to four other dimers, resulting in a 2D supramolecular structure corresponding to layers parallel to $\{10\bar{1}\}$ (Fig. 3.3).

In the structure of **6**, the Gd(1)-O(3') distance, 3.1434(17) Å, is now too long to relate to any significant interaction, and this pivalate can thus also be described as making a simple *syn-syn* bridge. Gd(1) is therefore eight-coordinate, consistent with its smaller ionic radius relative to Pr(1). The Gd---Gd distance, 4.1952(3) Å, is longer than the Pr---Pr distance in **3**, presumably reflecting the loss of the weak bridging interaction through O(3'), since the lanthanide contraction alone would be expected to result in a slightly shorter Ln---Ln distance in **6** compared to **3**.

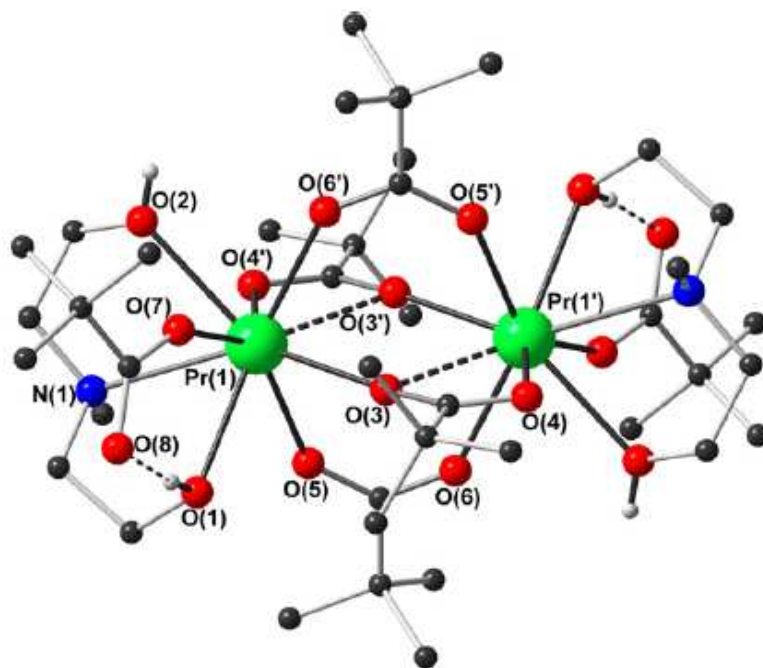


Fig. 3.1 Crystal structure of $[\text{Pr}_2(\text{mdeaH}_2)_2(\text{piv})_6]$ (**3**). Methyl groups corresponding to the minor disorder component of the two pivalate ligands and all H atoms are omitted for clarity. Grey, red, blue, and green spheres represent C, O, N and Pr, respectively.

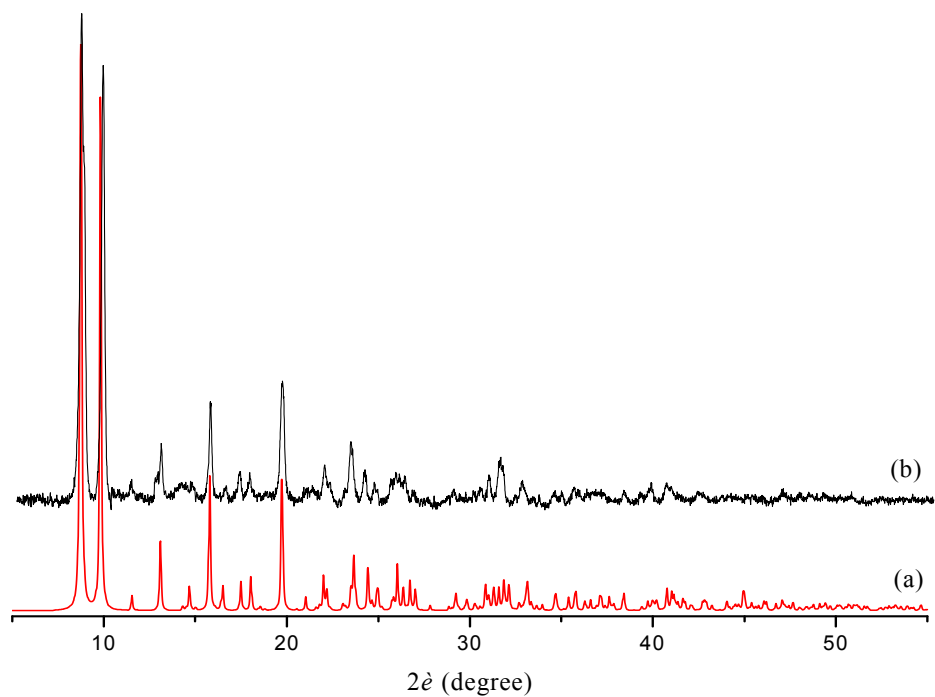


Fig. 3.2 X-ray powder diffraction: (a) calculated for **3** based on the single crystal X-ray structure; (b) measured for complex **2**.

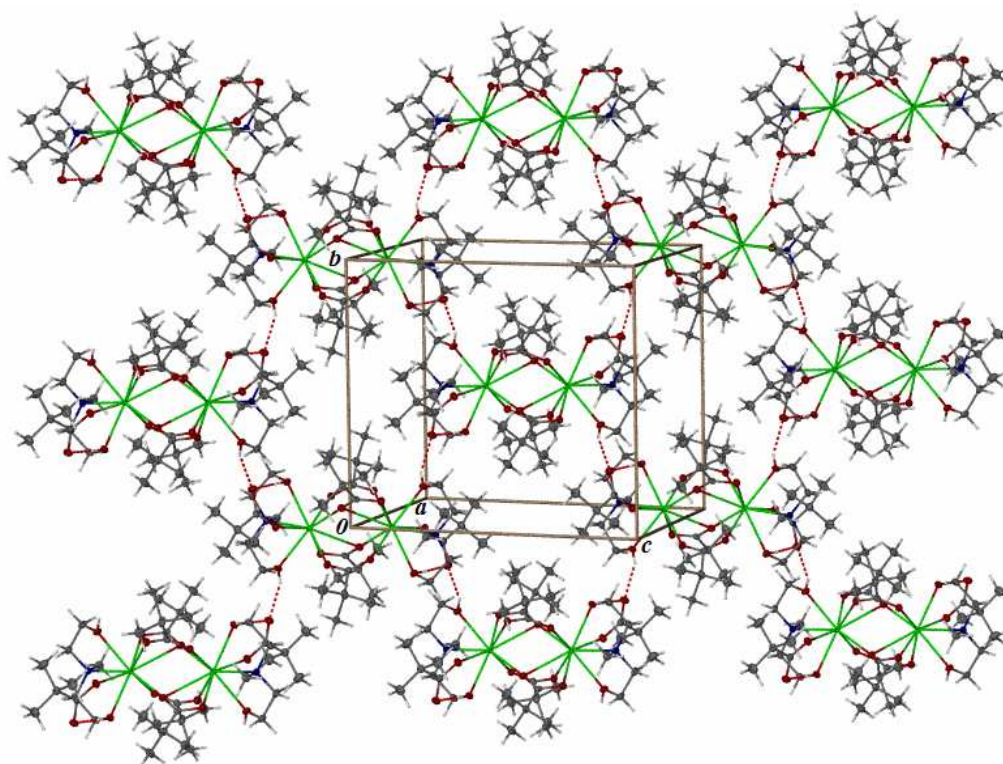


Fig. 3.3 The 2D supramolecular structure for **3** showing the hydrogen bonds as red dotted lines.

Table 3.1 Selected bond distances (Å) for complexes of compounds **3** and **6**.

Compound	3 (Ln = Pr)	6 (Ln = Gd)
Ln(1)-N(1)	2.8200(16)	2.724(2)
Ln(1)-O(1)	2.5714(12)	2.5075(17)
Ln(1)-O(2)	2.5754(13)	2.5090(17)
Ln(1)-O(3)	2.3850(12)	2.2799(16)
Ln(1)-O(3')	2.9047(13)	3.1434(17)
Ln(1)-O(4')	2.471(12)	2.3890(16)
Ln(1)-O(5)	2.4647(12)	2.3891(16)
Ln(1)-O(6')	2.3860(12)	2.3148(16)
Ln(1)-O(7)	2.4480(13)	2.3708(17)
Ln(1)---Ln(1')	4.1440 (2)	4.1952(3)

3.2.2 Magnetic properties of [Ln₂(mdeaH₂)(piv)₆] (Compounds 1-6).

Variable temperature dependence of the magnetic susceptibility was carried out on polycrystalline powder samples of **1-6** in the temperature range 1.8-300 K at 1000 Oe. Of this series of compounds, La₂ (**1**) is a diamagnetic compound, thus its magnetic susceptibility ($\chi_{La_2} = \chi_{dia} = 8.8 \times 10^{-4} \text{ cm}^3 \text{ mol}^{-1}$) was used to correct for the diamagnetic contribution of this system. At room temperature, the experimental χT products are all more or less close to the expected values^[40] as can be seen in Table 3.2. On lowering the temperature, the χT product decreases down to 1.8 K for compounds **1-5**. For Gd₂ (**6**), it stays constant until 10 K and then slightly increases to reach $16.8 \text{ cm}^3 \text{ K mol}^{-1}$ at 1.8 K (Fig. 3.4). The Stark sublevels of the anisotropic Ln (Ce, Pr, Nd and Sm) ions are thermally depopulated when the temperature is lowered resulting in a decrease of the χT versus T plot.^[90] Therefore, even if the χT product decreases with the temperature and reaches a minimum value at 1.8 K, it is uncertain whether this behaviour can be associated with dominant antiferromagnetic interactions between the two Ln(III) ions within complexes **1-5**. However, in the case of Gd₂ (**6**), the slight increase of the χT product at low temperature indicates at most a weak ferromagnetic interactions. As Gd(III) has essentially no orbital contribution, it can be considered as an isotropic $S = 7/2$ spin. Hence for this compound, the magnetic behaviour can be analysed using a simple isotropic Heisenberg Hamiltonian:

$$H = -2JS_{Gd}S_{Gd'}$$

where J is the exchange interactions in the dimer between the Gd(III) ions as seen in Fig. 3.1. The application of the van Vleck equation^[96] to the Kambe's vector coupling scheme^[92] allows a determination of the low-field analytical expression of the magnetic susceptibility:^[46,47,48]

$$\chi_{Gd2} = \frac{g^2 N \mu_B^2}{k_B T} \frac{2e^{\frac{2J}{k_B T}} + 10e^{\frac{6J}{k_B T}} + 28e^{\frac{12J}{k_B T}} + 60e^{\frac{20J}{k_B T}} + 110e^{\frac{30J}{k_B T}} + 182e^{\frac{42J}{k_B T}} + 140e^{\frac{56J}{k_B T}}}{1 + 3e^{\frac{2J}{k_B T}} + 5e^{\frac{6J}{k_B T}} + 7e^{\frac{12J}{k_B T}} + 9e^{\frac{20J}{k_B T}} + 11e^{\frac{30J}{k_B T}} + 13e^{\frac{42J}{k_B T}} + 15e^{\frac{56J}{k_B T}}}$$

This model was able to reproduce the experimental data from 300 K to 1.8 K very well (Fig. 3.5). The best set of parameters found are $J/k_B = 0.005(5)$ K (ca. 0.0035 cm^{-1}) and $g = 2.03(1)$. The sign of the magnetic interaction confirms the two Gd(III) ions in this compound are very weakly ferromagnetically coupled or else decoupled. The magnitude of the interaction between the Gd(III) centres can be compared with those obtained for similar systems such as 0.015 cm^{-1} for $\text{Gd}_2(\text{PhOCH}_2\text{COO})_6(\text{H}_2\text{O})_3 \cdot \text{H}_2\text{O}$ ^[47], 0.039 cm^{-1} for $[\text{Gd}(\text{Hcit})(\text{H}_2\text{O})_2 \cdot \text{H}_2\text{O}]_n$, where $\text{Hcit}^{3-} = \text{C}(\text{OH})(\text{COO}^-)(\text{CH}_2\text{COO}^-)_2$ ^[48] and -0.020 cm^{-1} for $\text{Gd}_2(\text{ClH}_2\text{CCOO})_6(\text{bipy})_2$.^[46]

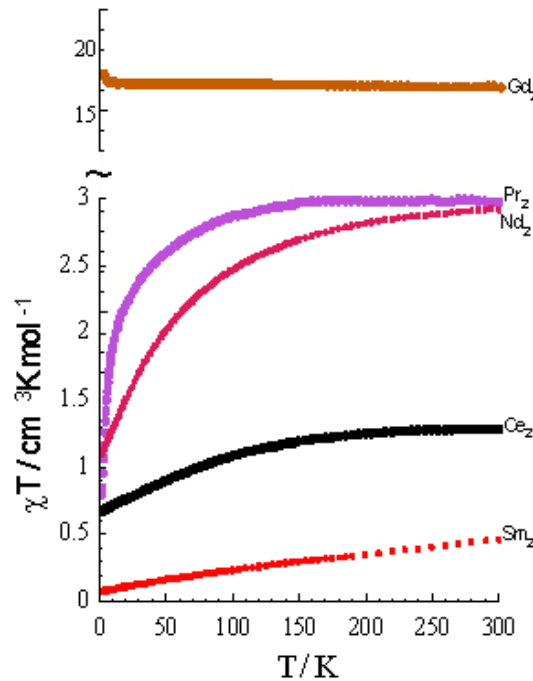


Fig. 3.4 Temperature dependence of χT product for 1-6 at 1000 Oe.

Table 3.2 Comparison of the χT products at room temperature between the expected^[93] and the experimental values for compounds **1–6**.

Compound	χT (cm ³ K mol ⁻¹) theoretical value for each Ln ion at room temperature ^[98]	χT (cm ³ K mol ⁻¹) expected value for Ln ₂ compound at room temperature	χT (cm ³ K mol ⁻¹) experimental value for Ln ₂ compound at room temperature
Ce ₂ (2)	0.80	1.60	1.29
Pr ₂ (3)	1.60	3.20	2.98
Nd ₂ (4)	1.64	3.28	2.93
Sm ₂ (5)	0.09	0.18	0.46
Gd ₂ (6)	7.875	15.75	16.16

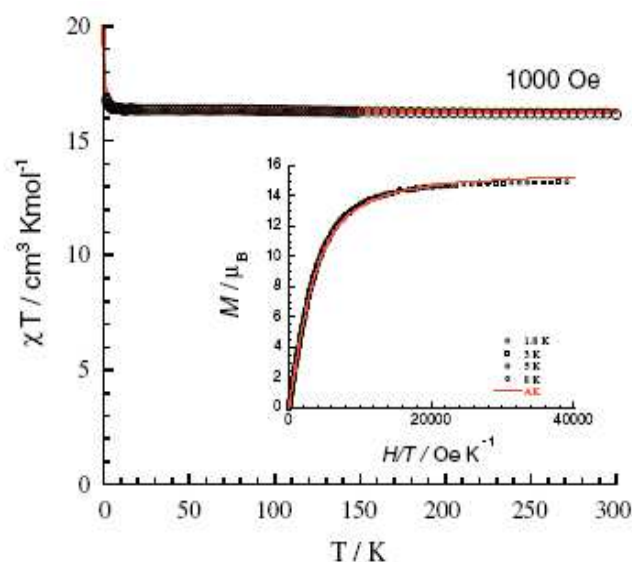


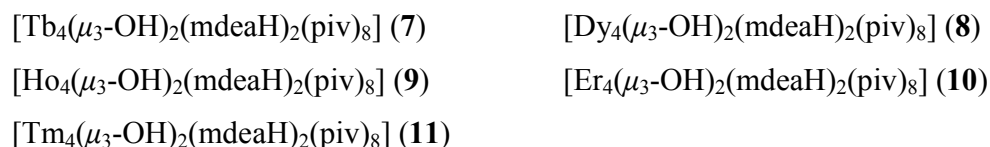
Fig. 3.5 Temperature dependence of the χT product for compound Gd₂ (**6**) at 1000 Oe; Inset: the fit of the Brillouin function to the M versus H/T data of compound **6**. The solid line is the best fit; the dots are the experimental data.

The field dependence of the magnetisation at low temperatures shows that the magnetisation increases smoothly with the applied dc field without saturation even at 7 T where it reaches the value of 1.8, 2.3, 2.6 and 0.4 μ_B for compounds **2**, **3**, **4** and **5**, respectively. This behaviour indicates the presence of magnetic anisotropy and/or the lack of a well-defined ground state, suggesting the presence of low-lying excited states that might be populated when a field is applied. However, for compound **6**, the field dependence of the magnetisation at low temperatures shows that the magnetisation rapidly increases with the applied dc field to approach a true saturation above 2 T at which it reaches the value of 14.8 μ_B . This reveals the absence of

magnetic anisotropy within this compound. The M versus H/T plots further confirm this result, as the data are almost completely superposed on a single master-curve as expected for an isotropic system. The fit of the M versus H/T data by the sum of two simple $S = 7/2$ Brillouin functions leads to a good agreement with the experimental data in the range of 1.8-8 K (see Fig. 3.5 inset) by fixing g to 2.03, which is the same value as that obtained from the fit of the susceptibility. It is worth noting that the fit of the M versus H/T data with a simple $S_T = 7$ Brillouin function does not reproduce the experimental data at all, confirming that the two Gd(III) ions are essentially uncoupled.

3.3 Structure and magnetic properties of $[\text{Ln}_4(\mu_3\text{-OH})_2(\text{mdeaH})_2(\text{piv})_8]$

Our previous studies on the lighter lanthanide series on compounds **1-6** revealed the formation in non-aqueous conditions of isostructural lanthanide dimers of general formula $[\text{Ln}_2(\text{mdeaH})_2(\text{piv})_6]$. These lanthanides ions are connected by *syn-syn* carboxylate bridges and this type of bridge mediates vanishingly small magnetic interactions.^[94] Synthetic attempts were extended to the heavier lanthanide homologues (Tb-Tm). In this case, a $\text{LnCl}_3 \cdot x\text{H}_2\text{O}:\text{mdeaH}_2:\text{pivH}$ ratio of (1:5:3) yielded the isostructural $[\text{Ln}_4(\mu_3\text{-OH})_2(\text{mdeaH})_2(\text{piv})_8]$ compounds:



3.3.1 Structure of $[\text{Dy}_4(\mu_3\text{-OH})_2(\text{mdeaH})_2(\text{piv})_8]$ (8)

X-Ray crystallographic structure determinations were carried out for all five compounds and showed a tetranuclear structure $[\text{Ln}_4(\mu_3\text{-OH})_2(\text{mdeaH})_2(\text{piv})_8]$, where Ln = Tb (7), Dy (8), Ho (9), Er (10) and Tm (11). The five compounds crystallise isomorphously in the triclinic space group $P\bar{1}$, with $Z = 1$. All five clusters are thus isostructural, thus only the structure of **8** is discussed in detail. The molecular structure of **8** is depicted in Fig. 3.6. It has a crystallographically centrosymmetric $[\text{Dy}^{\text{III}}_4(\mu_3\text{-OH})_2]^{10+}$ “butterfly” core. Although a literature survey revealed that this type of core is very common for $3d$ elements, such as Cr,^[95] Mn,^[96,97]

and Fe^[98,99], such a core for 4*f* elements is very rare.^[101,102] Charge compensation of all clusters requires two singly deprotonated *N*-methyldiethanolamine ligands and eight pivalate anions.

The topological presentation of the [Dy₄^{III} (μ₃-OH)₂]¹⁰⁺ core can be described as a “butterfly” structure (Fig. 3.7). The body is formed by Dy(1) and Dy(1′), while Dy(2) and Dy(2′) occupy the wing-tips, and the four Dy atoms are exactly coplanar as a result of the crystallographic inversion symmetry. The two μ₃-OH⁻ ions are displaced above and below the Ln₄ plane (Table 3.3). The sum of the Ln-O-Ln angles around the μ₃-OH⁻ ions is close to the ideal value of 328.4° expected for pure *sp*³ hybridization. Each μ₃-OH⁻ ion makes two short Dy(1′)-O(1), Dy(2)-O(1) (2.334, 2.378 Å) and one longer Dy(1)-O(1) (2.448 Å) distances. In this way, the coordination number around each Dy(III) ion is eight (DyO₈ for Dy(1) and DyO₇N for Dy(2)). A detailed analysis of the molecular geometry^[102,103] reveals that Dy(1) has a geometry between Dod and BCTP coordination environments (φ angles 2.39° and 11.99°, dihedral angles 26.11°, 38.84°, 41.46°, 43.08°) and that Dy(2) has a distorted dodecahedral (Dod) coordination environment (φ angles 0.23° and 3.03°, dihedral angles 13.66°, 32.39°, 32.42°, 44.52°).

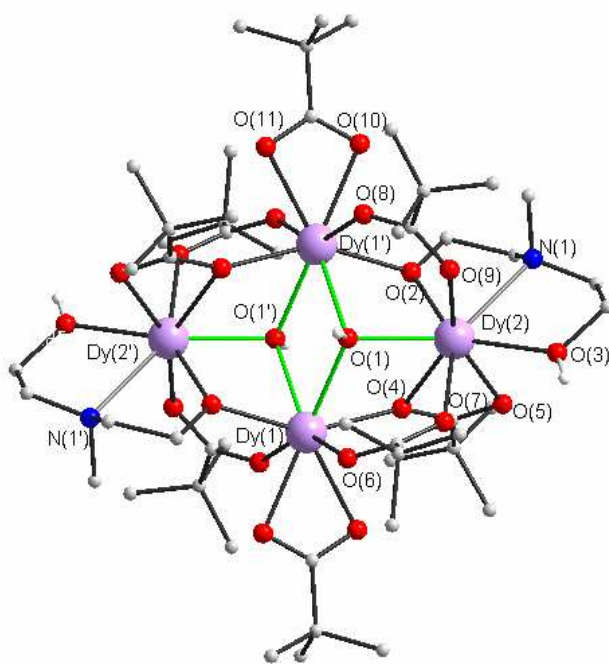


Fig. 3.6 Molecular structure of **8**. lavender, red, blue and grey spheres represent Dy, O, N and C, respectively. All H atoms are omitted for clarity.

The two central Dy(III) ions [Dy(1) and Dy(1')] are bridged by the two μ_3 -OH⁻, while a single μ_3 -OH⁻ ion participates in the coordination sphere of the wing Dy(III) ions, resulting in shorter distances in the body-to-wing separation relative to larger central Dy(1)---Dy(1') separation. The wing-to-wing separation is the largest one, as expected, ranging from 6.232(5) to 6.346(1) Å. Peripheral ligation is provided by eight piv⁻ and two singly deprotonated mdeaH⁻ ligands. The deprotonated arm of each monodeprotonated mdeaH⁻ ligand, forms a bridge, O(2) between Dy(1) and Dy(2) with the deprotonated arm, while the protonated arm simply chelating to Dy(1). All four body-wingtip edges are bridged by four pivalates possess a μ_2 ($\eta^1:\eta^1$)-bidentate bridging mode in a *syn-syn* configuration. Moreover, Dy(1), Dy(2') and their symmetry related, are bridged by a bridging/chelating pivalate (Fig.1.12, mode VIII). Finally, the coordination sphere of Dy(1) and Dy(1') are completed by a chelated pivalate anion.

Table 3.3 Selected distances (Å) and bond angles (°) for the cores of compounds **7–11**.

	7 (Tb)	8 (Dy)	9 (Ho)	10 (Er)	11 (Tm)
Ln(1)--Ln(1')	4.069	4.041	4.023	4.003	3.994
Ln(1)--Ln(2)	3.674	3.651	3.628	3.611	3.601
Ln(1')--Ln(2)	3.861	3.832	3.815	3.798	3.798
O(1)---Ln ₃ plane	0.873	0.871	0.865	0.866	0.852
O(1)-Ln(1)	2.460(11)	2.448(4)	2.430(5)	2.427(4)	2.419(5)
O(1)-Ln(1')	2.354(10)	2.372(4)	2.366(5)	2.357(4)	2.348(5)
O(1)-Ln(2)	2.386(11)	2.334(4)	2.323(5)	2.303(4)	2.296(4)
O(2)-Ln(1)	2.291(11)	2.284(4)	2.270(5)	2.251(4)	2.237(5)
O(2)-Ln(2)	2.261(11)	2.258(4)	2.257(5)	2.243(4)	2.243(5)
O(4)-Ln(1)	2.364(10)	2.370(4)	2.350(5)	2.340(4)	2.341(4)
O(4)-Ln(2)	2.544(11)	2.544(4)	2.530(6)	2.510(5)	2.515(5)
Ln(1)-O(1)-Ln(2)	101.6(4)	101.74(16)	101.4(2)	101.55(17)	101.69(18)
Ln(2)-O(1)-Ln(1')	106.6(4)	106.49(16)	106.8(2)	106.78(17)	107.30(19)
Ln(1)-O(1)-Ln(1')	114.2(4)	113.91(17)	114.1(2)	113.57(17)	113.8(2)
Ln(1)-O(2)-Ln(2)	107.7(5)	106.99(17)	106.6(2)	106.93(18)	106.99(19)
Ln(2)-O(4)-Ln(1')	103.7(4)	102.41(16)	102.80(19)	103.02(16)	102.86(18)

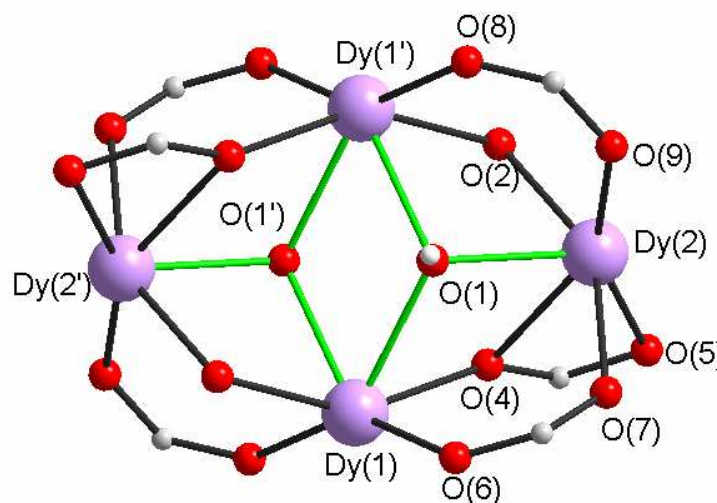


Fig. 3.7 The structure of the $[\text{Ln}^{\text{III}}_4(\mu_3\text{-OH})_2]^{10+}$ butterfly core in **8**, which lies on an inversion center. Dy(1) and Dy(1') represent “body” sites and Dy(2) and Dy(2’) “wingtip” sites.

3.3.2 Magnetic properties of $[\text{Ln}_4(\mu_3\text{-OH})_2(\text{mdeaH})_2(\text{piv})_8]$ (Ln = Tb, Dy, Ho, Er, Tm).

As discussed earlier, all five tetranuclear compounds **7-11** are isostructural, thereby four Ln(III) ions form a planar butterfly core. Variable temperature dc magnetic susceptibility data were collected for **7-11** at the temperature range of 300-1.8 K in an applied field of 1000 Oe (Fig. 3.8). The dc magnetic data are summarised in Table 3.4. Compared with the theoretical values, the observed χT products at room temperature are in good agreement with those. Overall, the temperature dependences of their magnetic susceptibilities show the same thermal evolution in the full temperature range. On decreasing the temperature, the χT product at 1000 Oe steadily decreases till 30 K and then rapidly drops down to 1.8 K. The Stark sublevels of the anisotropic Ln (Tb, Dy, Ho, Er and Tm) ions are thermally depopulated when the temperature is lowered resulting in a decrease of the χT versus T plot.^[90,102] Therefore, even if the χT product decreases with the temperature and reaches a minimum value at 1.8 K, it is uncertain whether this behaviour is associated with dominant antiferromagnetic interactions between the Ln(III) ions within the complexes or with the Ln(III) ions themselves.

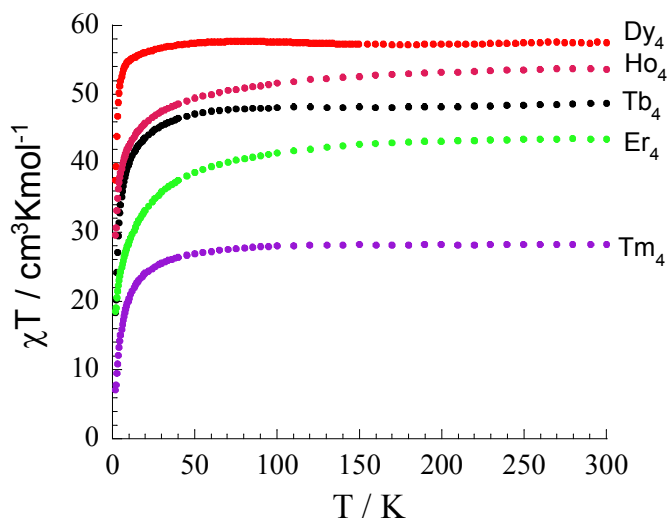


Fig. 3.8 Temperature dependence of the χT products for compounds **7–11** at 1000 Oe.

Table 3.4 Comparison of the dc magnetic data for compounds **7-11**.

Compound	7 (Tb)	8 (Dy)	9 (Ho)	10 (Er)	11 (Tm)
Ground state term with Ln ion	7F_6	$^6H_{15/2}$	5I_8	$^4I_{15/2}$	3H_6
S	3	5/2	2	3/2	1
L	3	5	6	6	5
g	3/2	4/3	5/4	6/5	7/6
C ($\text{cm}^3\text{Kmol}^{-1}$) for each Ln ion ^[98]	11.82	14.17	14.07	11.5	7.15
χT ($\text{cm}^3\text{Kmol}^{-1}$) expected value for 4 non-interacting Ln ₄ at RT	47.28	56.68	56.28	46.0	28.6
χT ($\text{cm}^3\text{Kmol}^{-1}$) experimental value for Ln ₄ at RT	48.4	57.7	53.7	43.4	28.2
χT ($\text{cm}^3\text{Kmol}^{-1}$) experimental value for Ln ₄ at 1.8 K	18.2	37.6	29.6	18.6	7.1
magnetisation (μ_B) observed at 7 T and 1.8 K	22.4	25.6	24.6	21.7	17.9

The field dependence of the magnetisation of compounds **7-11** at low temperatures shows that the magnetisation is smoothly increasing with the applied dc field without saturation even at 7 T (Fig. 3.9-3.13, left). The magnitude of magnetization is given in Table 3.4. This behaviour indicates the presence of magnetic anisotropy and/or the lack of a well-defined ground state suggesting the presence of low-lying excited states that might be populated when a field is applied. Furthermore,

while plotting the M versus H/T at low temperatures for compounds 7-11 (Fig. 3.9-3.13, right), the curves are not superposed as expected for an isotropic system further indicating the presence of magnetic anisotropy and/or low-lying excited states. In addition, the M vs H data at 1.8 K reveals the existence of hysteresis effect with a very small coercive field (about 12 Oe).

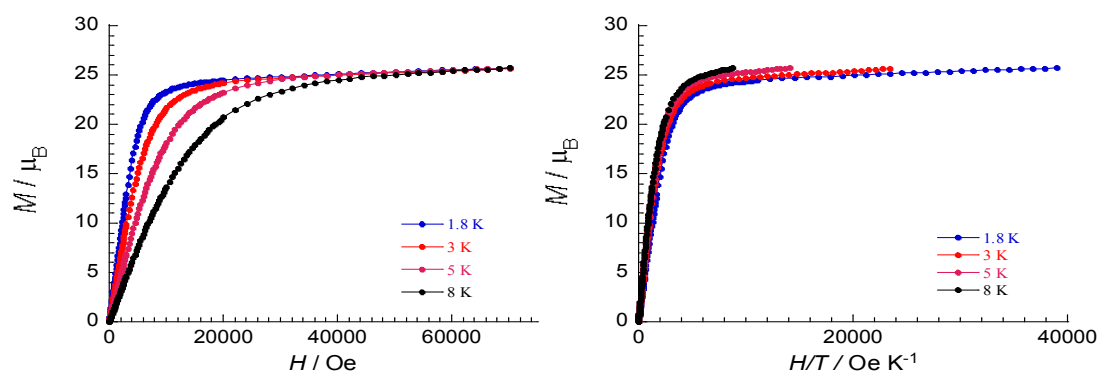


Fig. 3.9 Field dependence of magnetisation at indicated temperatures for compound 7.

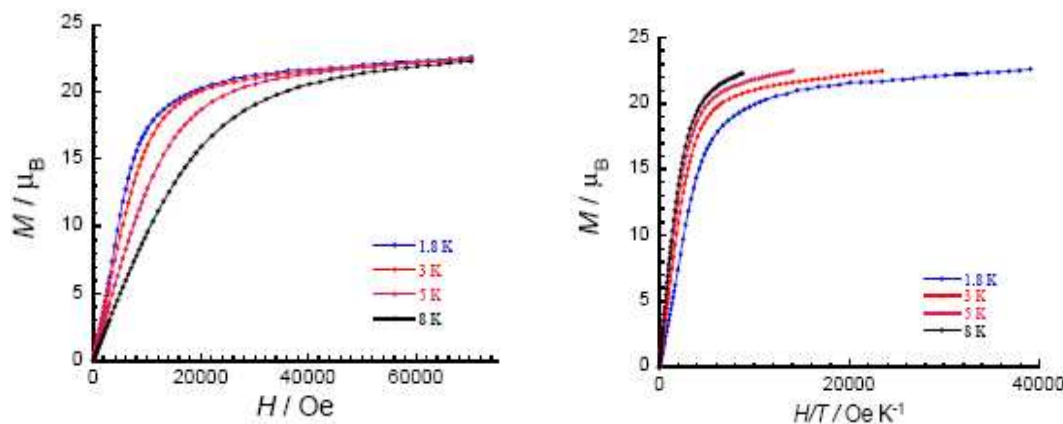


Fig. 3.10 Field dependence of the magnetisation at indicated temperatures for 8.

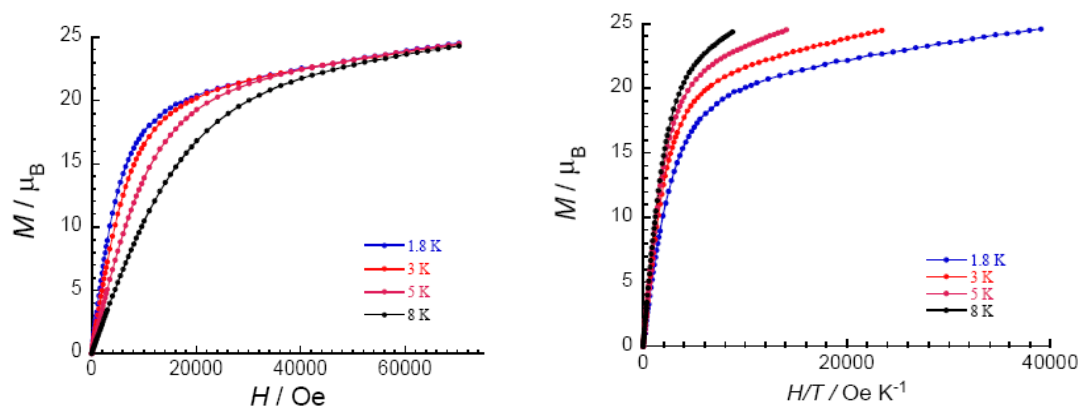


Fig. 3.11 Field dependence of magnetisation at indicated temperatures for compound 9.

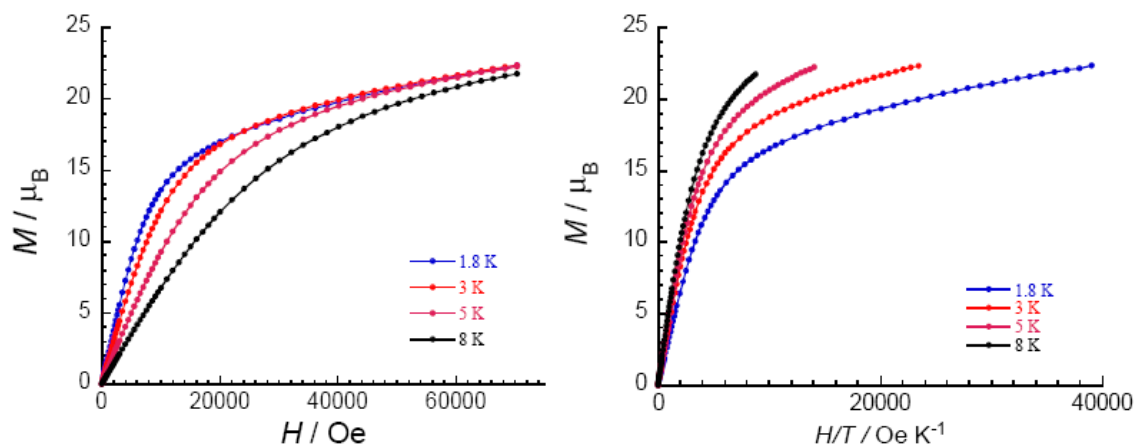


Fig. 3.12 Field dependence of magnetisation at indicated temperatures for compound **10**.

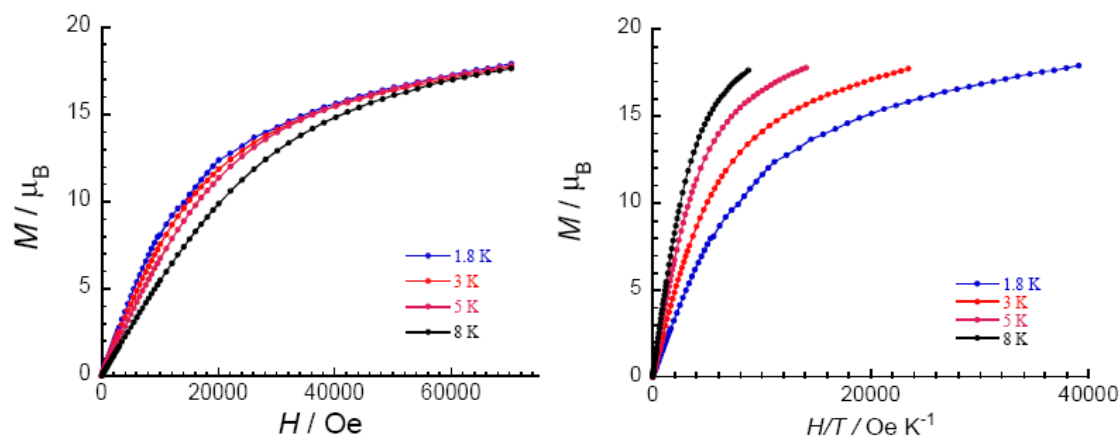


Fig. 3.13 Field dependence of magnetisation at indicated temperatures for compound **11**.

Due to the presence of magnetic anisotropy, the magnetisation relaxation was probed under zero dc field for all compounds **7-11**. Out of them, only compound **8** exhibits slow relaxation of its magnetisation. As shown in Fig. 3.14, frequency dependence of both in-phase and out-of-phase components was observed in zero dc field below 12 K indicating slow relaxation of the magnetisation. The out-of-phase signal possesses a reasonable intensity in comparison to the in-phase signal and its maximum is observed at 2.5 K at a frequency of 1500 Hz. In addition to frequency dependent ac susceptibilities, frequency sweeping ac susceptibilities were also measured at different temperatures (Fig. 3.15). Both the shape and frequency dependence strongly suggests that this compound is a SMM. Fitting the data to an Arrhenius law leads to the characteristic SMM energy gap (Δ) of 6.2 K and the pre-exponential factor (τ_0) of 2.45×10^{-5} s (Fig. 3.16).

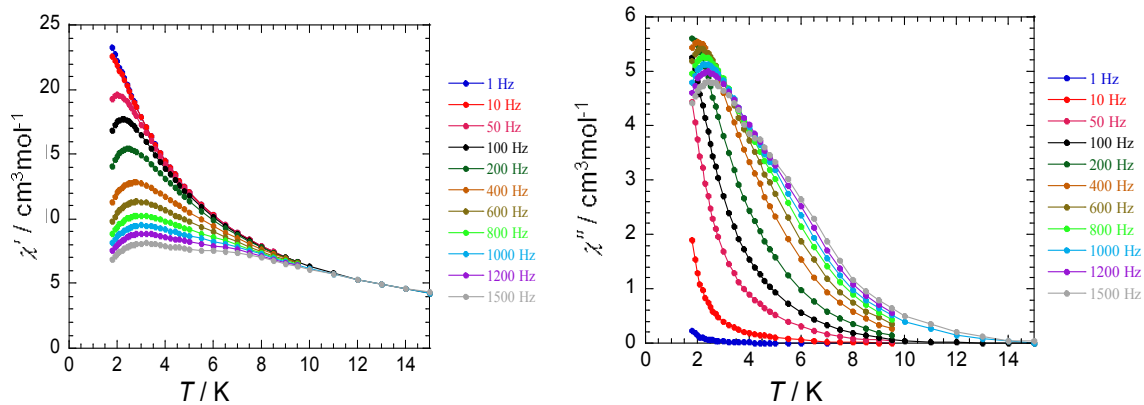


Fig. 3.14 Temperature dependence of the in-phase (left) and out-of-phase (right) components of the ac magnetic susceptibility, for **8** under zero dc field.

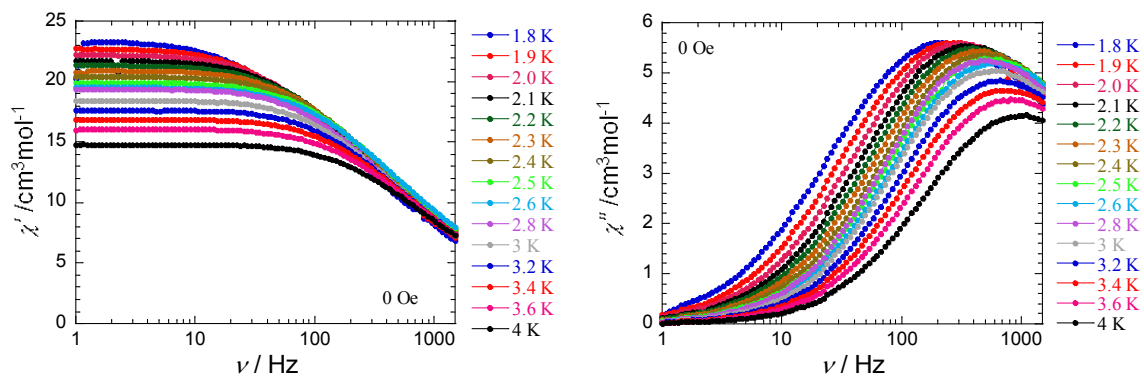


Fig. 3.15 Frequency dependence of the in-phase (left) and the out-of-phase (right) ac susceptibility component at different temperature for compound **8** under zero dc field.

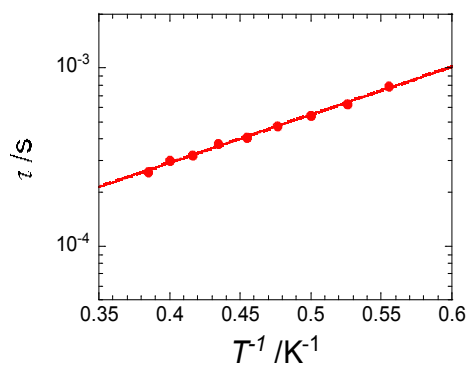


Fig. 3.16 τ versus $1/T$ plot for **8** obtained from frequency dependent ac susceptibilities under zero dc field.

In order to study further this relaxation time and check the quantum tunnelling effect above 1.8 K, frequency dependence of the ac susceptibility at 1.8 K was also measured in the application of a small dc field (Fig. 3.17). In SMMs with a relaxation partially influenced by quantum effects, the application of a small dc field removes the ground state degeneracy and thus the possibility of quantum tunnelling in SMMs inducing a slowing down of the magnetisation relaxation.^[87] In zero field, the characteristic frequency was 240 Hz at 1.8 K. By increasing the field, this frequency decreased to 75 Hz around 800 Oe. The small dc field slows down the relaxation time as has been observed for some SMMs when quantum tunnelling of the magnetisation is suppressed. Therefore, ac susceptibility measurements as a function of temperature were carried out again under a dc field of 800 Oe (Fig. 3.18) in order to estimate the relaxation time. Fitting the data to an Arrhenius law, the characteristic SMM energy gap, Δ , was estimated to be 6.9 K and the pre-exponential factor, τ_0 , 4.8×10^{-5} s (Fig. 3.19). The slight increase of the energy barrier indicates that the quantum tunneling effect in this compound is not very pronounced.

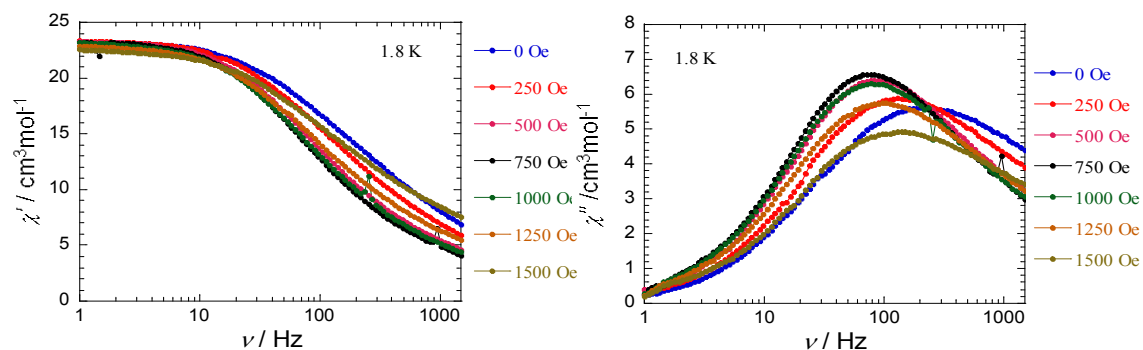


Fig. 3.17 Frequency dependence at 1.8 K of the in-phase (left) and the out-of-phase (right) ac susceptibility components at different dc fields for **8**.

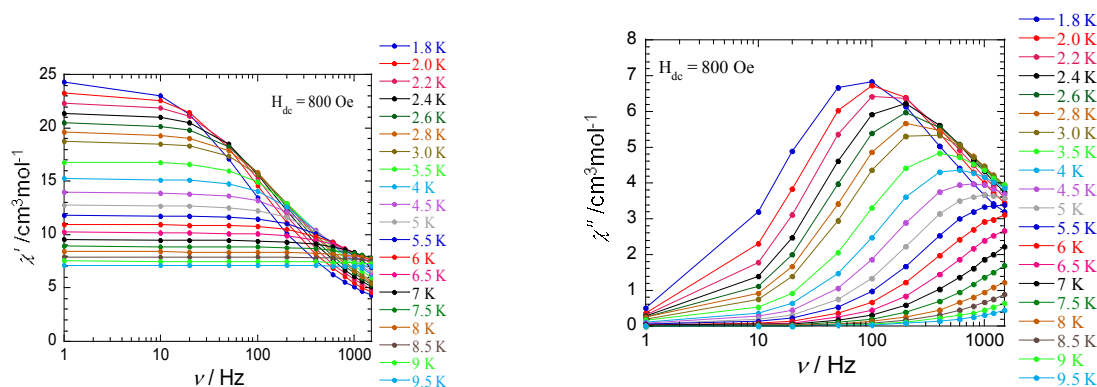


Fig. 3.18 Frequency dependence of the in-phase (left) and the out-of-phase (right) ac susceptibility components at different temperature for compound **8** under dc field of 800 Oe.

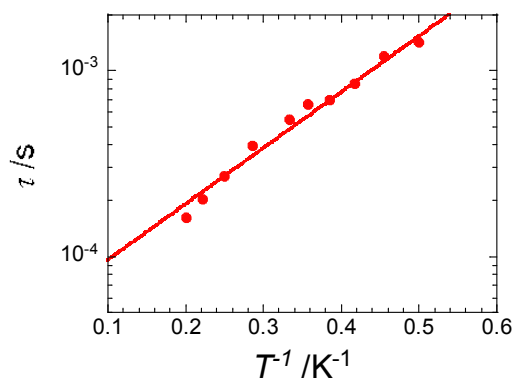
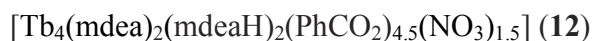
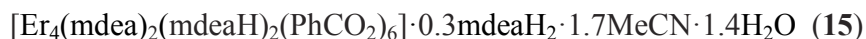
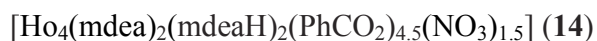
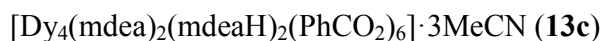
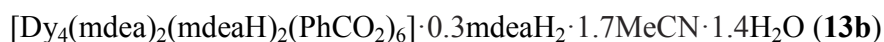


Fig. 3.19 τ versus $1/T$ plot for **8** under 800 Oe dc field obtained from Fig. 3.18.

3.4 Structure and magnetic properties of $[\text{Ln}_4(\text{mdea})_2(\text{mdeaH})_2(\text{PhCO}_2)_6]$

The synthetic method for **1-11** was now extended to develop new systems by varying the carboxylate ligand. In place of pivalic acid, benzoic acid was now used and this resulted in the formation of tetranuclear lanthanide complexes with a non-planar Ln_4 core, in contrast to the planar cores in **7-11**. The reactions of ($\text{Ln} = \text{Tb}, \text{Dy}, \text{Ho}, \text{Er}$) with mdeaH_2 and benzoic acid (PhCO_2H) in a $\text{LnCl}_3 \cdot x\text{H}_2\text{O}:\text{mdeaH}_2:\text{PhCO}_2\text{H}$ ratio of (1:5:1) in acetonitrile yielded the tetranuclear compounds:





The Dy₄ compound **13** has been obtained in three distinct crystallographic phases, **13a**, **13b** and **13c**. It has so far not proved possible to obtain a sample that contains one of the three phases in a pure form; only mixtures have been obtained. The factors determining the relative proportions of each phase from a given preparation require further investigation. However, **13b** appears to be the majority phase. The powder diffraction pattern in Figure 3.20 was recorded from the sample used for the SQUID measurements. The peaks marked with arrows result from **13b**, with some weaker peaks from **13a**, and only a few very weak peaks that can be assigned to **13c**. Moreover, the molecular structures of the Dy₄ aggregates in each of the phases are closely similar.

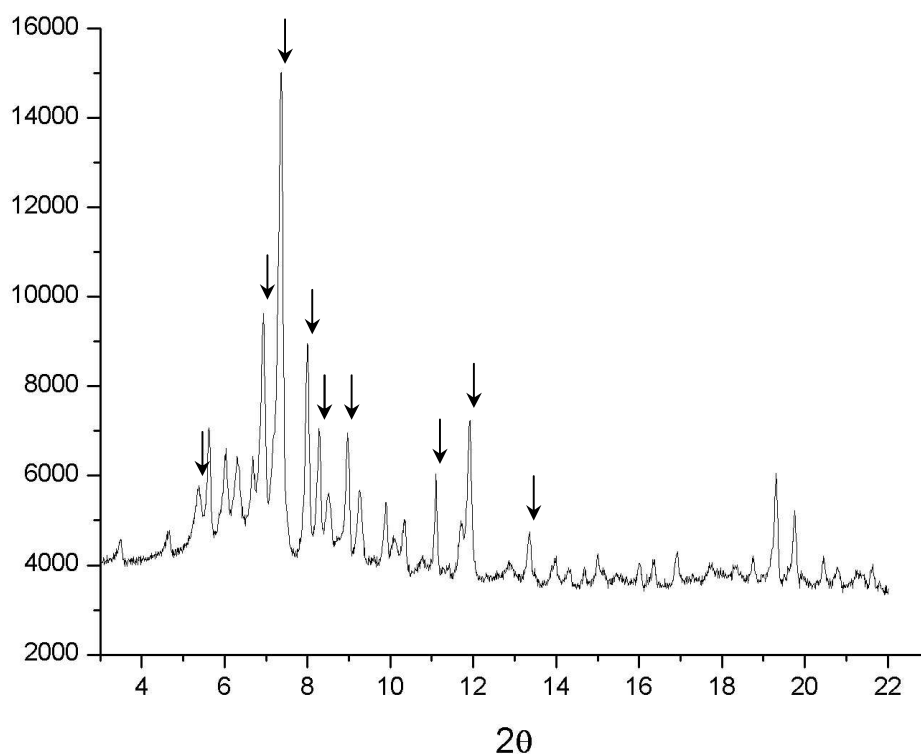


Fig. 3.20 X-ray powder diffraction: for **13** based on the single crystal X-ray structure.

3.4.1 Structure of $[\text{Dy}_4(\text{mdea})_2(\text{mdeaH})_2(\text{PhCO}_2)_6] \cdot 4\text{MeCN}$ (**13a**)

X-ray crystallographic structure studies showed that slightly varying the reaction condition three different products can be obtained **13a**, **13b** and **13c**. All compounds contain a Dy_4 core, although peripheral ligation and solvated molecules are slightly different. The Dy_4 aggregate in **13a** will be described in detail.

The molecular structure of **13a** is depicted in Fig. 3.21. The compound crystallises in the monoclinic $P2_1/n$ space group. The four Dy(III) ions forming the Dy_4 core (Fig. 3.22) are located at four vertices of a defect dicubane or else can be described in terms of a non-planar butterfly core (in contrast to compounds **7-11**). They are bridged by the two deprotonated oxygen atoms from the two mdeaH^- ligands and the totally deprotonated mdea^{2-} ligands. The four Dy(III) ions are non-coplanar with the dihedral angle between the two Dy_3 triangles being $39.01(3)^\circ$. Peripheral ligation is provided by three chelating benzoates, two bidentate *syn-syn* ($\eta^1:\eta^1:\mu_2$) benzoates, one monodentate (η^1) benzoate, two singly deprotonated mdeaH^- ligands and two mdea^{2-} ligands. Atoms O(1) and O(3) ($\mu_3\text{-O}$) of mdeaH^- are triply bridging, resulting in the following Dy---Dy distances Dy(1)-Dy(2) 3.730 Å, Dy(1)-Dy(3) 3.786 Å, Dy(2)-Dy(3) 3.761 Å, Dy(1)-Dy(4) 3.695 Å, Dy(2)-Dy(4) 3.756 Å, respectively. The two Dy_3 triangles do not show a large isosceles distortion, in spite of the differing bridges along the outer edges. As a result of their sp^3 -hybridisation, O(1) and O(3) are displaced above their respective Dy_3 least-squares planes (by 1.03, 1.11 Å, respectively). The doubly bridging oxygens of mdea^{2-} complete the defect dicubane core, with Dy-O distances 2.189-2.337 Å along with the protonated O atoms of the last two mdeaH^- ligands, O(2) and O(4), which are singly coordinated to Dy(3) (2.391 Å) and to Dy(4) (2.394 Å). One benzoate forms comparable bonds coordinated in *syn-syn* mode ($\eta^1:\eta^1:\mu_2$) to Dy(1) and Dy(3) (2.366 Å and 2.336 Å), while bridging Dy-O distances to Dy(4) and Dy(2) in the second bidentate ($\eta^1:\eta^1:\mu_2$) benzoate are notably different (2.281 Å and 2.371 Å). Moreover, one benzoate is chelated to each Dy(1), Dy(2) and Dy(3), while the sixth benzoate is coordinated to Dy(4) in a monodentate mode providing a Dy-O bond distance of 2.247 Å.

Finally, the coordination sphere of the four Dy ions is completed by the four N atoms, belonging to the two mdeaH^- and to the two mdea^{2-} ligands. Therefore, the two mdeaH^- ligands adopt the $\eta^1:\eta^1:\eta^3:\mu_3$ coordination mode (mode VI, Fig. 1.10) and the other two mdea^{2-} bind with the $\eta^2:\eta^1:\eta^2:\mu_3$ mode (mode I, Fig. 1.10). In this way, in the distorted dicubane the coordination number around Dy(1), Dy(2) and Dy(3) ions is eight [DyO_7N] and that of Dy(4) is seven

[DyO₆N]. A detailed analysis of the molecular geometry for each Dy ion^[108,109] reveals that the Dy(1) has a geometry described as being intermediate between D_{4d} and square anti-prismatic(SAP) (φ angles = 6.12° and 25.04°; dihedral angles = 14.39°, 30.73°, 40.21°, 53.58°). Dy(2) (φ angles = 2.18° and 16.51°; dihedral angles = 5.58°, 23.93°, 36.84°, 51.92°) and Dy(3) (φ angles = 5.23° and 14.17°, dihedral angles = 31.00°, 24.04°, 50.98°, 24.55°) each have geometries intermediate between D_{4d} and BCTP. The coordination geometry of Dy(4) can be best described as pentagonal-bipyramidal.

X-ray crystallographic structure studies for other compounds, showed that they consist of tetranuclear Ln₄ non-planar butterfly core, although peripheral ligation and solvated molecules are slightly different comparing to **13a**. Compounds **14** and **16** are isomorphous (monoclinic, *P*2₁/*n*). In both compounds, one of the chelating ligands is benzoate, one is nitrate, and two are a disordered mixture of benzoate (major) and nitrate (minor), with a total nitrate content of 1.5 per cluster. Compounds **13b** and **15** are also isomorphous (monoclinic *P*2₁/*n* but a different unit cell to **12** and **14**).

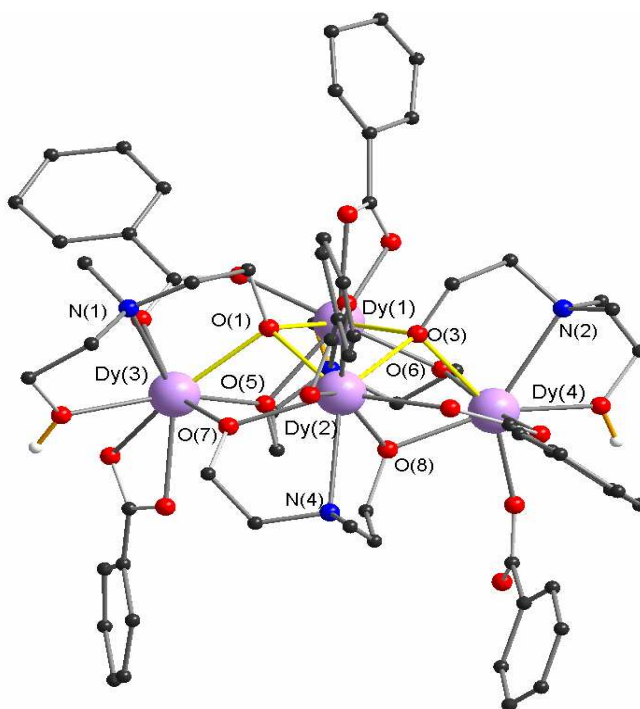


Fig. 3.21 Structure of compound **13a**. Grey, red, blue and lavender spheres represent C, O, N and Dy, respectively.

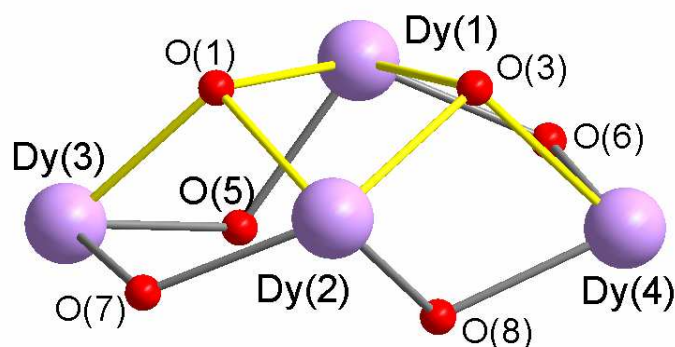


Fig. 3.22 The structure of the Dy₄^{III} core of **13a**.

Table 3.5 Unit cell measurements of compounds **12-15**.

Compounds	12 (Tb)	14 (Ho)	13b (Dy)	15 (Er)
Crystal system	monoclinic	monoclinic	monoclinic	monoclinic
Space group	P2 ₁ /c	P2 ₁ /c	P2 ₁ /n	P2 ₁ /n
a/Å	19.346(3)	19.0132(8)	18.9483(6)	18.9241(9)
b/Å	17.419(2)	17.2017(7)	15.4400(5)	15.3619(9)
c/Å	21.433(3)	21.1723(9)	25.3766(8)	25.3848(8)
β/°	115.166(3)°	114.54(1)	95.164(1)	98.647(1)

3.4.2 Magnetic properties of [Ln₄(mdea)₂(mdeaH)₂(PhCO₂)_{6-x}(NO₃)_x] (**12-15**)

As described in the structural part, the cores of the tetranuclear compounds **12-15** are isostructural and the four Ln(III) ions now form a non-planar Ln₄ core. Overall, the static magnetic behaviour of the compounds in this series is very similar. The temperature dependence of their magnetic susceptibilities show the same thermal evolution in the range of 1.8-300 K (Fig. 3.23). The results are summarised in Table 3.6. On decreasing the temperature, the χT products at 1000 Oe continuously decrease from room temperature till 50 K and then further decrease till 1.8 K, however, in case of the Er analogue, there is a up-turn around 5 K (33.32 cm³ K mol⁻¹). The experimental χT products at room temperature for compound **12-15** are close to the expected values for the presence of four non-interacting Ln(III) ions^[93] as compared in Table 3.6. The Stark sublevels of the anisotropic Ln (Tb, Dy, Ho and Er) ions are thermally depopulated when the temperature is lowered, resulting in a decrease of the χT versus T plot.^[90,102] Therefore even if the χT product decreases with the temperature and reaches a minimum value at 1.8 K, it is

uncertain whether this behaviour is associated with dominant antiferromagnetic interactions between the Ln(III) ions within the complexes or with the individual Ln(III) ions.

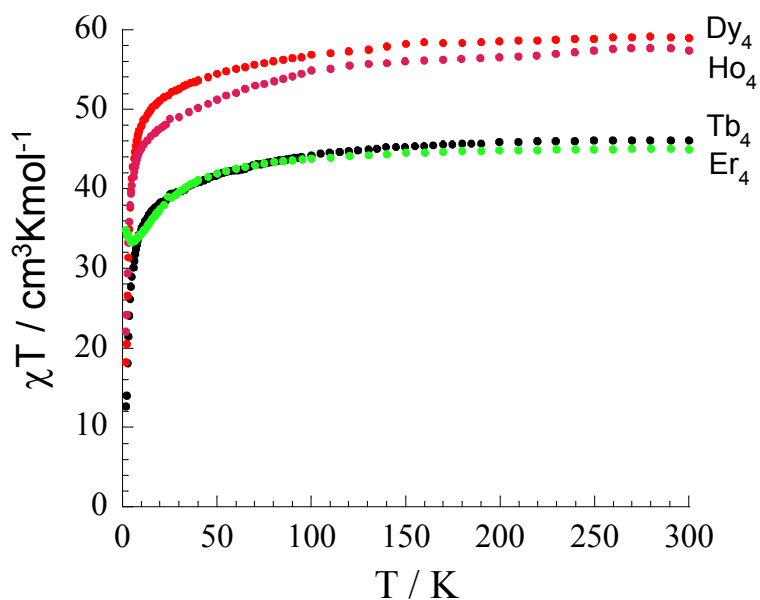


Fig. 3.23 Temperature dependence of the χT products for compounds **14–17** at 1000 Oe.

Table 3.6 Comparison of the dc magnetic data for compounds **12–15**.

Compounds	12 (Tb)	13 (Dy)	14 (Ho)	15 (Er)
Ground state term with Ln ion	7F_6	$^6H_{15/2}$	5I_8	$^4I_{15/2}$
S	3	5/2	2	3/2
L	3	5	6	6
g	3/2	4/3	5/4	6/5
C ($\text{cm}^3\text{Kmol}^{-1}$) for each Ln ion ^[98]	11.82	14.17	14.07	11.5
χT ($\text{cm}^3\text{Kmol}^{-1}$) expected value for 4 non-interacting Ln ₄ at RT	47.28	56.68	56.28	46.0
χT ($\text{cm}^3\text{Kmol}^{-1}$) experimental value for Ln ₄ at RT	45.99	58.95	57.70	44.95
χT ($\text{cm}^3\text{Kmol}^{-1}$) experimental value for Ln ₄ at 1.8 K	12.58	18.28	22.05	34.85
magnetisation (μ_B) observed at 7 T and 1.8 K or 2 K	19.5	25.4	21.8	21.7

The field dependence of the magnetisation at low temperatures shows that the magnetisation smoothly increases with the applied dc field without saturation even at 7 T where it reaches the values for compound **12-15** given in Table 3.6. This behaviour indicates the presence of magnetic anisotropy and/or the lack of a well-defined ground state suggesting the presence of low-lying excited states that might be populated when a field is applied. Moreover, while plotting the M versus H/T at low temperatures for compounds **12-15** (Fig. 3.24-3.27, right), the non-superposed curves indicate the presence of magnetic anisotropy and/or low-lying excited states.

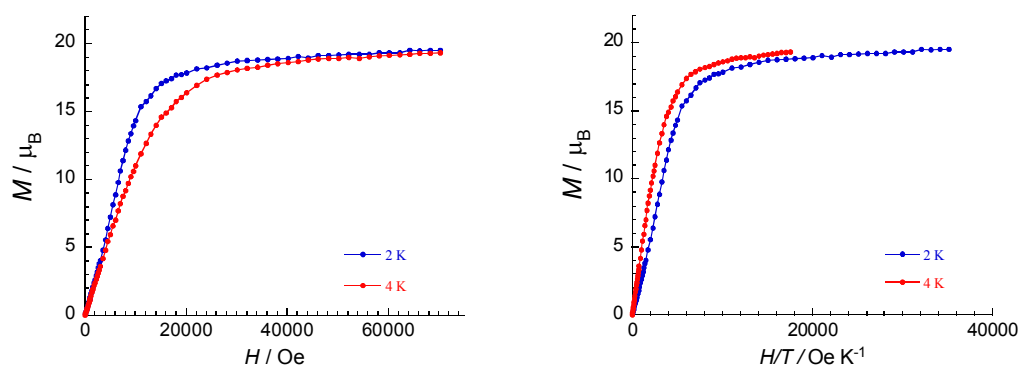


Fig. 3.24 Field dependence of magnetisation at indicated temperatures for compound **12**.

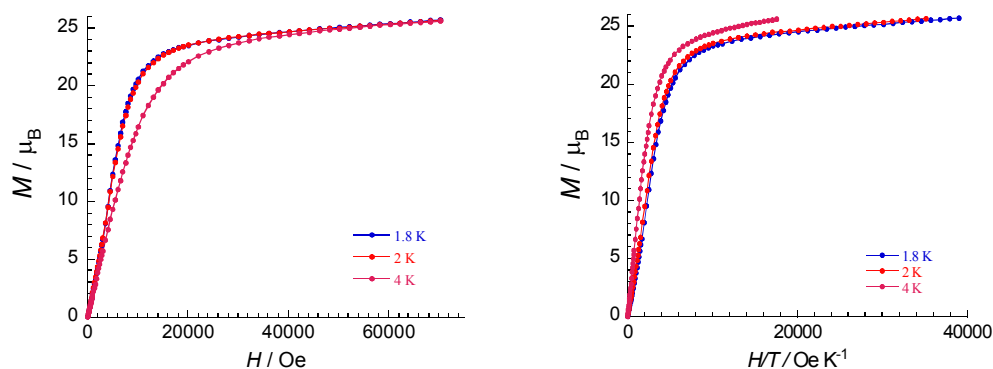


Fig. 3.25 Field dependence of magnetisation at indicated temperatures for compound **13**.

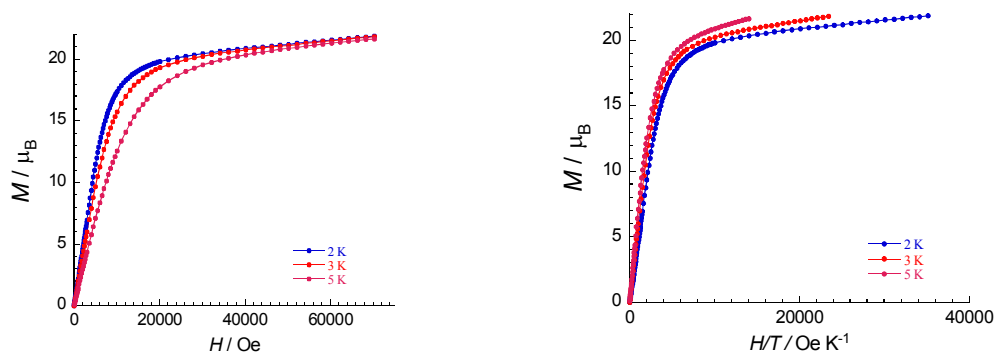


Fig. 3.26 Field dependence of magnetisation at indicated temperatures for compound **14**.

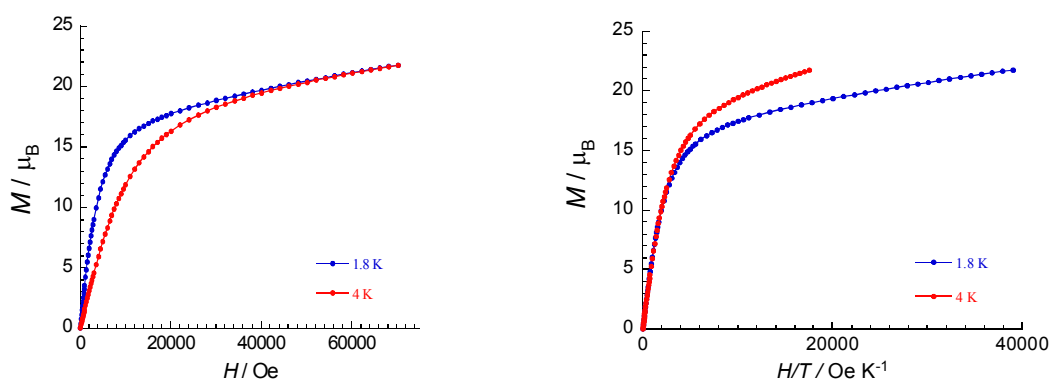


Fig. 3.27 Field dependence of magnetisation at indicated temperatures for compound **15**.

Due to the presence of magnetic anisotropy, the magnetisation relaxation was probed using ac susceptibility measurements as a function of the temperature at different frequencies and also at different temperatures as a function of the frequency. The out-of-phase component is completely absent in compounds **14** and **15**, whilst it is present in compounds **12** and **13**. In zero-dc field, both compounds **12** and **13** show a frequency dependent out-of-phase signal indicating the presence of slow relaxation of the magnetisation. No maximum of out-of-phase signal could be observed in the compound **12** even at 1.8 K (Fig. 3.28) indicating that the block temperature of this compound is below 1.8 K and the energy barrier of the slow relaxation is small.

On the other hand, compound **13** exhibits two maxima of out-of-phase signal observed at 2.5 K and 10 K at a frequency of 1500 Hz (Fig. 3.29). The observed out-of-phase signals possess a reasonable intensity in comparison to the in-phase signal that is also frequency dependent. This feature (shape and frequency dependence) strongly suggests this compound is a SMM. The double maximum could indicate two distinct relaxation processes, one operating at higher, the other at lower temperature. Fitting the frequency sweeping ac susceptibilities as a function of

temperature (Fig. 3.30) by an Arrhenius law, the SMM energy gap (Δ) and the pre-exponential factor (τ_0) are deduced as follows: process 1 (> 5 K): $\Delta_1 = 34.5$ K, $\tau_0 = 1.86 \cdot 10^{-5}$ s; and process 2 (< 5 K): $\Delta_2 = 5.4$ K, $\tau_0 = 8.1 \cdot 10^{-3}$ s (Fig. 3.31). However, as indicated in the structural part, samples of compound **13** form co-crystallised mixtures of the three different species **13a**, **13b** and **13c**. It is more likely, therefore, that the observed double maximum results from the presence of different crystal phases of **13** in the sample, which have different relaxation rates, but it has so far proved impossible to associate energy gaps to particular crystal structures.

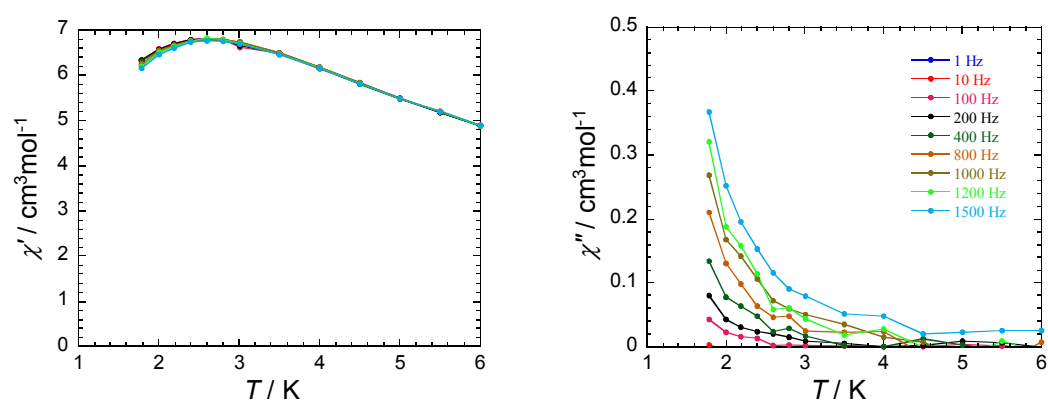


Fig. 3.28 Temperature dependence of the in-phase (left) and out-of-phase (right) components of the ac magnetic susceptibility for **12** under zero dc field.

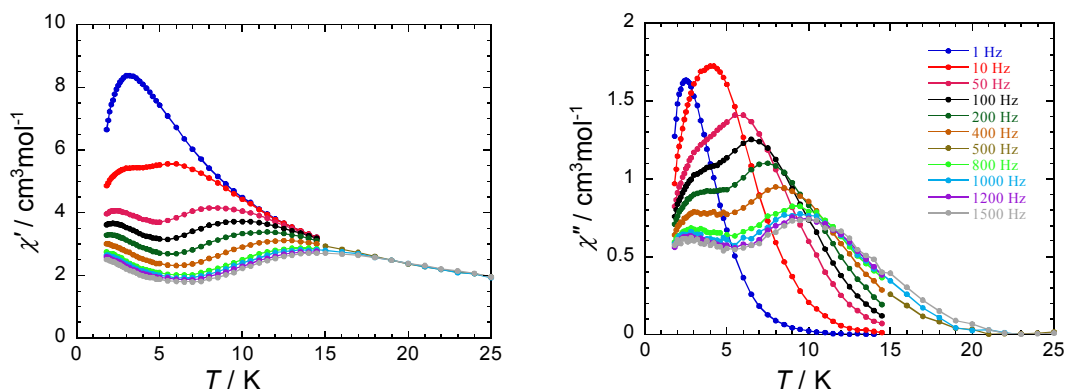


Fig. 3.29 Temperature dependence of the in-phase (left) and out-of-phase (right) components of the ac susceptibility for **13** under zero dc field.

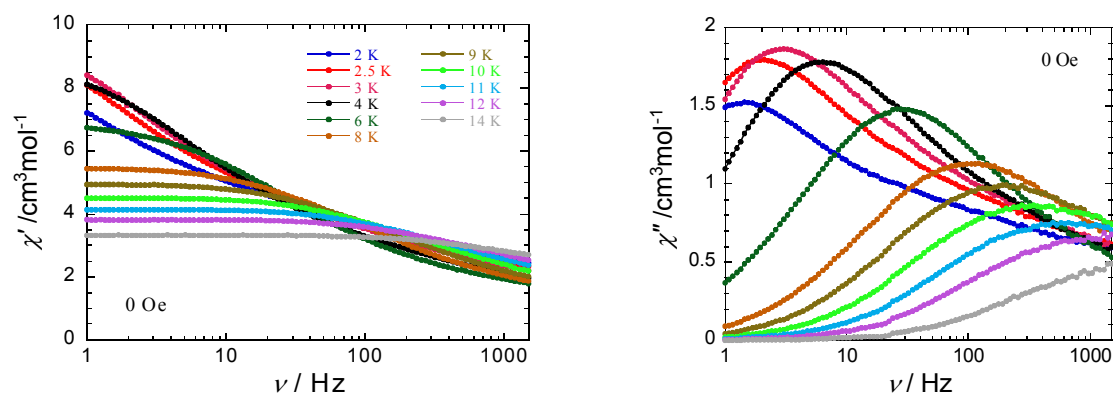


Fig. 3.30 Frequency dependence of the in-phase (left) and the out-of-phase (right) ac susceptibility components at different temperature for compound **13** under zero dc field.

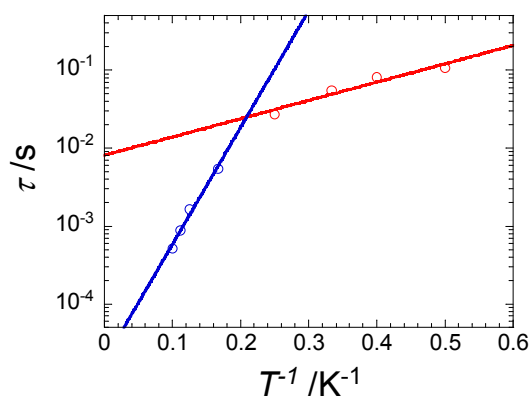


Fig. 3.31 τ versus $1/T$ plot for **13** obtained from frequency dependent ac susceptibility measurements under zero dc field.

In addition, the ac susceptibility measurements under a small dc field were also performed in order to see if the relaxation would slow down. The relaxation mode is almost unchanged in both cases **12** and **13**, indicating that the slow relaxation is fixed with the application of small dc fields (Fig. 3.31-3.33). However, the second relaxation mode of compound **15** at 7 K is only very slightly shifted to higher frequency with the increase of applied dc field (Fig. 3.33). This observation shows that the compounds essentially do not have a relaxation influenced by any quantum effects.

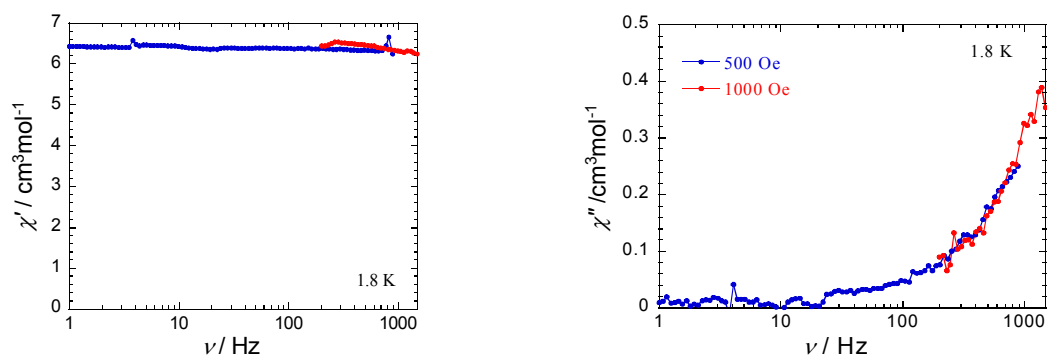


Fig. 3.32 Frequency dependence at 1.8 K of the in-phase (left) and the out-of-phase (right) ac susceptibility components at different dc fields for **12**.

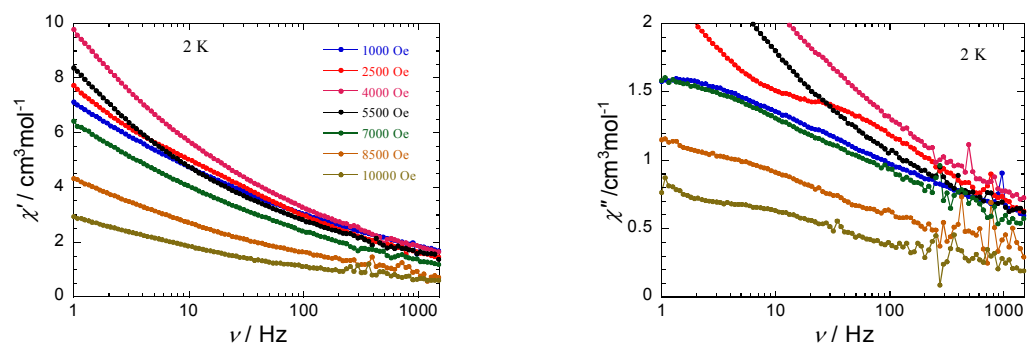


Fig. 3.33 Frequency dependence at 2 K of the in-phase (left) and the out-of-phase (right) ac susceptibility components at different dc fields for **13**.

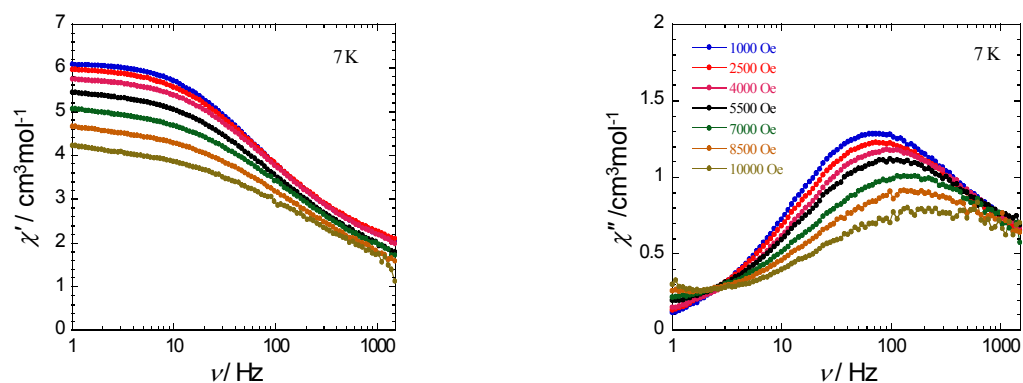


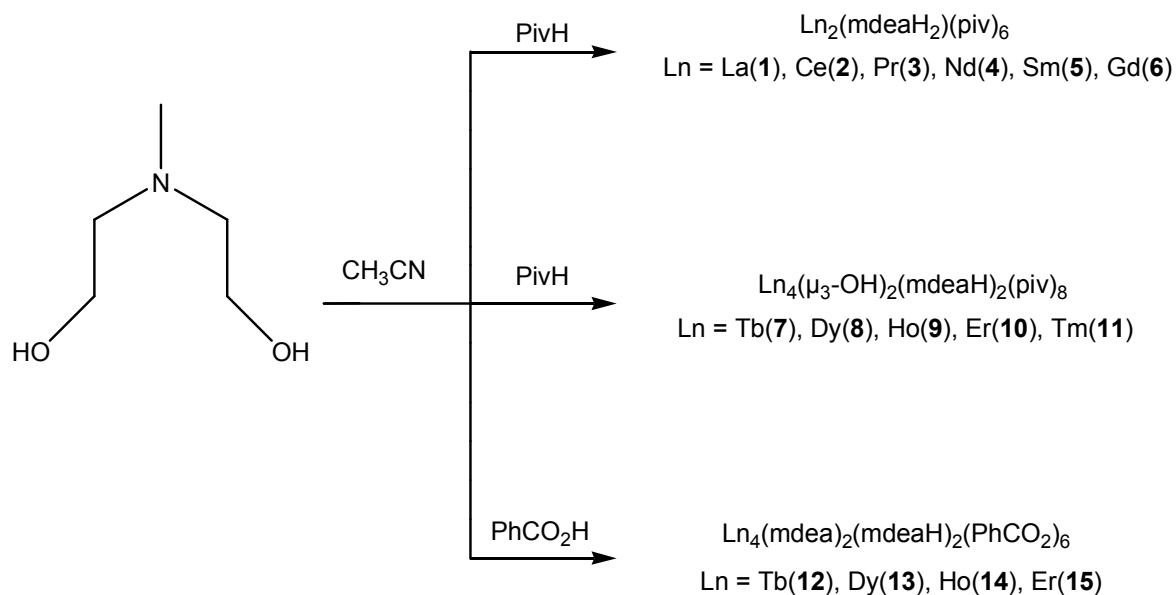
Fig. 3.34 Frequency dependence at 7 K of the in-phase (left) and the out-of-phase (right) ac susceptibility components at different dc fields for **13**.

3.5 Conclusion

In this chapter, a series of six dinuclear $[\text{Ln}_2(\text{mdeaH}_2)(\text{piv})_6]$ (**1-6**), five tetranuclear $[\text{Ln}_4(\mu_3\text{-OH})_2(\text{mdeaH})_2(\text{piv})_8]$ (**7-11**) and four tetranuclear $[\text{Ln}_4(\text{mdea})_2(\text{mdeaH})_2(\text{PhCO}_2)_6]$ (**12-15**) compounds were successfully synthesised, as depicted in Scheme 2, crystallographically characterised and magnetically studied. The dinuclear compounds **1-6** and the tetranuclear compound **7-11** were derived from the same reaction system, so the structure of the final product is presumably a result of the size of the lanthanide cation. For lanthanides with a large radius, dinuclear compounds were isolated while for the heavier, smaller, lanthanides seem to disfavour the dinuclear core, preferring a tetranuclear core. From a magnetic point of view, the exchange coupling between the lanthanides in the dinuclear compounds **1-6** is very weak to the point of being virtually non-existent. Thus it would seem that in complexes of this type the *syn-syn* carboxylate bridges do not allow for any significant magnetic interactions between the lanthanide centres. Magnetically, compounds **7**, **9-11** exhibit antiferromagnetic interactions, and more interestingly, the Dy analogue, compound **8**, shows SMM behaviour. This finding is in agreement with other Dy_4 planar systems developed previously in this group.^[88] Bearing in mind that such tetranuclear Ln cores are potential SMM candidates, the next step to this systematic study was to examine the influence of the co-ligand, therefore pivalic acid was replaced by benzoic acid. Four tetranuclear compounds $[\text{Ln}_4(\text{mdea})_2(\text{mdeaH})_2(\text{PhCO}_2)_6]$ (**12-15**) were synthesized. The tetranuclear cores found in **12-15** are non-planar, with dihedral angles between the two Ln_3 triangles of *ca.* 40° , in contrast to the planar cores in **7-11**. Magnetic studies carried out on these compounds revealed that compounds **12** and **13** exhibit slow relaxation of magnetisation and show SMM behaviour, whereas in compounds **14** and **15**, antiferromagnetic interactions are dominant.

In summary, in this chapter a Ln/mdeaH₂/coligand synthetic approach was developed. Depending on the radius of the lanthanide cation, dinuclear or tetranuclear units are formed. Especially in the tetranuclear series, varying the nature of the co-ligand can result in significant changes to the structure of the core, therefore allowing SMM properties to be tuned. It is noted that for such *4f* systems, hydroxo and alkoxo bridges can mediate weak but significant interactions, as was previously shown in this group for a Dy_3 triangle,^[39] suggesting that future synthetic efforts should attempt to incorporate such superexchange pathways. The results suggested that one of the main contributions lanthanides can make to magnetic behaviour in

molecular systems arises from the possibility of providing significant anisotropy, which is an especially desirable feature in the design of new single molecule magnets.



Scheme 2 The synthetic route from $\text{Ln}(\text{NO}_3)_3 \cdot 6\text{H}_2\text{O}$ to compounds **3-8**, **9-13** and **14-17**.

Chapter 4: Structure and magnetic properties of iron-lanthanide aggregates

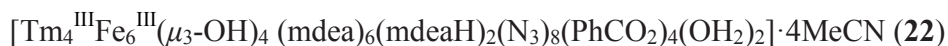
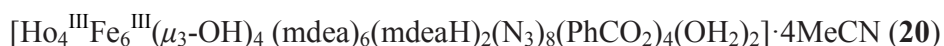
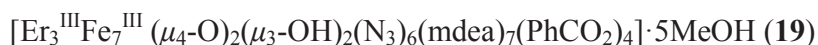
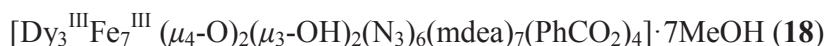
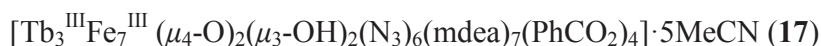
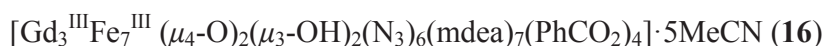
4.1 Introduction

The discovery of the first single molecule magnet (SMM)^[7,8] has animated interest in the field of magnetism, due to the fact that SMMs can be magnetised, below certain temperatures, with retention of their magnetisation after the magnetic field is switched off. The quest for new SMMs displaying high blocking temperatures has focussed the interests of many synthetic chemists towards the development of *3d-4f* heterometallic systems. Polynuclear clusters which combine high spin and/or single-ion anisotropy, such as Cu_6Dy_3 ,^[106a] Co_2Gd ^[106b] and Mn_5Dy_4 ^[106c] have reported a magnitude of the barrier to reorientation of the spin, Δ_{eff} , which reaches the value of 25, 28 and 38 K, respectively. From the synthetic point of view, *N*-substituted diethanolamine and related ligands represent useful tools in the synthesis of polynuclear clusters possessing SMM behaviour.^[105c,73,75,78] Sparked by the structural diversity and interesting properties of heterometallic *3d-4f* compounds, mixed *3d-4f* (Fe-Dy) compounds have been investigated as a means of enhancing anisotropy and/or spin state using *N*-methyldiethanolamine (mdeaH₂) as a ligand. Up to now, only two examples of Fe-Dy SMMs have been reported.^[70a,71] As discussed in Chapter 3, tetranuclear lanthanide compounds **12-15** consisting of benzoic acid as co-ligand were successfully synthesised and characterised. These reaction strategies were modified and a new reaction system involving *3d-4f* complexes was developed. The research presented within this chapter describes the development of new strategies for the synthesis of new Fe-Ln clusters which are valuable additions to the growing family of mixed *3d-4f* species, possessing unique cores and display interesting magnetic properties.

To facilitate the formation of polynuclear compounds, *N*-methyldiethanolamine was used as a ligand in the new reaction system. Since mdeaH₂ contains alcoholic arms, which are good metal-bridging groups on deprotonation, it fosters the formation of polynuclear products, as discussed in Chapter 1. In addition, since transition metal cations are readily chelated by diethanolamine ligands, while oxophilic lanthanide cations show a strong affinity towards hard donors such as the oxygen atoms of deprotonated alkoxy groups, this could lead to mixed *3d-4f* products.

4.2 Structure and magnetic properties of decanuclear complexes (16-22)

The reactions of $\text{Ln}(\text{NO}_3)_3 \cdot x\text{H}_2\text{O}$ ($\text{Ln} = \text{Gd, Tb, Dy, Ho, Er}$ and Tm) with mdeaH_2 , benzoic acid, FeCl_3 and NaN_3 in a ratio of (1:5:1:1:3) in acetonitrile yielded the decanuclear complexes $[\text{Ln}_3^{\text{III}}\text{Fe}_7^{\text{III}}(\mu_4\text{-O})_2(\mu_3\text{-OH})_2(\text{N}_3)_6(\text{mdea})_7(\text{PhCO}_2)_4]$ (**16-19**). The methanol solvates of the Dy(III) and Er(III) complexes could also be obtained by using $\text{DyCl}_3 \cdot x\text{H}_2\text{O}$ or $\text{ErCl}_3 \cdot x\text{H}_2\text{O}$ in methanol. A new class of decanuclear compounds $[\text{Ln}_4^{\text{III}}\text{Fe}_6^{\text{III}}(\mu_3\text{-OH})_4(\text{mdea})_6(\text{mdeaH})_2(\text{N}_3)_8(\text{PhCO}_2)_4(\text{OH}_2)_2]$ ($\text{Ln} = \text{Ho, Er, Tm}$) **20-22**, is synthesised using acetonitrile only as solvent. It is worth mentioning that change of solvent does not affect the overall the nuclearity of the isolated crystalline material but it does change the Ln:Fe ratio.



4.2.1 Structure of $[\text{Dy}_3^{\text{III}}\text{Fe}_7^{\text{III}}(\mu_4\text{-O})_2(\mu_3\text{-OH})_2(\text{N}_3)_6(\text{mdea})_7(\text{PhCO}_2)_4] \cdot 7\text{MeOH}$ (18)

X-Ray crystallographic structure determinations were carried out for all four compounds **16-19**. Crystals of these Fe_7Ln_3 compounds, whether obtained from MeOH or MeCN, are all isomorphous, crystallising in the triclinic space group P-1 with $Z = 2$. Within the structure, the molecular twofold axes are aligned almost exactly perpendicular to the 001 plane. In fact, the crystal structure as a whole has *quasi*-twofold symmetry in this direction, and in consequence all the crystals studied showed twinning by a 180° rotation about c^* . Because α is very close to 90° (typically $90.4\text{-}91.2^\circ$), the two reciprocal lattices are close to coincident, with very many overlapped reflections. Most crystals also show additional twinning, and accurate integration proved problematic, even with the Bruker software. One crystal of the methanol solvate of Fe_7Dy_3 , **18**, was found to be cleanly twinned, and this could be integrated successfully and the structure refined to an acceptable standard; this structure will be described in detail below. With the other datasets, it was generally only possible to refine the metal atoms anisotropically.

However, it is clear that the other Fe₇Ln₃ compounds are closely isostructural, and their unit cells are compared in Table 4.1.

The central core of **18** is built up from seven Fe^{III} cations each of which is chelated by a doubly-deprotonated (mdea)²⁻ ligand, and three Dy^{III} cations. While the molecule has no crystallographically-imposed symmetry, an idealised two-fold axis runs through N(1), Fe(1) and Dy(1). The structure of the molecule (organic H atoms omitted for clarity) is shown in Figure 4.1. Two views of the central core (benzoate and azide ligands omitted) are shown in Figures 4.2.

The two (μ₄-O)²⁻ ligands O(1) and O(2) each bridge between two Fe and two Dy centres, either Fe(2) and Dy(2) or Fe(3) and Dy(3), respectively, and Fe(1) and Dy(1). The resulting distorted tetrahedral {Fe₂Dy₂(μ₄-O)} units thus share one edge, Fe(1)⋯Dy(1). Within each tetrahedron, the Fe-O-Fe angles (144.1(4) and 143.5(4)°) are much larger than the Fe-O-Dy (99.1(3)-101.9(3)°) and Dy-O-Dy (106.1(2), 106.6(3)°) angles. The two Dy⋯Dy edges are each further bridged by a hydroxo ligand, which both form (μ₃-OH)⁻ bridges to a further Fe centre, with O(3) and O(4) bridging either Dy(1), Dy(2) and Fe(4), or Dy(2), Dy(3) and Fe(5), respectively. These hydroxo bridges are more regular than the oxo bridges; the angles around O(3) and O(4) are all in the range 103.0(3)-111.5(3)°. The final two triple-bridges are provided by alkoxo oxygens from two (mdea)²⁻ ligands: O(13) bridges Fe(5), Dy(3) and Fe(7), while O(11) bridges Fe(4), Dy(2) and Fe(6). The angles around O(11) and O(13) are rather smaller (95.4(3)-101.6(3)°) than those for the (μ₃-OH)⁻ bridges. The remaining twelve (mdea)²⁻ oxygens each form a (μ-OR) bridge between the iron which their respective ligand chelates and one other metal centre, forming ten Fe⋯Dy and two Fe⋯Fe bridges. The twelve Fe-O-Dy or Fe-O-Fe angles are rather consistent, with all in the range 101.7(3)-109.9(3)°. The four benzoate ligands form *syn,syn* bridges, each between an iron and a dysprosium centre.

The coordination sphere of each iron except Fe(1) is completed by a terminal azido ligand, resulting in a more or less distorted *cis*-N₂O₄ octahedral environment. Fe(1) has a five-coordinate NO₄ environment, in which the two alkoxo oxygens O(5) and O(6) occupy the axial sites of what is best described as a trigonal bipyramidal geometry. The Fe-O, Fe-N(azide) and Fe-N(imino) distances are in the ranges 1.880(7)-2.143(7) Å, 1.971(9)- 2.080(9) Å and 2.199(10)-2.240(10) Å, respectively. The three Dy centres are each eight-coordinate, with approximate square-antiprismatic geometries, and Dy-O bond lengths in the range 2.258(8)-2.532(7) Å.

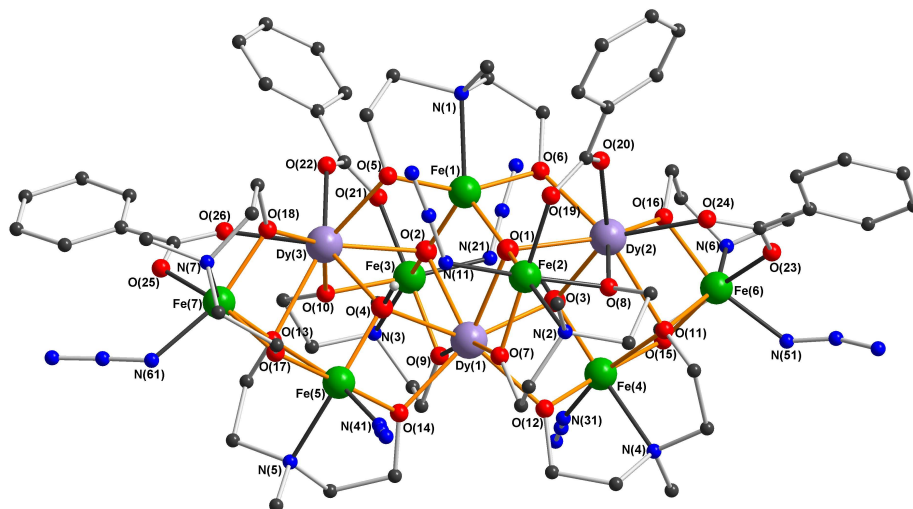


Fig. 4.1 Structure of $[\text{Dy}_3^{\text{III}}\text{Fe}_7^{\text{III}}(\mu_4\text{-O})_2(\mu_3\text{-OH})_2(\text{N}_3)_6(\text{mdea})_7(\text{PhCO}_2)_4]$ in **18**. Hydrogen atoms are omitted for clarity. Grey, red, blue, green and lavender spheres represent C, O, N, Fe and Dy, respectively.

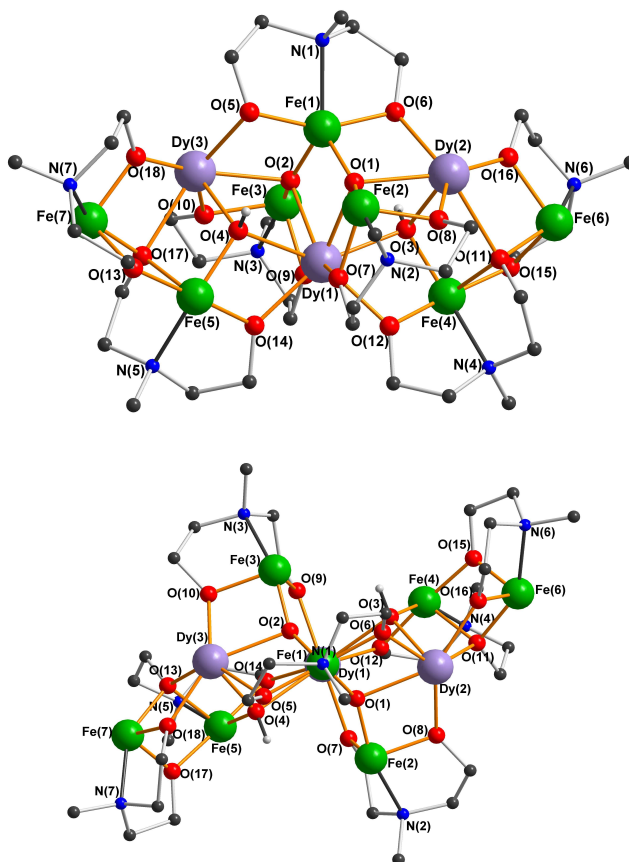


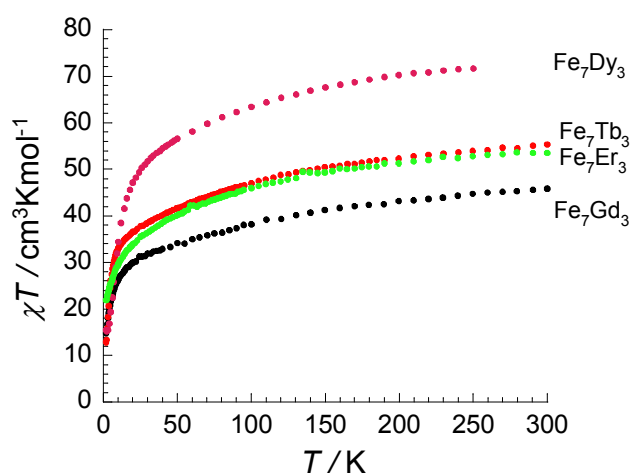
Fig. 4.2 Structure of the $[\text{Dy}_3^{\text{III}}\text{Fe}_7^{\text{II}}(\mu_4\text{-O})_2(\mu_3\text{-OH})_2]^{24+}$ core in the cluster of **18**.

Table 4.1 Unit cell measurements of compound **16-19**.

	<i>a</i>	<i>b</i>	<i>c</i>	α	β	γ	<i>V</i>
(16) Fe ₇ Gd ₃ (MeCN)	14.3513(14)	17.0941(16)	21.1210(19)	90.891(2)	93.705(2)	97.509(2)	5124.8(8)
(16a) Fe ₇ Gd ₃ (MeOH)	14.444(2)	17.383(3)	21.268(3)	91.229(3)	93.576(3)	98.440(3)	5269(2)
(17) Fe ₇ Tb ₃ (MeCN)	14.366(2)	17.178(2)	21.209(3)	90.572(3)	93.727(3)	97.761(3)	5173.7(13)
(18) Fe ₇ Dy ₃ (MeOH)	14.2482(17)	17.446(2)	21.224(2)	90.430(2)	92.445(2)	98.504(2)	5212.4(11)
(19) Fe ₇ Er ₃ (MeOH)	14.182(3)	17.133(3)	21.078(4)	91.204(3)	92.860(3)	97.969(3)	5063.7(16)

4.2.2 Magnetic properties of [Ln₃^{III}Fe₇^{III}(μ_4 -O)₂(μ_3 -OH)₂(N₃)₆(mdea)₇(PhCO₂)₄] (Ln = Gd, Tb, Dy, Er) (compounds 16-19)

Due to the high anisotropy of compound **18**, this compound was dispersed in Apiezon grease during the magnetic measurements. Thus the dc susceptibility of **18** was only measured below 250 K. The temperature dependence of the magnetic susceptibilities of all compounds **16-19** show similar thermal evolution in the range of 1.8-300 K (Fig. 4.3). The magnetic data are summarized in Table 4.2. The χT product values at room temperature are in low comparison to the expected value for seven Fe(III) ions ($S = 5/2$, $g = 2$, $C = 4.375 \text{ cm}^3 \text{ K mol}^{-1}$) and three Ln(III) ions.

**Fig. 4.3** Temperature dependence of the χT products for compounds **16–19** at 1000 Oe.

On decreasing the temperature, the χT product at 1000 Oe continuously decreases to reach a minimum value at 1.8 K. As Gd(III) is an isotropic ion without orbital contributions, the interactions among the spin carriers in **16** are antiferromagnetic. However, in the case of compounds **16**, **17** and **19**, the thermal decrease of the χT product might also originate, at least partially, from the depopulation of the Stark sublevels of the anisotropic Tb, Dy and Er ions.^[90] Therefore, the decrease of the χT products might also be responsible for the thermal decrease of the χT product.

The field dependence of the magnetisation of compounds **16-19** at low temperatures show that the magnetisation smoothly increases with the applied dc field. In all cases there is no clear saturation, even at 7 T at which it reaches the values given in Table 4.2, suggesting the presence of magnetic anisotropy and/or the population of low-lying excited states. Moreover, while plotting the M versus H/T at low temperatures for compounds **16-19** in Figures 4.4, 4.5, 4.6a and 4.8(right). The curves are not superimposed on a single master curve further indicating the presence of magnetic anisotropy and/or low-lying excited states.

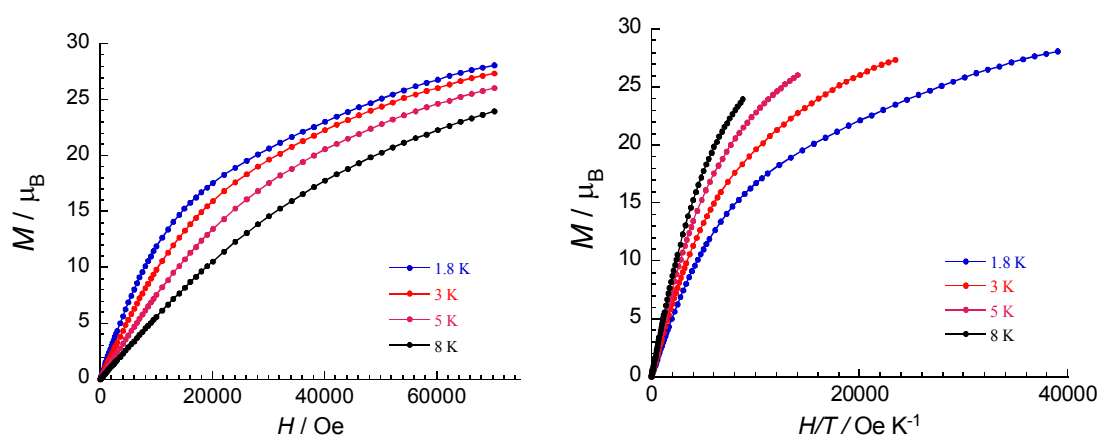


Fig. 4.4 Field dependence of magnetisation at indicated temperatures for compound **16**.

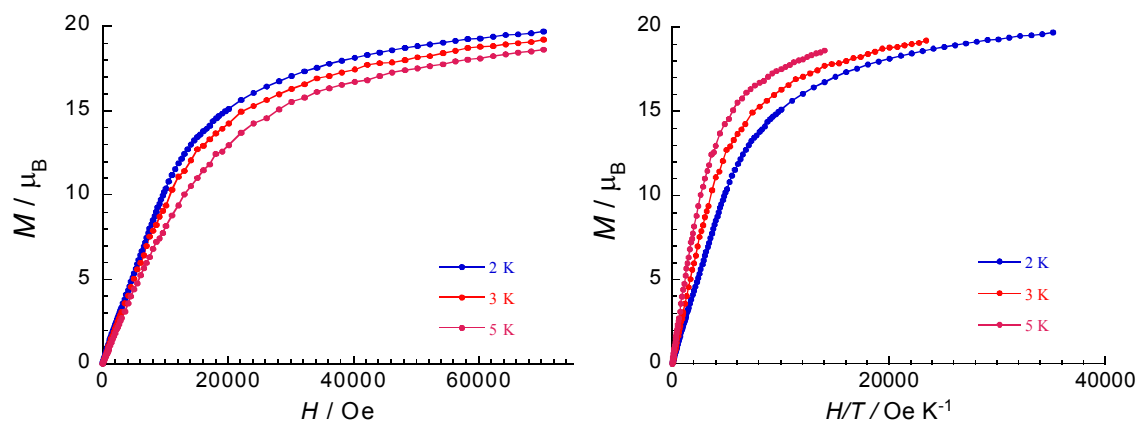


Fig. 4.5 Field dependence of magnetisation at indicated temperatures for compound **17**.

Table 4.2 Comparison of dc magnetic data for compounds **16-19**.

Compound	16 (Gd)	17 (Tb)	18 (Dy)	19 (Er)
Ground state term of Ln ion	$^8S_{7/2}$	7F_6	$^6H_{15/2}$	$^4I_{15/2}$
S	7/2	2	5/2	3/2
L	0	3	5	6
g	2	3/2	4/3	6/5
C ($\text{cm}^3\text{Kmol}^{-1}$) for each Ln ion ^[98]	7.87	11.82	14.17	11.5
χT ($\text{cm}^3\text{Kmol}^{-1}$) expected value for Ln_3Fe_7 at RT	54.25	66.08	73.13	65.12
χT ($\text{cm}^3\text{Kmol}^{-1}$) experimental value for Ln_3Fe_7 at RT	45.8	55.4	71.6	53.3
χT ($\text{cm}^3\text{Kmol}^{-1}$) experimental value for Ln_3Fe_7 at 1.8 K	14.8	12.8	15.4	21.9
magnetisation (μ_B) observed at 7T and 1.8 K or 2 K	28.1	19.6	30.1	22.5

For compound **18**, the magnetisation at low field is increasing rapidly in agreement with a non-zero ground state for complex **18**, (Fig. 4.6) and it reaches a pseudo-saturation at about $8 \mu_B$ around 1 T. Then a second step is observed, as is clearly seen in the plot of dM/dH versus H (Fig. 4.7) which displays a maximum (*i.e.* a characteristic field that corresponds to an inflexion point on the M versus H plot) at 16300 Oe. This behaviour is typically seen when the magnetic field overcomes antiferromagnetic interactions and the spins align with the applied field. In other words, low lying excited states are progressively populated with the increase of external field. As the spin ground state is difficult to determine in dysprosium-based compounds, it is also difficult to evaluate the magnitude of the magnetic interactions and the spins involved in the feature observed at 16300 Oe. It is worth mentioning that the M versus H data reveal the existence of

hysteresis (*i.e.* slow relaxation of the magnetisation) at 1.8 K with a very small coercive field (few Oe).

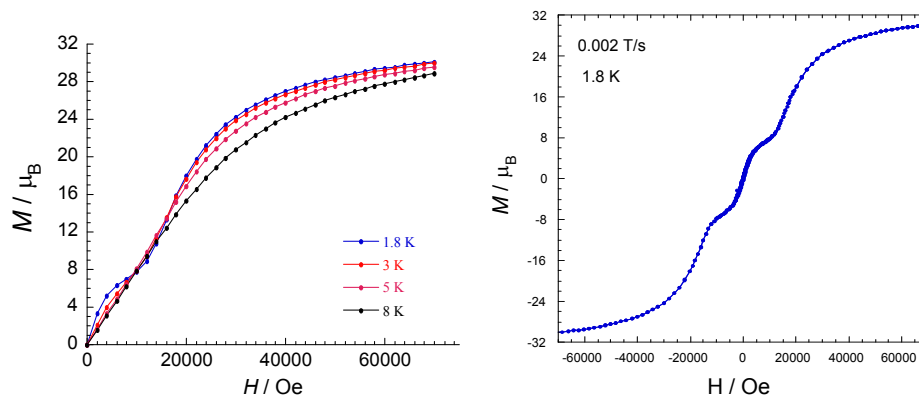


Fig. 4.6 (a) Field dependence of magnetisation at indicated temperatures for compound **18** (left). (b) Hysteresis measurements of compound **18** at 1.8 K with a sweeping rate of 0.002 T/s. (right).

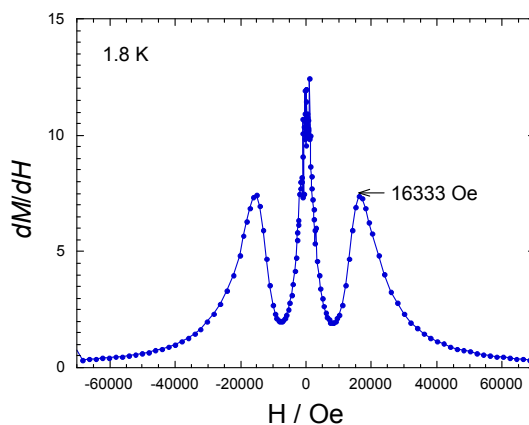


Fig. 4.7 Plot of dM/dH versus H for compound **18**.

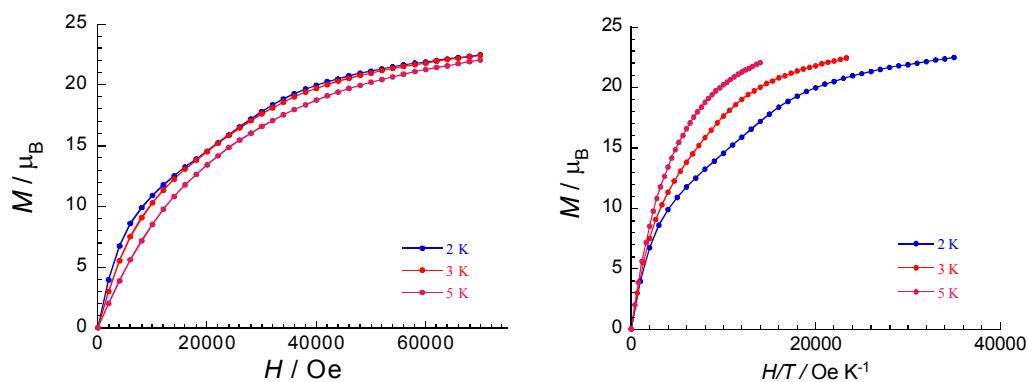


Fig. 4.8 Field dependence of magnetisation at indicated temperatures for compound **19**.

In the case of the Er(III) analogue **19**, there is a relatively rapid increase of the magnetisation below 1 T to reach a magnitude of $14.8 \mu_B$ and a slope centred on ~ 2.8 T (Fig. 4.9) and then a smooth increase above 3 T without saturation. The shape of the magnetisation curves suggest that low-lying excited states are progressively populated with the increase of the external field.

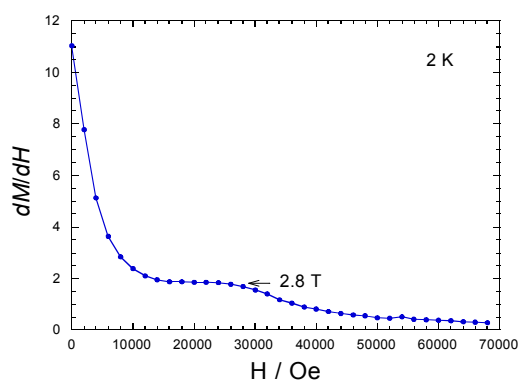


Fig. 4.9 Plot of dM/dH versus H for compound **19**.

Due to the presence of anisotropy in those compounds (Fig. 4.4-4.8), the ac susceptibility measurements were carried out in zero dc field. There is no out-of-phase signal shown above 1.8 K for compounds **16** and **19**, while an out-of-phase component was present in both compounds **17** and **18**.

In the Tb case (**17**), an out-of-phase signal is detected (about 15% of the in-phase signal) clearly below 3 K indicating slow relaxation of the magnetisation (Fig. 4.10). Both in-phase and out-of-phase signals are frequency dependent, suggesting that this compound exhibits slow relaxation and is a SMM. In addition, the ac susceptibility measurements under a small dc field were also performed in order to see whether relaxation would slow down (Fig. 4.11). The relaxation mode is almost unchanged indicating that the slow relaxation is fixed under a small dc field. This observation shows that if this compound is a SMM, it does not have a relaxation influenced by quantum effects at 1.8 K and above.

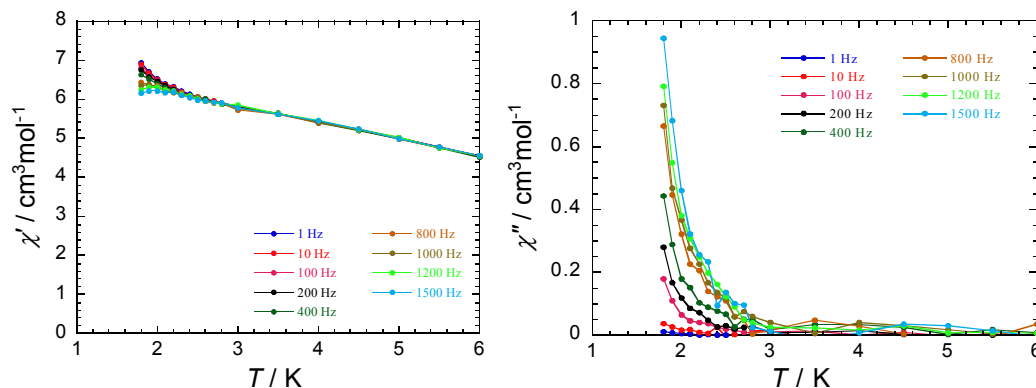


Fig. 4.10 Temperature dependence of the in-phase (left) and out-of-phase (right) components of the ac magnetic susceptibility for **17** under zero dc field.

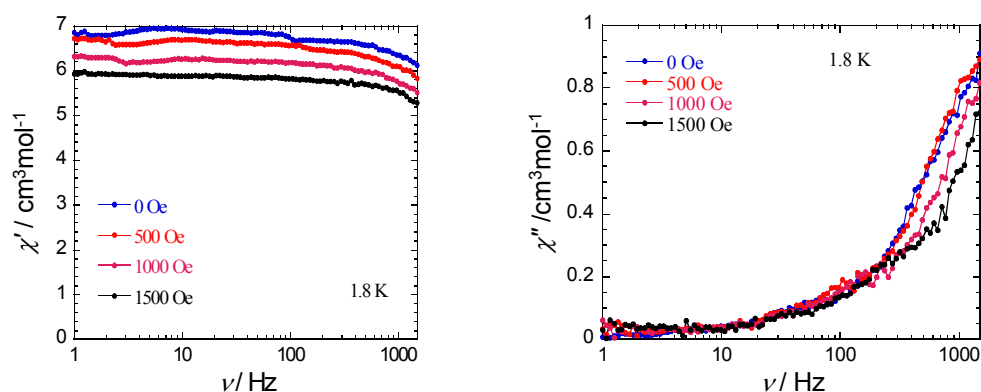


Fig. 4.11 Frequency dependence at 1.8 K of the in-phase (left) and the out-of-phase (right) ac susceptibility component at different dc fields for **17**.

The magnetic relaxation of **18** has been probed using ac susceptibility measurements as a function of the temperature at different frequencies and also at different temperatures as a function of the frequency. Clearly this compound exhibits slow relaxation of its magnetisation. In zero-dc field (Fig. 4.12,4.13), a strong frequency dependent in-phase and out-of-phase signal are observed below 7 K indicating slow relaxation of the magnetisation. The maximum of the out-of-phase signal was observed at 4.4 K at a frequency of 1500 Hz. This feature (shape and frequency dependence) strongly suggests that this compound might be a SMM. After extracting the characteristic relaxation time (τ) of the system from both data sets, τ was found to follow an Arrhenius law with the characteristic SMM energy gap, Δ , estimated at 30.9 K and the pre-exponential factor (slow relaxation time), τ_0 at $1.3 \cdot 10^{-7}$ s (Fig. 4.14).

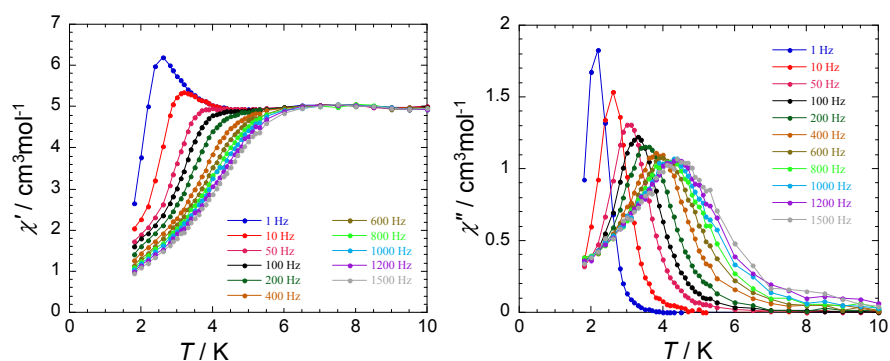


Fig. 4.12 Temperature dependence of the in-phase (left) and out-of-phase (right) component of the ac magnetic susceptibility for **18** under zero dc field.

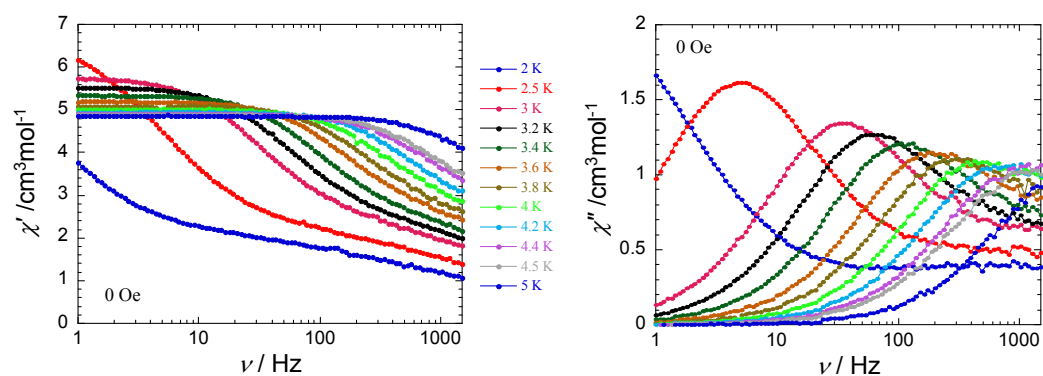


Fig. 4.13 Frequency dependence of the in-phase (left) and out-of-phase (right) ac susceptibility component at different temperatures for **18** under zero dc field.

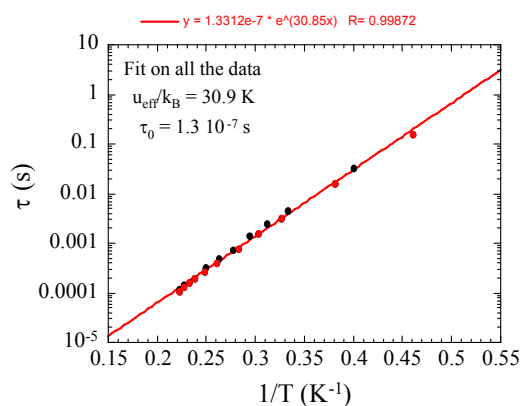


Fig. 4.14 τ versus $1/T$ plot for **18** obtained from both temperature- and frequency-dependent ac susceptibility measurements under zero dc field.

A small dc field was applied to see whether relaxation would slow down due to the possible presence of a quantum relaxation pathway. The relaxation mode is indeed almost unchanged (*i.e.* the slow relaxation is fixed) under a small dc field (Fig. 4.15). This observation shows that the relaxation mechanism of this SMM, at least above 1.8 K, is not influenced by quantum effects.

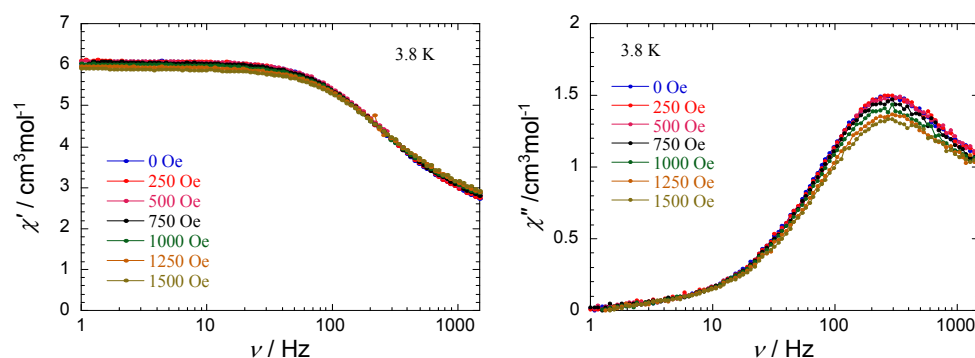


Fig. 4.15 Frequency dependence of the in-phase (left) and the out-of-phase (right) ac susceptibility components at 3.8 K at different dc fields for **18**.

Micro-SQUID measurements were done on single crystal oriented in the easy magnetic direction. These data confirm the presence of slow relaxation of the magnetization, as hysteresis is clearly seen below 2 K at 0.035 T/s (Fig. 4.16). The coercive field is strongly temperature dependent, increasing with decreasing temperature and increasing with increasing field sweep rate as expected for the superparamagnetic-like behavior observed for SMM systems. Below 0.5 K, the width of the hysteresis loop becomes temperature-independent (about 2 T at 0.035 T/s) indicating the presence of a quantum regime where the relaxation of the magnetization occurs by quantum tunneling. It is worth mentioning that steps are also visible on the M versus H data that are probably the signature of resonant quantum tunneling relaxation often found for SMM complexes. In order to obtain a more quantitative assessment of the magnetization relaxation dynamics, the time-dependence of the dc magnetization decay was studied (Fig. 4.17). The resulting dc relaxation rate together with the ac data were used to construct an Arrhenius plot (Fig. 4.18) leading to an effective energy barrier U_{eff} of 33.4 K and relaxation time τ of 6.6×10^{-8} s.

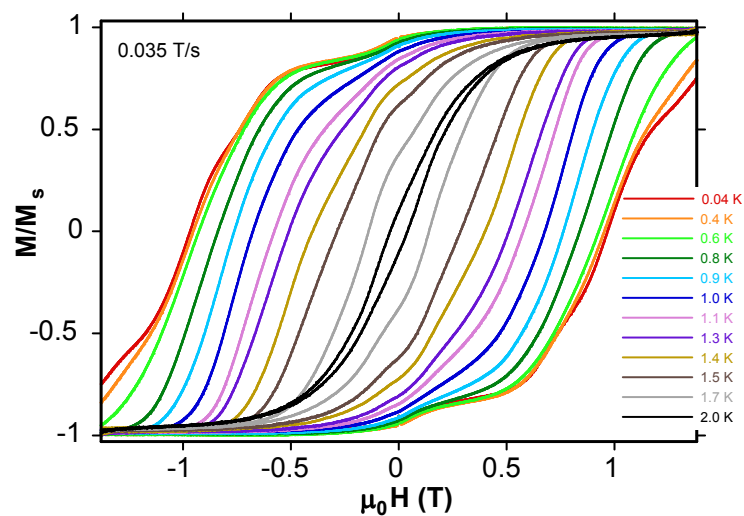


Fig. 4.16 Magnetization (M) versus applied dc field (H) hysteresis loops for single crystals of **18** at the indicated temperatures and a fixed sweep rate of 0.035 T/s. The magnetization is normalized to its saturation value M_s .

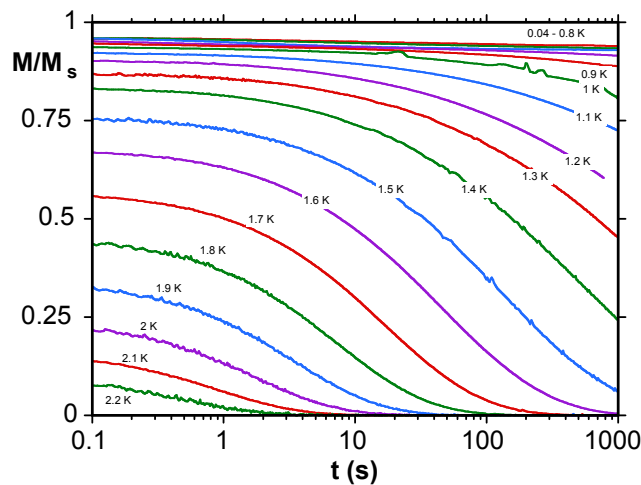


Figure 4.17. Magnetization (M) vs time decay plots in zero dc field for a single crystal of **18**. The magnetization is normalized to its saturation value M_s .

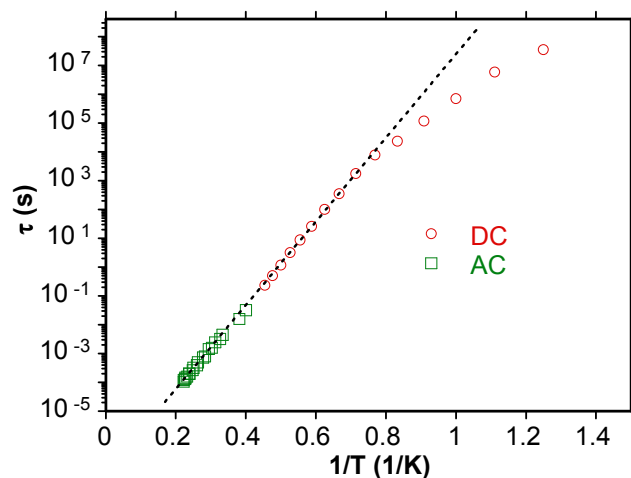


Figure 4.18. Arrhenius plot of the relaxation time (τ) versus $1/T$ for a single crystal of **18** using data obtained from ac susceptibility and the dc magnetization decay measurements of Fig. 4.17. The dashed line is the fit of data in the thermally activated region to the Arrhenius equation; see the text for the fit parameters.

4.2.3 Structure of $[\text{Tm}_4^{\text{III}}\text{Fe}_6^{\text{III}}(\mu_3\text{-OH})_4(\text{mdea})_6(\text{mdeaH})_2(\text{N}_3)_8(\text{PhCO}_2)_4(\text{OH}_2)_2]\cdot 4\text{MeCN}$ (**22**)

The Fe_6Ln_4 aggregates **20-22** crystallise in the orthorhombic space group $Pca2_1$, with $Z = 4$. The molecular structure as a whole has no crystallographic symmetry, but possesses idealised C_2 symmetry. The structure of the Fe_6Tm_4 compound **22** will be discussed in detail. The structures of the analogous Fe_6Ho_4 and Fe_6Er_4 complexes could only be refined with the metal atoms anisotropic. It is possible that in fact their true crystal symmetry is slightly lower than orthorhombic, resulting in unresolved *pseudo*-merohedral twinning. However, attempts to refine the structures in monoclinic space groups as twins proved unsuccessful because of high correlation between metal atom parameters. Nonetheless, the three compounds are closely isostructural, and at least *quasi*-isomorphous, as can be seen from comparison of the unit cells (Table 4.3).

The crystal structure of **22** contains a decanuclear $[\text{Tm}_4\text{Fe}_6(\mu_3\text{-OH})_4(\text{mdea})_6(\text{mdeaH})_2(\text{N}_3)_8(\text{PhCO}_2)_4(\text{H}_2\text{O})_2]$ moiety (Fig. 4.19) and solvating MeCN molecules; the latter will not be further discussed. The structural core is shown in Fig. 4.20. Four of the Fe centres, Fe(1) – Fe(4), are chelated by doubly-deprotonated $(\text{mdea})^{2-}$ ligands, of which the oxygens each form a bridge to a Tm centre. Fe(5) and Fe(6) are each chelated by a mono-deprotonated $(\text{mdeaH})^-$ ligand, of which the deprotonated oxygens bridge to Tm centres while the

protonated –OH oxygens coordinate to their respective Fe centres without bridging. Tm(3) and Tm(4) are also chelated by (mdea)²⁻ ligands, which each bridge to a Tm and an Fe, in contrast to the Fe₇Ln₃ structures, in which the diethanolamine ligands only chelated Fe centres. Fe(1), Fe(2), Tm(1) and Tm(2) together form a central “butterfly” moiety, in which the (μ₃-OH)⁻ ligands O(1) and O(2) each bridge a FeTm₂ triangle. Each of the four Fe··Tm edges is also bridged by an alkoxo oxygen from one of the (mdea)²⁻ ligands chelating Fe(1) or Fe(2). Two opposite Fe··Tm edges are also bridged by *syn, syn*-(μ-benzoate) ligands. Each of Tm(1) and Tm(2) is also linked by a (μ₃-OH)⁻ ligand, O(3) or O(4), respectively, to further Fe and Tm centres.

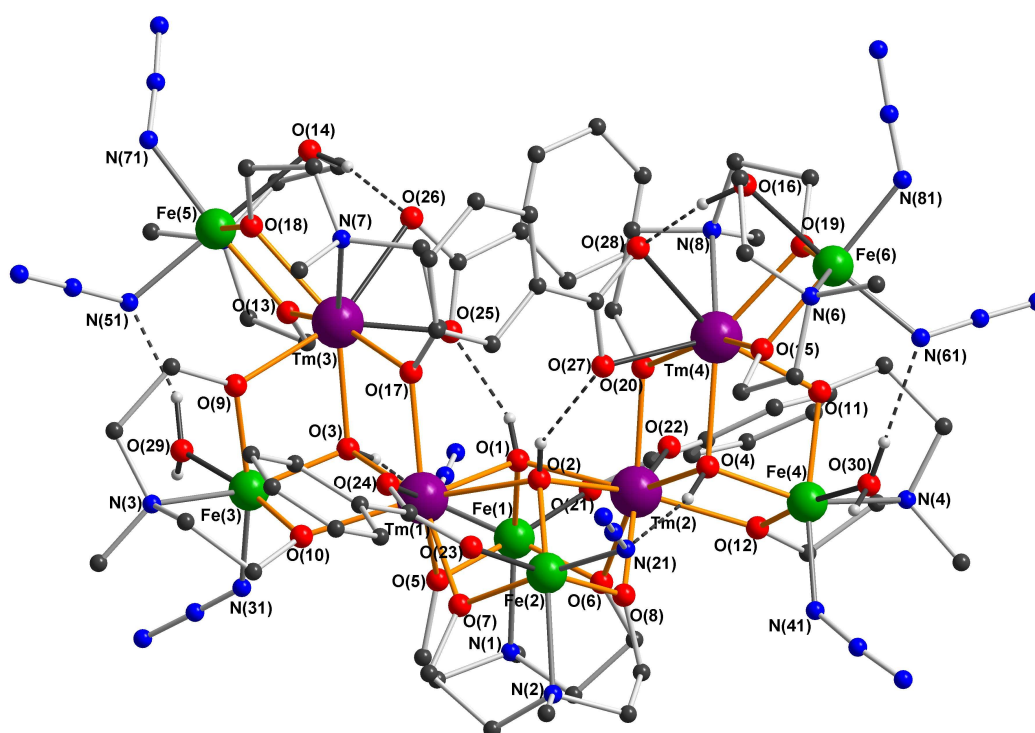


Fig. 4.19 Molecular structure of [Fe₆^{III}Tm₄^{III}(μ₃-OH)₄(mdea)₆(mdeaH)₂(μ-benzoate)₄(N₃)₈(OH₂)₂]. Organic H atoms and minor disorder components omitted for clarity; intramolecular hydrogen-bonds are shown as dotted lines.

The edges of these Tm₂Fe triangles are each bridged by a deprotonated akoxo oxygen. The two “outer” Thuliums, Tm(3) and Tm(4), are then linked by a pair of alkoxo bridges to Fe(5) and Fe(6), respectively, completing the core structure. The core can also be thought of as a chain of four thuliums, to which the irons are attached by (μ₃-OH)⁻ and alkoxo bridges. Since the Tm··Tm distances are all similar (3.751-3.867 Å), the two Tm··Tm··Tm angles are 108.6 and 109.0°, and

the Tm(3)-Tm(1)-Tm(2)-Tm(4) torsional angle is 67.5° , the geometry of the Tm₄ chain could be considered as resembling that of the *gauche* conformation of the butane molecule. The octahedral coordination environments of the Fe centres are completed by one azide ligand (Fe(1) and Fe(2)), an azide and an aquo ligand (Fe(3) and Fe(4)) or two azides (Fe(5) and Fe(6)). The octacoordination of Tm(3) and Tm(4) is each completed by a chelating benzoate ligand, giving a geometry intermediate between square-antiprismatic and dodecahedral, while the geometries about Tm(1) and Tm(2) approximate more closely to square-antiprismatic. In contrast to the Fe₇Ln₃ structures, the molecular structures of the Fe₆Ln₄ species are supported by several hydrogen bonds, involving the (μ_3 -OH)⁻ and aquo ligands, and the two protonated (mdeaH)⁺ oxygens.

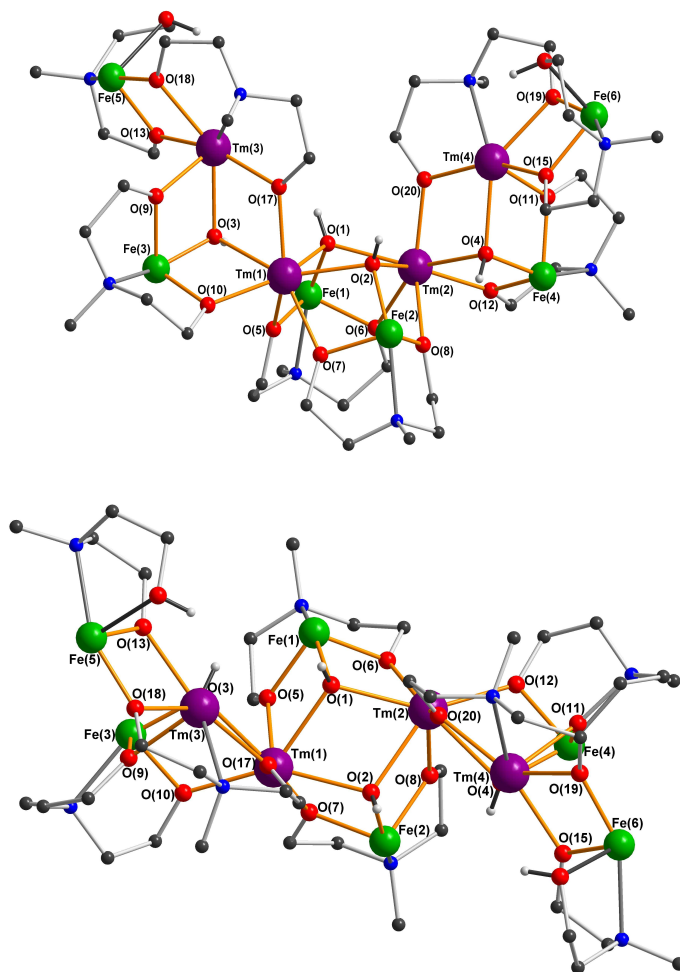


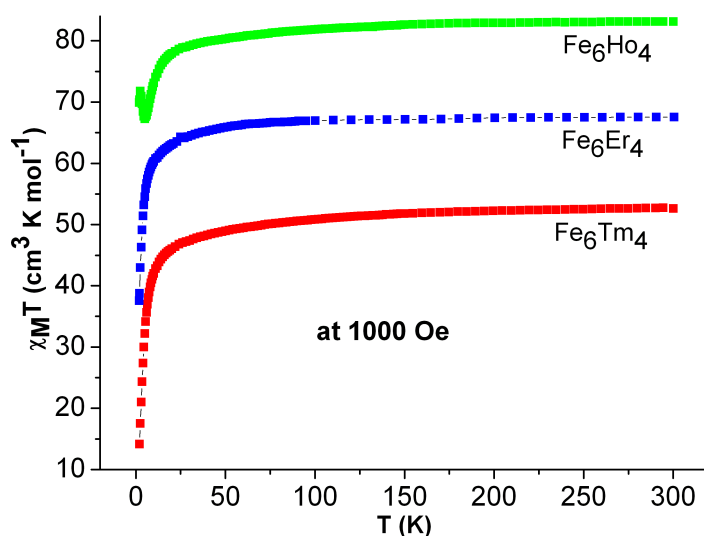
Fig. 4.20 Two views of the structure of the core of $[\text{Fe}_6^{\text{III}}\text{Tm}_4^{\text{III}}(\mu_3\text{-OH})_4(\text{mdea})_6(\text{mdeaH})_2(\mu\text{-benzoate})_4(\text{N}_3)_8(\text{OH}_2)_2]$. Azide and benzoate ligands, and C-H hydrogen atoms, omitted for clarity.

Table 4.3 Unit cell measurements of compound **20-22**.

	<i>a</i>	<i>b</i>	<i>c</i>	<i>V</i>
(20)Fe ₆ Ho ₄	30.3556(15)	21.2322(19)	17.3104(9)	11151.0(10)
(21)Fe ₆ Er ₄	30.333(2)	21.2834(12)	17.2716(12)	11150.3(15)
(22)Fe ₆ Tm ₄	30.2863(11)	21.2097(8)	17.1584(6)	11021.9(7)

4.2.4 Magnetic properties of [Ln^{III}Fe₆^{III}(μ₃OH)₄(mdea)₆(mdeaH)₂(N₃)₈(PhCO₂)₄(H₂O)₂]·4MeCN (Ln = Er, Ho, Tm) (**20-22**)

The temperature dependences of the magnetic susceptibilities of compounds **20-22** were measured on powder samples of compounds in the temperature range 1.8-300 K under an applied dc magnetic field of 1000 Oe (Fig. 4.21).

**Fig. 4.21** Temperature dependence of the χT product at indicated applied magnetic fields for **20-22**.

At room temperature the experimental χT values are in good agreement with the expected theoretical values of six uncoupled Fe(III) and four Ln(III) values for the compounds given in Table 4.4. On decreasing the temperature, the χT product at 1 T continuously decreases from room temperature till 1.8 K. The Stark sublevels of the anisotropic Ln (Ho, Er, and Tm) ions are thermally depopulated when the temperature is lowered resulting in a decrease of the χT versus T plot.^[90,102] However, the zero-field splitting (ZFS) of the Fe(III) ions might also be responsible

for the thermal decrease of the χT product. Since the magnetically active electrons of Ln(III) ions are deeply buried because of the shielding of the filled $5s$ and $5p$ orbitals, the magnetic exchange between the Ln(III) ions and Fe(III) is very weak.^[12]

The nature of magnetic exchange between the Ln(III) ions or between Ln(III) and Fe(III) ions is difficult to conclude due to the sudden decrease of the χT value which is mostly dominated by the depopulation of Stark levels at low temperature. The shape of the χT versus T curve of **20** at 1000 Oe, (Fig. 4.21) looks similar to that of ferrimagnetic materials. When the applied field is not too high (1000 Oe), a local minimum and maximum are observed at low temperature in the χT versus T plot. At higher field (10000 Oe), the stronger Zeeman perturbation simply leads to a rapid decrease in χT . For all the three complexes, χT plot decreases to lower value at low temperature except **20** for which χT starts rising from minimum value of $67.30 \text{ cm}^3 \text{ K mol}^{-1}$ at 4.90 K to the maximum value of $71.82 \text{ cm}^3 \text{ K mol}^{-1}$ at 2.5 K and finally falls to $69.94 \text{ cm}^3 \text{ K mol}^{-1}$ at 1.8 K.

The low-temperature field dependence of the magnetisation was studied at different temperatures. In all the cases magnetisation values of compounds **20**, **21** and **22** (Fig. 4.22, 4.23 and 4.24) smoothly increase to the corresponding values given in Table 4.4. The magnetisation does not saturate, which is common for Ln(III) ions due their orbital contribution. This lack of saturation suggests the presence of magnetic anisotropy and/or the population of low-lying excited states.^[90] For complex **20**, the magnetisation value at 2 K rapidly increases to $16 \mu_B$ at 0.4 T and then slows down in the range of 0.8 T to 1.4 T. After that, it again smoothly increases with increasing dc field (Fig. 4.22, inset).

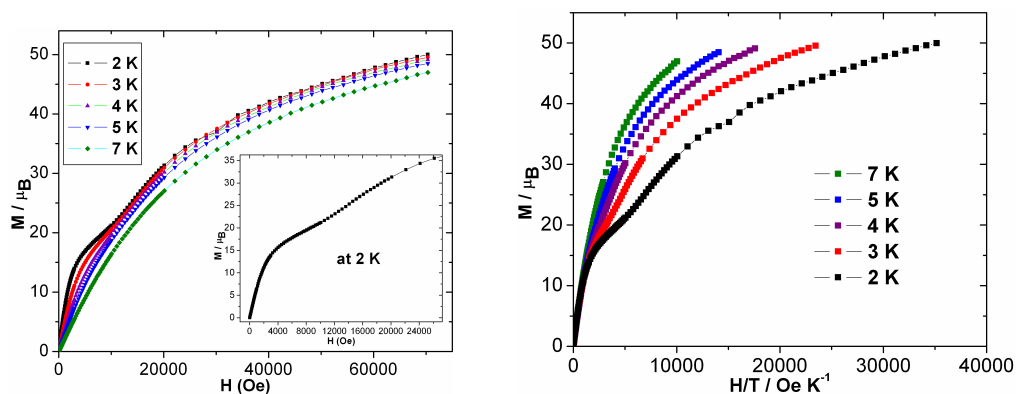


Fig. 4.22. Field dependence of magnetisation at indicated temperatures for **20**.

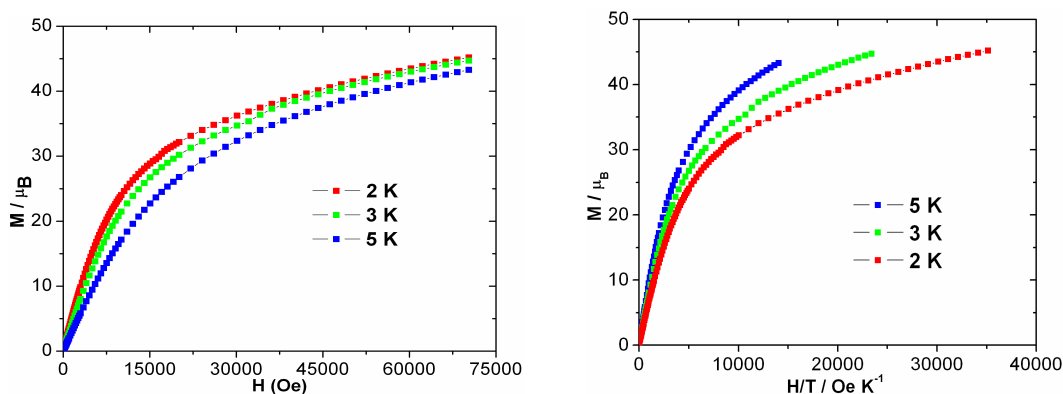


Fig. 4.23. Field dependence of magnetisation at indicated temperatures for compound **21**.

The step-like feature slowly vanishes at higher temperatures. This step-like behaviour is most probably because of field-induced spin population of the next low-lying excited states.^[12] Moreover, the M in $N\mu_B$ versus H/T plots at low temperatures (Fig. 4.22, 4.23 and 4.24, right) of **20**, **21** and **22** are not at all superimposed on a single master-curve, further indicating the presence of magnetic anisotropy and/or low-lying excited states.^[90,93]

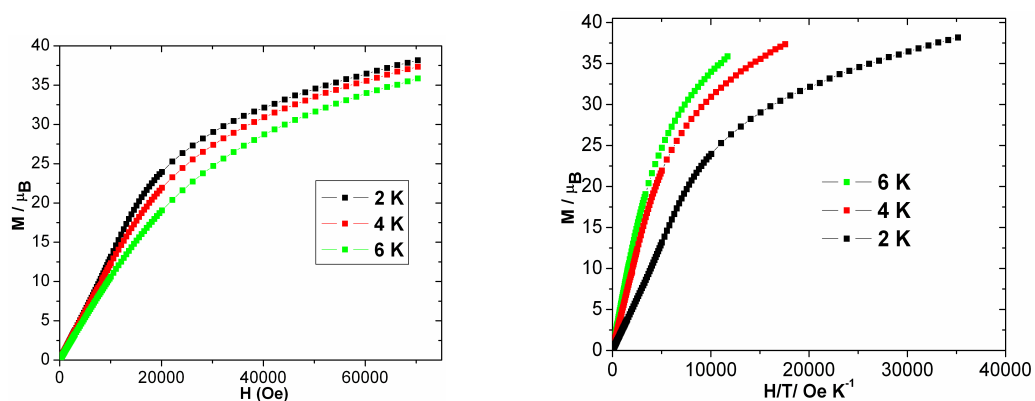


Fig. 4.24. Field dependence of magnetisation at indicated temperatures for **22**.

The frequency dependences of the ac susceptibilities were measured for all the three complexes (**20**, **21** and **22**). Only complex **20** shows slow magnetic relaxation below 3 K in the frequency range of 0.5-1500 Hz. On increasing frequency, the out-of-phase susceptibility increases to higher values without going through any sort of maxima while the in-phase susceptibility increases very slowly with decreasing ac frequency (Fig. 4.25), indicating that the compound could be a SMM.

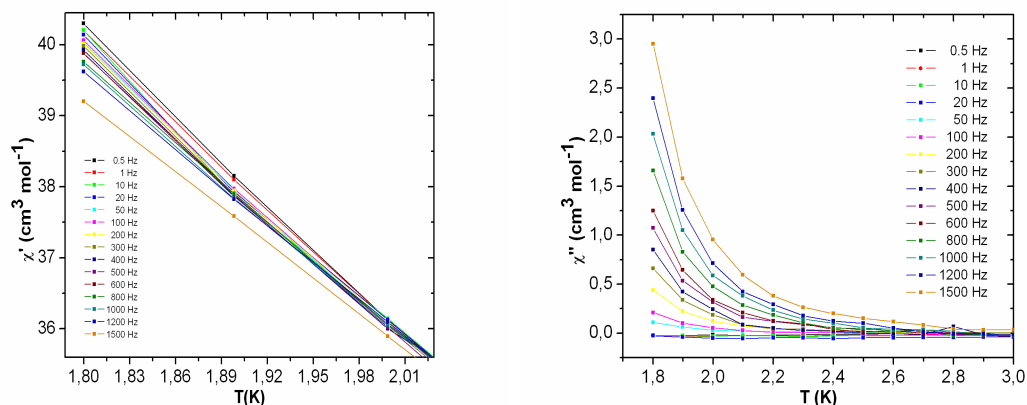


Fig. 4.25. Temperature dependence of the in-phase (left) and out-of-phase (right) components of the ac magnetic susceptibility, for **20** under zero dc field.

Table 4.4 Comparison of the magnetic data for compounds **20-22**.

Compound	20 (Ho)	21 (Er)	22 (Tm)
Ground state term of Ln ion	$^4I_{15/2}$	5I_8	3H_6
S	3/2	2	1
L	6	6	5
g	6/5	5/4	7/6
C ($\text{cm}^3\text{Kmol}^{-1}$) for each Ln ion ^[98]	14.07	11.5	7.15
χT ($\text{cm}^3\text{Kmol}^{-1}$) expected value for Ln_4Fe_6 at RT	82.45	72.13	54.77
χT ($\text{cm}^3\text{Kmol}^{-1}$) experimental value for Ln_4Fe_6 at RT	83.31	67.62	52.77
χT ($\text{cm}^3\text{Kmol}^{-1}$) experimental value for Ln_4Fe_6 (1T) at 1.8 K	17.82	24.63	12.70
magnetisation (μ_B) observed at 7 T and 2 K	45.30	49.98	38.20

4.3 Structure and magnetic properties $[\text{Er}^{\text{III}}\text{Fe}_4^{\text{III}}(\mu_3\text{-O})(\text{mdea})_3(\text{mdeaH})(\text{O}_2\text{CPh})_2(\text{N}_3)_4] \cdot 2.5 \cdot \text{MeCN}$ (**23**)

A pentanuclear compound $[\text{ErFe}_4^{\text{III}}(\mu_3\text{-O})(\text{mdea})_3(\text{mdeaH})(\text{O}_2\text{CPh})_2(\text{N}_3)_4]$ was obtained by using *N*-methyldiethanolamine ligand, $\text{ErCl}_3 \cdot x\text{H}_2\text{O}$, benzoic acid, FeCl_3 and NaN_3 in a ratio of (1:1:1:2:2) in acetonitrile.

4.3.1 Structure of $[\text{Er}^{\text{III}}\text{Fe}_4^{\text{III}}(\mu_4\text{-O})(\text{mdea})_3(\text{mdeaH})(\text{O}_2\text{CPh})_2(\text{N}_3)_4] \cdot 2.5\text{MeCN}$ (**23**)

Complex **23** crystallises in the monoclinic space group $P2_1$ with $Z = 4$; there are therefore two independent (but nonetheless closely isostructural) molecules in the asymmetric unit. One

molecule of the pentanuclear compound $[\text{Er}^{\text{III}}\text{Fe}_4^{\text{III}}(\mu_3\text{-O})(\text{mdea})_3(\text{mdeaH})(\text{O}_2\text{CPh})_2(\text{N}_3)_4]$ is depicted in Fig. 4.26. The structure contains a $[\text{Er}^{\text{III}}\text{Fe}_4^{\text{III}}]^{11+}$ core (Fig.4.27) and charge consideration requires four deprotonated *N*-methyldiethanolamine ligands, two benzoate ligands and four azide ligands. Er(1), Fe(1), Fe(2) and Fe(3) are bridged by one $(\mu_4\text{-O})^{2-}$ ligand, O(1), while a μ_3 -alkoxo oxygen atom O(5) bridges Er(1), Fe(3) and Fe(4). Peripheral ligation is provided by two benzoate and four *mdea*²⁻ ligands. One benzoate group bridges Fe(1) and Fe(2) and the second bridges Er(1) and Fe(2) in a *syn-syn* binding modes. The three (*mdea*)²⁻ ions each chelate Fe(III) centres, Fe(1), Fe(3) and Fe(4), with their deprotonated O atoms forming either triple- (O(5)) or double-bridges. The (*mdeaH*)⁻ ligand chelates Er(1), with its deprotonated oxygen bridging to Fe(2) but its protonated –OH coordinating to Er(1) without bridging. One azide ligand coordinates in a terminal fashion to each of the Fe(III) ions, completing their coordination spheres. The coordination number around Er(1) is eight, with a geometry intermediate between Dod and BCTP. The four Fe(III) ions each have octahedral environments: [*fac*-FeO₃N₃] for Fe(1), [FeO₅N] for Fe(2), which unusually is not chelated by a diethanolamine ligand, and [*cis*-FeO₄N₂] for Fe(3) and Fe(4).

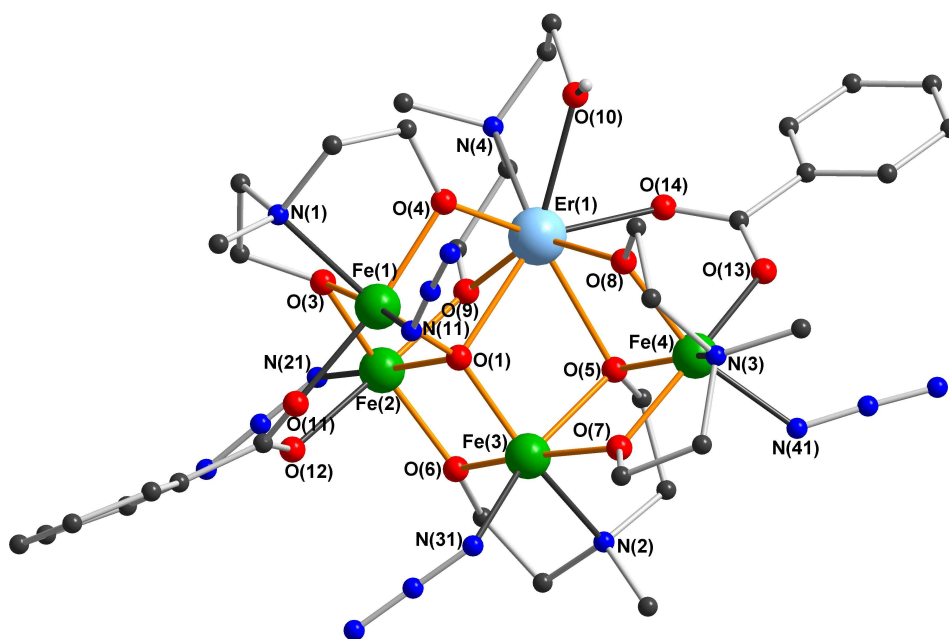


Fig. 4.26 The molecular structure of $[\text{Er}^{\text{III}}\text{Fe}_4^{\text{III}}(\mu_3\text{-O})(\text{mdea})_3(\text{mdeaH})(\text{O}_2\text{CPh})_2(\text{N}_3)_4]$. 2.5MeCN (**23**). Hydrogen atoms are omitted for clarity. Grey, red, dark blue, green and pale blue spheres represent C, O, N, Fe and Er, respectively.

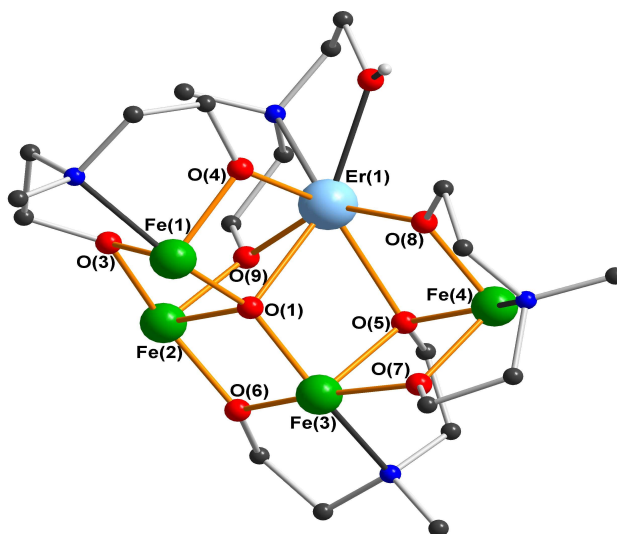


Fig. 4.27 Structure of the core of $[[\text{Fe}_4^{\text{III}}\text{Er}^{\text{III}}(\mu_4\text{-O})(\text{mdea})_3(\text{mdeaH})(\mu\text{-benzoate})_2(\text{N}_3)_4]$. Azide and benzoate ligands, and C-H hydrogen atoms, omitted for clarity.

Table 4.5 Selected bond lengths (\AA°) of compound **23**.

Er1—O1	2.404(2)	Fe2—O6	1.979(2)
Er1—O4	2.270(3)	Fe2—O1	2.102(2)
Er1—O5	2.490(2)	Fe3—O1	1.934(2)
Er1—O8	2.233(2)	Fe3—O5	2.117(2)
Er1—O9	2.298(2)	Fe3—O6	2.012(2)
Fe1—O1	1.920(2)	Fe3—O7	1.962(2)
Fe1—O4	1.990(2)	Fe4—O5	2.042(2)
Fe1—O3	2.081(2)	Fe4—O7	1.989(2)
Fe2—O3	1.968(2)	Fe4—O8	1.958(2)

4.3.2 Magnetic properties of $[\text{Er}^{\text{III}}\text{Fe}_4^{\text{III}}(\mu_3\text{-O})(\text{mdea})_3(\text{mdeaH})(\text{O}_2\text{CPh})_2(\text{N}_3)_4] \cdot 2.5\text{MeCN}$ (**23**)

Variable temperature dc magnetic susceptibility data were collected for compound **23** (Fig. 4.28) in the temperature range 300–1.8 K in an applied field of 1000 Oe. At room temperature, the χT product value is $27.60 \text{ cm}^3 \text{ K mol}^{-1}$ which is in agreement with the expected value for four Fe(III) ions ($S = 5/2$, $g = 2$, $C = 4.375 \text{ cm}^3 \text{ K mol}^{-1}$) and one Er(III) ion ($S = 3/2$, $L = 6$, $g = 6/5$, ${}^4\text{I}_{15/2}$, $C = 11.5 \text{ cm}^3 \text{ K mol}^{-1}$)^[93]. On decreasing the temperature, the χT product at 1000 Oe continuously decreases to reach $11.97 \text{ cm}^3 \text{ K mol}^{-1}$ at 1.8 K indicating the presence of antiferromagnetic interactions within the complexes. However, the thermal depopulation of the

Stark sublevels of the anisotropic Er ion^[90] might be also responsible for the thermal decrease of the χT product. Therefore if the χT product decreases with the temperature it is not possible to be sure that this behavior is associated with dominant antiferromagnetic interactions within the complexes.

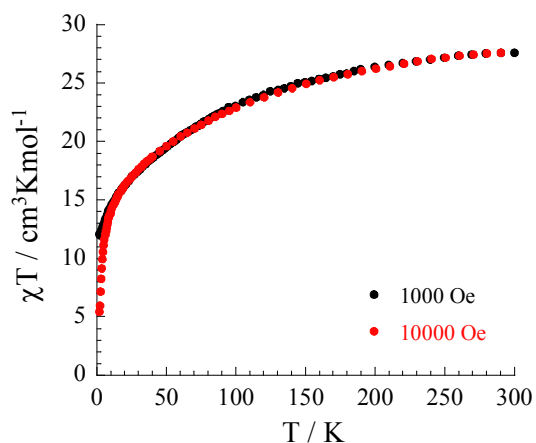


Fig. 4.28 Temperature dependence of χT product for compound **23**.

The field dependence of the magnetisation at low temperature of compound **23** show that the magnetisation smoothly increases with the applied dc field. In this case, there is no clear saturation even at 7 T at which it reaches the value of $10.5 \mu_B$ for **23**, suggesting the presence of magnetic anisotropy and/or the population of low-lying excited states. Moreover, while plotting the M versus H/T at low temperatures (Fig.4.29) the curves are not all superimposed on a single master-curve, further indicating the presence of magnetic anisotropy and/or low-lying excited states. The magnetisation show a small kink centred at ~ 2.6 T and then a smooth increase without saturation (Fig. 4.30). The shape of magnetisation curves further suggests that low-lying excited states are progressively populated with the increase of external field. In addition, the ac susceptibility of **23** in zero dc field shows a complete absence of out-of-phase component above 1.8 K

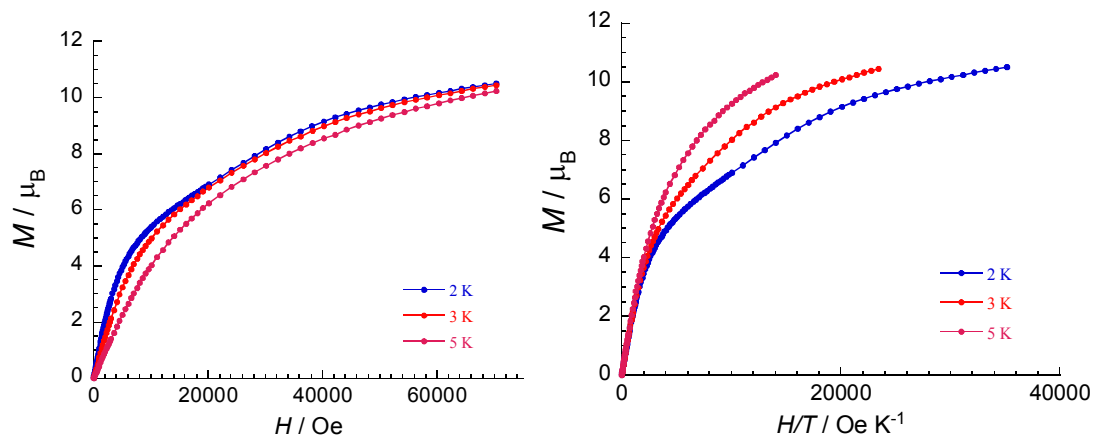


Fig. 4.29 Field dependence of magnetization at indicated temperatures for compound **23**.

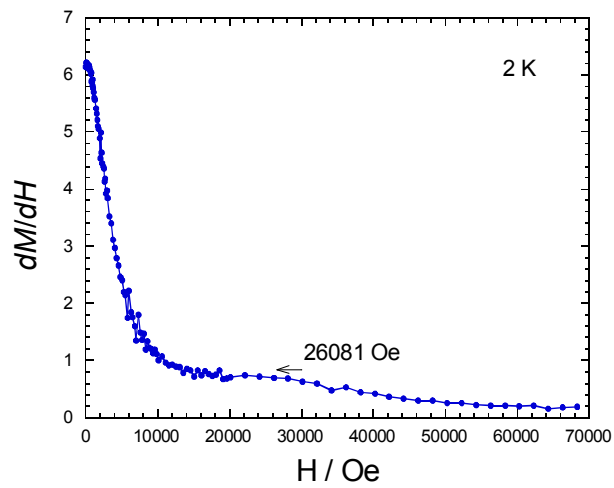
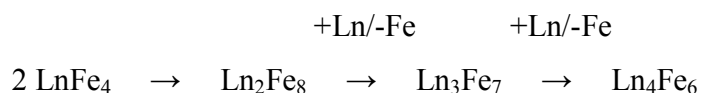


Fig. 4.30 Plot of dM/dH versus H for compound **23**.

4.4 Conclusion

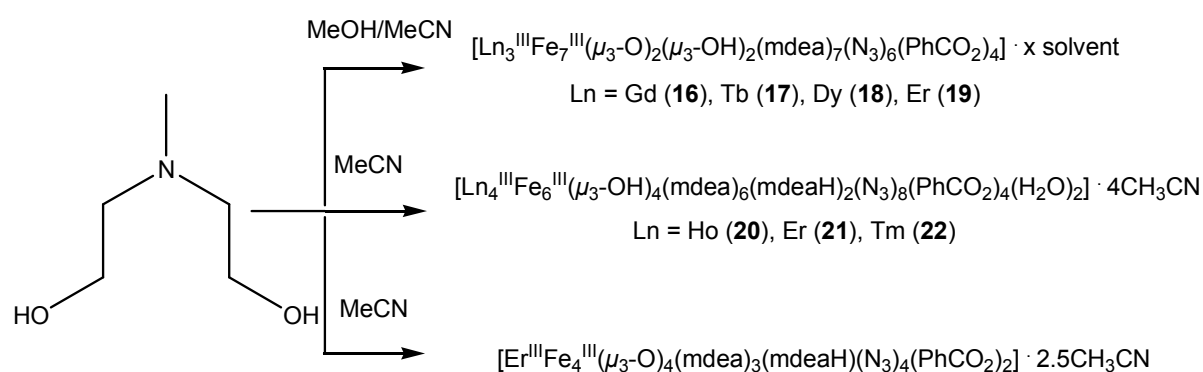
In this chapter a new group of mixed 3*d*-4*f* (Fe-Ln) decanuclear clusters has been synthesised from the reactions of Fe(III), benzoic acid, NaN₃ and mdeaH₂, using acetonitrile or simply by methanolysis (scheme 3). Two different series of decanuclear compounds were synthesised and structurally and magnetically characterised. The first includes four compounds of general formula [Ln^{III}₃Fe^{III}₇(μ₄-O)₂(μ₃-OH)₂(N₃)₆(mdea)₇(PhCO₂)₄].6MeCN (**16-19**). The second contains three compounds with the formula [Ln₄^{III}Fe₆^{III}(μ₃-OH)₄(mdea)₆(mdeaH)₂(N₃)₈(PhCO₂)₄(OH₂)₂].4MeCN. Both series were derived from the same reaction system. In the case of lanthanides with large radius, decanuclear compounds containing three lanthanide and seven iron ions were obtained. In the case of lighter lanthanide, decanuclear compounds consisting of six iron and four lanthanide ions were obtained. By changing the metal ions to ligand ratio, a new pentanuclear compound **23** was obtained. This finding may suggest that there is a correlation between the pentanuclear and the decanuclear compounds. A more carefully study of all the crystal structures concludes in possible reaction mechanism which can be considered as follow:



From the magnetic point of view, the first series has some compounds that exhibit antiferromagnetic interactions (**16,17**) whereas others exhibit slow relaxation of magnetisation and might be good candidates for SMMs. In the second series, antiferromagnetic interactions were found dominant in compounds **20**, **21** and **22**. However compound **23** shows slow relaxation of magnetisation and might be a SMM. Compound **23** exhibits dominant antiferromagnet interactions. These products represent new additions to what is still a small, but growing, family of such mixed-metal species. While the magnetic properties are complicated by the large spin-orbit coupling effects of most Ln(III) ions, making the quantitative elucidation of the magnitude of the exchange parameters and their resulting ground state description difficult, hysteresis loop determinations have established that additional examples of SMMs have been discovered. However, lanthanide-containing SMMs still suffer from the disadvantage of fast quantum tunnelling of magnetisation (QTM) rates. This represents a diminution of the effective barrier for

magnetisation relaxation, and thus the temperature below which the relaxation is blocked and below which the complex will function as a SMM is lowered. Nevertheless, the use of lanthanides to modulate the magnetic properties of transition metal SMMs is still an interesting area that promises much new science as it matures.

In conclusion, in this chapter a Ln/Fe/MdeaH₂/Benzoate system was developed. Depending on the solvent, Ln₃Fe₇ or Ln₄Fe₆ clusters can be obtained. Some of them show SMM behaviour, therefore SMM properties can be tuned upon the solvent selection.



Scheme 3 The synthetic route of compounds **16-19**, **20-22** and **23**.

Chapter 5: Summary

This research has produced compounds exhibiting a wide range of structural motifs and interesting magnetic properties. The results are divided into two parts, each of which illustrates one kind of cluster aggregate. In Chapter 3, *4f* aggregates are discussed, whereas Chapter 4 highlights *3d-4f* (Fe-Ln) heterometallic clusters.

In **Chapter 3**, a series of six dinuclear $[\text{Ln}_2(\text{mdeaH}_2)(\text{piv})_6]$ **1-6**, five tetranuclear $[\text{Ln}_4(\mu_3\text{-OH})_2(\text{mdeaH})_2(\text{piv})_8]$ **7-11** and four tetranuclear $[\text{Ln}_4(\text{mdea})_2(\text{mdeaH})_2(\text{PhCO}_2)_6]$ **12-15** compounds were successfully synthesised, crystallographically characterised and magnetically studied. The dinuclear compounds **1-6** and the tetranuclear compound **7-11** derived from the same reaction system containing mdeaH_2 , pivalic acid and Ln(III) ions, but from the structural point of view the final product is influenced by the size of the lanthanide centre. For lanthanides with a large radius, dinuclear compounds were isolated while for the heavier lanthanides tetranuclear compounds are obtained. Each binuclear complex **1-6** is linked by hydrogen bonds to four other dimers, resulting in a 2D supramolecular structure. Tetranuclear compounds **7-11** are isostructural having a “butterfly” core. On varying co-ligands, for example, by using benzoic acid, a series of four isostructural tetranuclear $[\text{Ln}_4(\text{mdea})_2(\text{mdeaH})_2(\text{PhCO}_2)_6]$ (**12-15**) possessing a crystallographically different core is obtained. They are more distorted compared to compounds **7-11**.

From the magnetic point of view, compounds **2-5** exhibit weak antiferromagnetic interactions. The field dependence at low temperature for **2-5** indicate the presence of magnetic anisotropy and or the lack of a well-defined ground state suggesting the presence of low-lying excited states that might be populated when a field is applied. In contrast, compound **6** displays weak ferromagnetic interactions. As Gd(III) has essentially no orbital contribution, it can be considered as an isotropic $S = 7/2$ spin. For dinuclear compounds **1-6** the exchange coupling between the lanthanides is very weak to the point of being virtually non-existent. Thus it would seem that in complexes of this type, the *syn-syn* carboxylate bridges do not allow for any significant magnetic interactions between the lanthanide centres. As for the tetranuclear compounds (**7, 9, 10** and **11**) coupling between the Ln centres is antiferromagnetic, while for compound **8**, the field dependence at low temperature indicated the presence of anisotropy. The M versus H data reveal at 1.8 K the existence of hysteresis with a very small coercive field (about

12 Oe). In zero dc field, frequency dependent in-phase and out-of-phase signals were observed below 12 K indicating slow relaxation of the magnetisation. The out-of-phase signals were observed at 2.5 K and 1500 Hz. The out-of-phase signal possesses a reasonable intensity in comparison to the in-phase signal. The shape and frequency dependence strongly suggests that it is a SMM. Fitting the data to an Arrhenius law, the characteristic SMM energy barrier, Δ , was estimated to be 6.2 K and the pre-exponential factor, τ_0 , 2.45×10^{-5} s.

Magnetic studies carried out on compounds **12-15** revealed that compounds **12** and **13** exhibit slow relaxation of magnetisation and show SMM behaviour. In zero dc field, both compounds show frequency dependent in-phase and out-of-phase signals below 12 K indicating slow relaxation of the magnetisation. In the case of compound **12** there is no out-of-phase signal observed even at 1.8 K, which indicates that the blocking temperature of this compound is below 1.8 K. Compound **13** exhibits two maxima in the out-of-phase susceptibility observed at 2.5 K and 10 K at a frequency of 1500 Hz therefore the energy barrier of the slow relaxation is small. Fitting the frequency sweeping ac susceptibilities as a function of temperature to the Arrhenius law, the SMM energy barrier (Δ) and the pre-exponential factor are deduced as follows: process 1 (> 5 K): $\Delta_1 = 34.5$ K, $\tau_0 = 1.86 \cdot 10^{-5}$ s; and process 2 (< 5 K): $\Delta_2 = 5.4$ K, $\tau_0 = 8.1 \cdot 10^{-3}$ s. However, in compounds **14** and **15**, antiferromagnetic interactions are dominant. It is noted that for $4f$ systems, hydroxide bridges can mediate weak but significant magnetic interactions, as previously found to be the case for a Dy_3 triangle, suggesting that future synthetic efforts should attempt to incorporate such superexchange pathways. The results suggest that one of the main contributions lanthanides make to magnetic behaviour in molecular systems arises from the possibility of providing significant anisotropy, which is an especially desirable feature in the design of new single molecule magnets.

In **Chapter 4** a new group of mixed $3d-4f$ (Fe-Ln) decanuclear clusters has been synthesised from the reactions of Fe(III), benzoic acid, NaN_3 and mdeaH₂, using acetonitrile or simply through solvolysis in methanol. Two different series of decanuclear compounds were synthesised and structurally and magnetically characterised. The first includes four compounds of general formula $[Ln_3^{III}Fe_7^{III}(\mu_4-O)_2(\mu_3-OH)_2(N_3)_6(mdea)_7(PhCO_2)_4] \cdot 6 \cdot MeCN$ (**16-19**). The second series contain three compounds with the formula $[Ln_4Fe_6(\mu_3OH)_4(mdea)_6(mdeaH)_2(N_3)_8(PhCO_2)_4(OH_2)_2]$. Both series were derived from the same reaction system. In the case of lanthanides with a large radius, decanuclear compounds containing three lanthanide and seven iron ions were obtained. In the case of lighter lanthanides, decanuclear

compounds consisting of six iron and four lanthanide ions were obtained. By changing the metal-ion-to-ligand ratio, a new pentanuclear compound **23** was also obtained.

From the magnetic point of view, the first series of compounds exhibit antiferromagnetic interactions (**16**, **17**) whereas others exhibit slow relaxation of magnetisation and might be good candidates for SMMs (**17**, **18**). The ac susceptibility measurements were carried out in zero dc field. Both in-phase and out-of-phase signals are frequency dependent, suggesting that these compounds exhibit slow relaxation and might be SMMs. For compound **18**, after extracting the characteristic relaxation time (τ) of the system from both data sets, τ was found to follow the Arrhenius law with the characteristic SMM energy barrier, Δ , estimated to be 30.9 K, which is the highest energy barrier in Fe-Ln complexes and the pre-exponential factor (τ_0) is $1.3 \cdot 10^{-7}$ s. In the second series, antiferromagnetic interactions were found dominant in compounds **20**, **21** and **22**. However compound **21** shows slow relaxation of magnetisation and might be a SMM. Compound **23** consists of the pentanuclear compound $[\text{Er}^{\text{III}}\text{Fe}_4^{\text{III}}(\mu_3\text{-O})(\text{mdea})_3(\text{mdeaH})(\text{O}_2\text{CPh})_2(\text{N}_3)_4]$ which exhibits dominant antiferromagnetic interactions. These products represent new additions to what is still a very small family of such mixed-metal species. While the magnetic properties are complicated by the large spin-orbit coupling effects of most Ln(III) ions, making the quantitative elucidation of the exchange parameters and their resulting ground state description difficult, hysteresis loop determinations have established that additional examples of SMMs have been discovered. However, lanthanide-containing SMMs still suffer from the disadvantage of fast quantum tunneling of magnetisation (QTM) rates. This represents a diminution of the effective barrier for magnetisation relaxation, and thus the temperature below which the relaxation is blocked and below which the complex will function as a SMM is lowered.

Finally, the synthesis of polynuclear metal clusters has been achieved, in principle, by controlling the hydrolysis of the metal ion either in an aqueous solution or in a mixture of organic solvents in the coexistence of the supported ligands. A finite aggregate of oxygen-bridged metal ions is thus trapped within a shell of organic ligands, rather than proceeding to the formation of an extended oxide or hydroxide mineral structure. In order to explain in an appropriate way the magnetic interactions in these compounds, crystalline materials are the desirable products which can be characterised well by X-ray crystallography. It is well known that the solvent, the concentration of the reactants, the temperature at which the reaction takes place, the ratio of the reactants and the pH of the final solution affect the final product. In order to synthesise high-

nuclearity metal clusters. a metal to ligand and co-ligand ratio in the system should be carefully selected.

Chapter 6: Experimental

The reagents used throughout this research were bought from commercial suppliers and were used without further purification.

6.1 Preparation of inorganic materials

6.1.1 Preparation of [La₂(mdeaH₂)(Piv)₆] (1)

A solution of *N*-methyldiethanolamine (0.148 g, 1.25 mmol) in CH₃CN (20 ml) was added dropwise over 20 minutes to a stirred solution of La(NO₃)₃·6H₂O (0.108g, 0.25 mmol) and pivalic acid (0.076 g, 0.75 mmol) in CH₃CN (20 ml). The mixture was heated under reflux for 1 hour, after which it was cooled at room temperature and then allowed to stand undisturbed in a sealed vial. Colourless cubic crystals of (3) suitable for X-ray crystallography were obtained overnight. The crystals of (3) were maintained in mother liquor for X-ray crystallography or collected by filtration, washed with CH₃CN and dried; Yield; 50% Anal. Calcd. (found) for (3) C₄₀H₈₀N₂O₁₆La₂: C, 42.78 (42.66); H, 7.18 (6.83); N, 2.49 (2.71)%. IR (KBr): ν (cm⁻¹) = 3425 (w), 2957 (m), 2925 (w), 2865 (w), 2030 (w) 1606 (vs), 1533 (s), 1484 (s), 1458 (w), 1421 (s), 1372 (w), 1360 (m), 1228 (s), 1135 (w), 1083 (m), 1028 (w), 974 (w), 941 (w), 894 (m), 803 (w), 785 (m), 602 (m), 543 (m).

6.1.2 Preparation of [Ce₂(mdeaH₂)(Piv)₆] (2)

This compound was prepared following the preceding procedure using Ce(NO₃)₃·6H₂O (0.110 g, 0.25 mmol). Yield; 53% Anal. Calcd. (found) for (2) C₄₀H₈₀N₂O₁₆Ce₂: C, 42.69 (40.02); H, 7.11 (6.56); N, 2.49 (2.24)%. IR (KBr): ν (cm⁻¹) = 3413 (w), 2954 (m), 2924 (w), 2900 (w), 2865 (w), 2825 (w), 1609 (vs), 1531 (s), 1484 (s), 1458 (m), 1417 (s), 1372 (m), 1360 (m), 1329 (w), 1294 (w), 1254 (w), 1229 (s) 1137 (w), 1083 (s), 1063 (w) 1052 (w), 1029 (m), 975 (m), 941 (w), 903 (w), 890 (m), 864 (w), 803 (w), 785 (m), 769 (w), 596 (m), 563 (w), 543 (m).

6.1.3 Preparation of [Pr₂(mdeaH₂)(Piv)₆] (3)

This compound was prepared following the preceding procedure using Pr(NO₃)₃·6H₂O (0.108g, 0.25 mmol). Yield; 54%. Anal. Calcd. (found) for (5) C₄₀H₈₀N₂O₁₆Pr₂: C, 42.59 (42.66); H, 7.09

(6.86); N, 2.48 (2.66)%. IR (KBr): ν (cm⁻¹) = 3429 (w), 2954 (m), 2924 (w), 2902 (w), 2866 (w), 2824 (w), 1613 (vs), 1531 (s), 1484 (s), 1458 (m), 1416 (s), 1372 (m), 1360 (m), 1327 (m), 1293 (m), 1230 (s), 1151 (w), 1137 (w), 1084 (s), 1052 (w), 1029 (m), 975 (m), 941 (w), 903 (w), 890 (m), 864 (w), 803 (w), 785 (m), 770 (w), 596 (m), 564 (w), 543 (m).

6.1.4 Preparation of [Nd₂(mdeaH₂)(Piv)₆] (4)

This compound was prepared following the preceding procedure using Nd(NO₃)₃·6H₂O (0.112g, 0.25 mmol). Yield; 40% Anal. Calcd. (found) for (3) C₄₀H₈₀N₂O₁₆Nd₂: C, 42.38 (42.41); H, 7.06 (6.91); N, 2.47 (2.65)%. IR (KBr): ν (cm⁻¹) = 3429 (w), 2954 (m), 2924 (w), 2901 (w), 2865 (w), 2827 (w) 2065 (w), 1615 (vs), 1583 (w), 1532 (s), 1484 (s), 1426 (m), 1417 (m), 1389 (w), 1372 (m), 1360 (m), 1325 (w), 1293 (w), 1267 (w), 1151 (w), 1137 (w), 1084 (s), 1052 (w), 1028 (m), 975 (m), 941 (w), 903 (w), 891 (s), 866 (m), 802 (w), 785 (s), 770 (w), 596 (s), 565 (w), 544 (m).

6.1.5 Preparation of [Sm₂(mdeaH₂)(Piv)₆] (5)

This compound was prepared following the preceding procedure using Sm(NO₃)₃·6H₂O (0.108g, 0.25 mmol). Yield; 45% Anal. Calcd. (found) for (7) C₄₀H₈₀N₂O₁₆Sm₂: C, 41.93 (41.35); H, 6.98 (6.84); N, 2.44 (2.59)%. IR (KBr): ν (cm⁻¹) = 3411 (w), 2956 (m), 2924 (w), 2901 (w), 2865 (w), 2828 (w), 1625 (vs), 1582 (w), 1531 (s), 1484 (s), 1458 (m), 1420 (s), 1389 (w), 1373 (m), 1360 (m), 1322 (w), 1292 (w), 1267 (w) 1230 (vs), 1152 (w), 1137 (m), 1084 (vs), 1052 (w), 1029 (m), 975 (m), 941 (w), 903 (w), 892 (s), 867 (m), 801 (w), 785 (s), 770 (w), 596 (s), 567 (m), 546 (m), 459 (w), 445 (m).

6.1.6 Preparation of [Gd₂(mdeaH₂)(Piv)₆] (6)

A solution of *N*-methyldiethanolamine (0.089 g, 0.75 mmol) in CH₂Cl₂ (20 ml) was added dropwise over 20 minutes to a stirred solution of Gd(NO₃)₃·6H₂O (0.113 g, 0.25 mmol) and pivalic acid (0.076 g, 0.75 mmol) in CH₃CN (20 ml). The mixture was heated under reflux for 1 hour, after which it was cooled at room temperature. Colourless cubic crystals of (8) suitable for X-ray crystallography were obtained after three days. The crystals of (8) were maintained in mother liquor for X-ray crystallography or collected by filtration, washed with CH₃CN and dried; Yield: 30% Anal. Calcd. (found) for (8) C₄₀H₈₀N₂O₁₆Gd₂: C, 41.39 (41.25); H, 6.89 (6.66); N, 2.41(2.51)%. IR (KBr): ν (cm⁻¹) = 3420 (w), 2957 (m), 2924 (w), 2901 (w), 2865 (w), 2830 (w),

1630 (vs), 1534 (s), 1484 (s), 1459 (m), 1421 (s), 1373 (m), 1360 (m), 1318 (m), 1290 (m), 1229 (s), 1152 (w), 1137 (w), 1085 (s), 1052 (w), 1028 (m), 976 (m), 942 (w), 894 (s), 868 (m), 786 (s), 771 (w), 597 (s), 569 (w), 548 (w).

6.1.7 Preparation of $[\text{Tb}_4(\mu_3\text{-OH})_2(\text{mdeaH})_2(\text{piv})_8]$ (7)

A solution of *N*-methyldiethanolamine (0.089 g, 0.5 mmol) in MeCN (15 ml) was added dropwise over 20 minutes to a stirred solution of $\text{Tb}(\text{NO}_3)_3 \cdot 6\text{H}_2\text{O}$ (0.114 g, 0.25 mmol) and pivilic acid (0.101 g, 1.00 mmol) in MeCN (15 ml). The mixture was heated under reflux for 1 hour, after which it was cooled at room temperature and then allowed to stand undisturbed in a sealed vial. Colourless needles of **9** suitable for X-ray crystallography were obtained after 3 days. The crystals of **9** were maintained in mother liquor for X-ray crystallography or collected by filtration, washed with MeCN and dried; yield 45% Anal. Calcd. (found) for $\text{C}_{50}\text{H}_{98}\text{N}_2\text{O}_{22}\text{Tb}_4$: C, 34.98 (35.07); H, 5.71 (5.82); N, 1.63 (1.35)%. IR (KBr): ν (cm^{-1}) = 3414 (w), 2959 (s), 2926 (w), 2867 (w), 2812 (w), 1566 (vs), 1513 (w), 1485 (s), 1459 (m), 1423 (s), 1375 (m), 1360 (m), 1321 (w), 1228 (s), 1137 (w), 1085 (s), 1046 (w), 1030 (w), 995 (w), 971 (w), 937 (w), 896 (s), 808 (m), 792 (m), 774 (w), 658(w), 607 (m), 561 (w), 464 (w).

6.1.8 Preparation of $[\text{Dy}_4(\mu_3\text{-OH})_2(\text{mdeaH})_2(\text{piv})_8]$ (8)

This compound was prepared following the preceding procedure using $\text{DyCl}_3 \cdot x\text{H}_2\text{O}$ (0.068 g). Yield; 46% Anal. Calcd. (found) for (2) $\text{C}_{50}\text{H}_{98}\text{N}_2\text{O}_{22}\text{Dy}_4$: C, 34.69 (31.13); H, 5.66 (4.88); N, 1.61(1.83) IR (KBr): (cm^{-1}) ν = 3423 (w), 2960 (s), 2927 (w), 2867 (w), 1566 (vs), 1514 (m), 1485 (s), 1423 (s), 1376 (m), 1361 (m), 1320 (w), 1327 (m), 1228 (s), 1151 (w), 1137 (w), 1086 (w), 1077 (w), 1046 (w), 971 (w), 938 (w), 897 (m), 808 (m), 792 (m), 776 (w), 608 (m), 559 (w), 468(w).

6.1.9 Preparation of $[\text{Ho}_4(\mu_3\text{-OH})_2(\text{mdeaH})_2(\text{piv})_8]$ (9)

This compound was prepared following the preceding procedure using $\text{HoCl}_3 \cdot x\text{H}_2\text{O}$ (0.098 g) Yield; 45% Anal. Calcd (found) for $\text{C}_{50}\text{H}_{98}\text{N}_2\text{O}_{22}\text{Ho}_4$: C, 34.50 (34.13); H, 5.63 (4.75); N, 1.61 (1.85)%. IR (KBr): ν (cm^{-1}) = 3434 (m), 2960 (s), 2926 (w), 2866 (w), 1567 (vs), 1544 (w), 1485 (s), 1459 (m), 1426 (s), 1376 (m), 1360 (m), 1319 (w), 1229 (s), 1137 (w), 1088 (s), 1046 (w), 971 (w), 937 (w), 898 (s), 809 (m), 792 (m), 658(w), 608 (m), 562 (w), 468 (w).

6.1.10 Preparation of $[\text{Er}_4(\mu_3\text{-OH})_2(\text{mdeaH})_2(\text{piv})_8]$ (10)

This compound was prepared following the preceding procedure using $\text{ErCl}_3 \cdot x\text{H}_2\text{O}$ (0.068 g).

Yield; 35% Anal. Calcd. (found) for $\text{C}_{50}\text{H}_{98}\text{N}_2\text{O}_{22}\text{Er}_4$: C, 34.31 (34.87); H, 5.60 (5.81); N, 1.60 (1.34)%. IR (KBr): ν (cm^{-1}) = 3427 (m), 2960 (s), 2923 (w), 2865 (w), 1568 (vs), 1516 (m), 1485 (s), 1460 (w), 1422 (s), 1376 (m), 1360 (m), 1318 (w), 1229 (s), 1137 (w), 1089 (s), 1046 (w), 971 (w), 937 (w), 898 (s), 809 (m), 792 (m), 608 (m), 562 (w), 470 (w).

6.1.11 Preparation of $[\text{Tm}_4(\mu_3\text{-OH})_2(\text{mdeaH})_2(\text{piv})_8]$ (11)

This compound was prepared following the preceding procedure using $\text{TmCl}_3 \cdot 6\text{H}_2\text{O}$ (0.068 g, 0.25 mmol). Yield; 45% Anal. Calcd. (found) for $\text{C}_{50}\text{H}_{98}\text{N}_2\text{O}_{22}\text{Tm}_4$: C, 34.18 (34.14); H, 5.58 (5.38); N, 1.59 (1.82)%. IR (KBr): ν (cm^{-1}) = 3412 (m), 2960 (s), 2926 (w), 2866 (w), 1570 (vs), 1546 (w), 1518(w) 1485 (s), 1459 (m), 1432 (s), 1376 (m), 1360 (m), 1318 (w), 1229 (s), 1137 (w), 1089 (s), 1064(w), 1046 (w), 971 (w), 938 (w), 899 (s), 810 (m), 792 (m), 683(w), 608 (m), 563 (w), 472 (w).

6.1.12 Preparation of $[\text{Tb}_4(\text{mdea})_2(\text{mdeaH})_2(\text{PhCO}_2)_{4.5}(\text{NO}_3)_{1.5}]$ (12)

A solution of *N*-methyldiethanolamine (0.148 g, 1.25 mmol) in MeCN (20 ml) was added dropwise over 20 minutes to a stirred solution of $\text{Tb}(\text{NO}_3)_3 \cdot 6\text{H}_2\text{O}$ (0.114 g, 0.25 mmol) and benzoic acid (0.030 g, 0.25 mmol) in MeCN (20 ml). The resulting mixture was stirred at room temperature for more 30 minutes, after which it was filtered and allowed to stand undisturbed in a sealed vial. Colourless needles of (12) were obtained after 3 days. The crystals of (12) were washed with MeCN and dried. Yield; 45% Anal. Calcd. (found) for $\text{C}_{51.5}\text{H}_{72.5}\text{N}_{5.5}\text{O}_{23.5}\text{Tb}_4$ (corresponds to crystallographic formula + $2\text{H}_2\text{O}$) C, 34.74 (34.53); H, 4.10 (4.00); N, 4.33 (4.35)% IR (KBr): (cm^{-1}) ν = 3421 (w), 2857 (s), 1601 (vs), 1560 (vs), 1494 (m), 1423 (s), 1461 (w), 1415 (s), 1290 (m), 1203 (w), 1175 (w), 1080 (s), 1034 (m), 1003 (w), 976 (m), 909 (w), 893 (m), 816 (w), 719 (s), 686 (m), 672 (w), 565 (m), 435(w).

6.1.13 Preparation of $[\text{Dy}_4(\text{mdea})_2(\text{mdeaH})_2(\text{PhCO}_2)_6] \cdot \text{solv}$ (13)

This compound was prepared following the preceding procedure using $\text{DyCl}_3 \cdot x\text{H}_2\text{O}$ (0.070 g). Yield; 47% Anal. Calcd. (found) for (13) $\text{C}_{66}\text{H}_{92}\text{N}_6\text{O}_{25}\text{Dy}_4$ (corresponds to

[Dy₄(mdea)₂(mdeaH)₂(PhCO₂)₆]·2MeCN·5H₂O): C, 39.25 (39.11); H, 4.59 (4.36); N, 4.16 (4.36)%. IR (KBr): (cm⁻¹) ν = 3423 (w), 2960 (s), 2927 (w), 2867 (w), 1566 (vs), 1514 (m), 1485 (s), 1423 (s), 1376 (m), 1361 (m), 1320 (w), 1327 (m), 1228 (s), 1151 (w), 1137 (w), 1086 (w), 1077 (w), 1046 (w), 971 (w), 938 (w), 897 (m), 808 (m), 792 (m), 776 (w), 608 (m), 559 (w), 468(w).

6.1.14 Preparation of [Ho₄(mdea)₂(mdeaH)₂(PhCO₂)_{4.5}(NO₃)_{1.5}] (14)

This compound was prepared following the preceding procedure using ErCl₃·xH₂O (0.067 g). Yield; 40%. Anal. Calcd. (found) for (14) C_{51.5}H_{70.5}N_{5.5}O_{22.5}Ho₄: C, 34.63 (34.52); H, 3.98 (4.17); N, 4.31 (4.73)% IR (KBr): (cm⁻¹) ν = 3374 (w), 3065(w), 2858 (s), 1602 (vs), 1562 (s), 1494 (m), 1415 (s), 1289 (s), 1203 (w), 1175 (m), 1138 (w), 1081 (s), 1034 (m), 1003 (m), 976 (m), 910 (w), 894 (m), 855 (m), 720 (s), 687(m), 673 (m), 568 (w).

6.1.15 Preparation of [Er₄(mdea)₂(mdeaH)₂(PhCO₂)₆]·0.3(mdeaH₂)·1.7MeCN·1.4H₂O (15)

This compound was prepared following the preceding procedure using ErCl₃·xH₂O (0.067 g). Yield; 35%. Anal. Calcd. (found) for (15) C_{63.5}H_{88.3}N_{4.3}O_{24.8}Er₄ (corresponds to [Er₄(mdea)₂(mdeaH)₂(PhCO₂)₆]·0.3(mdeaH₂)·4.2H₂O): C, 38.56 (38.37); H, 4.50 (4.55); N, 3.05 (2.97)% IR (KBr): (cm⁻¹) ν = 3421 (w), 3065(w), 2851 (s), 1598 (vs), 1543 (s), 1493 (m), 1416 (s), 1313 (w), 1204 (w), 1174 (m), 1139 (w), 1086 (s), 1068 (w), 1048 (w), 1024 (w), 1003 (m), 977 (m), 911 (w), 894 (m), 856 (m), 719 (s), 686(m), 673 (m), 568 (w).

6.1.16 Preparation of [Gd₃Fe₇(μ_4 -O)₂(μ_3 -OH)₂(N₃)₆(mdea)₇(PhCO₂)₄]·5MeCN (16)

A solution of *N*-methyldiethanolamine (0.148 g, 1.25 mmol) in MeCN (20 ml) was added dropwise over 20 minutes to a stirred solution of Gd(NO₃)₃·6H₂O (0.113 g, 0.25 mmol), benzoic acid (0.030 g, 0.25mmol), FeCl₃ (0.040 g, 0.25 mmol) and NaN₃ (0.051 g,0.75 mmol) in MeCN (20 ml). The mixture was heated under reflux for 1 hour, after which it was cooled to room temperature and then allowed to stand undisturbed in sealed vial. Orange needles of (16) suitable for X-ray crystallography were obtained after 15 days. The crystals of (16) were maintained in mother liquor for X-ray crystallography or collected by filtration, washed with MeCN and dried. Yield; 40%. Anal. Calcd. (found) for C₆₃H₁₀₅Gd₃Fe₇N₂₅O₂₉ (corresponds to [Gd₃Fe₇(μ_4 -O)₂(μ_3 -OH)₂(N₃)₆(mdea)₇(PhCO₂)₄]·3H₂O) C, 29.80 (29.91); H, 4.18 (3.92); N, 13.79 (13.79)%. IR (KBr):

ν (cm⁻¹) = 3424 (w), 2856 (w), 2059 (vs), 1625 (m), 1597 (m), 1547 (m), 1447 (w), 1399 (m), 1084 (s), 1026 (w), 1000 (w), 998 (m), 721 (m), 650(w), 577 (w), 490 (w).

6.1.17 Preparation of [Tb₃Fe₇(μ_4 -O)₂(μ_3 -OH)₂(N₃)₆(mdea)₇(PhCO₂)₄]·5MeCN (17)

This compound was prepared following the preceding procedure using Tb(NO₃)₃·6H₂O (0.114g, 0.25mmol). Yield; 45% Anal. Calcd. (found) for C₆₇H₁₀₅Tb₃Fe₇N₂₇O₂₆ (corresponds to [Tb₃Fe₇(μ_4 -O)₂(μ_3 -OH)₂(N₃)₆(mdea)₇(PhCO₂)₄]·2MeCN) C, 31.28 (31.63); H, 4.11 (3.81); N, 14.70 (14.35)%. IR (KBr): ν (cm⁻¹) = 3421 (w), 2861 (m), 2059 (vs), 1593 (s), 1546 (vs), 1458 (w), 1400 (s), 1332 (w), 1287(w), 1261 (w), 1144 (w), 1086 (s), 1026 (m), 999 (m), 897 (m), 721 (s), 654(w), 578 (m), 491 (w)

6.1.18 Preparation of [Dy₃Fe₇(μ_4 -O)₂(μ_3 -OH)₂(N₃)₆(mdea)₇(PhCO₂)₄]·2H₂O·7MeOH (18)

This compound was prepared following the preceding procedure using DyCl₃·xH₂O (0.070 g) and methanol as a solvent. Yield; 40%. Anal. Calcd. (found) for C₆₃H₁₀₃Dy₃Fe₇N₂₅O₂₈ (corresponds to [Dy₃Fe₇(μ_4 -O)₂(μ_3 -OH)₂(N₃)₆(mdea)₇(PhCO₂)₄]·2H₂O) C, 29.82 (29.97); H, 4.09 (4.02); N, 13.80 (13.79)%. IR (KBr): ν (cm⁻¹) = 3421 (w), 2926 (w), 2058 (vs), 1594 (w), 1548 (m), 1400 (s), 1259 (w), 1088 (m), 1026 (w), 1000 (w), 997 (w), 720 (m), 655(w), 578 (w), 488 (w).

6.1.19 Preparation of [Er₃^{III}Fe₇^{III}(μ_4 -O)₂(μ_3 -OH)₂(N₃)₆(mdea)₇(PhCO₂)₄]·5MeOH (19)

The compound was prepared following by preceding procedure using ErCl₃·xH₂O (0.067 g). Yield; 44%. Anal. Calcd. (found) for C₇₁H₁₃₅Er₃Fe₇N₂₅O₃₈ (corresponds to [Er₃Fe₇(μ_4 -O)₂(μ_3 -OH)₂(N₃)₆(mdea)₇(PhCO₂)₄]·8MeOH·4H₂O) C, 30.82 (29.73); H, 4.65 (3.83); N, 12.84 (11.95)%. IR (KBr): ν (cm⁻¹) = 3438 (w), 2921 (w), 2856 (w), 2059 (vs), 1593 (m), 1548 (s), 1455 (w), 1400 (m), 1287 (w), 1087 (m), 1026 (w), 1000 (w), 897(m),721 (m), 659(w), 579 (w), 493 (w).

6.1.20 Preparation of [Ho₄Fe₆(μ_3 -OH)₄(mdea)₆(mdeaH)₂(N₃)₈(PhCO₂)₄(OH₂)₂]·4MeCN (20)

A solution of *N*-methyldiethanolamine (0.148 g, 1.25 mmol) in MeCN (20 ml) was added drop wise over 20 minutes to a stirred solution of HoCl₃·xH₂O (0.067 g), benzoic acid (0.030 g, 0.25 mmol), FeCl₃ (0.040 g, 0.25 mmol) and NaN₃ (0.051g,0.75 mmol) in MeCN (20 ml). The mixture was heated under reflux for 2 hours, after which it was cooled to room temperature and then allowed to stand undisturbed in a sealed vial. Orange needles of (22) suitable for X-ray

crystallography were obtained after 15 days. The crystals of **(22)** were maintained in mother liquor for X-ray crystallography or collected by filtration, washed with MeCN and dried. Yield; 45%. Anal. Calcd. (found) for $C_{76}H_{116}Fe_6Ho_4N_{36}O_{30}$ C, 30.31 (29.95); H, 3.88 (4.23); N, 16.75 (15.69)%. IR (KBr): ν (cm^{-1}) = 3425 (w), 2862 (w), 2066 (vs), 1620(w), 1597 (s), 1557 (s), 1493 (w), 1446 (w), 1391 (s), 1337 (w), 1144 (w), 1084 (s), 1025 (m), 997 (m), 899 (m), 721 (m), 675(w), 579 (w), 510 (w), 464 (w).

6.1.21 Preparation of $[Er_4Fe_6(\mu_3-OH)_4(mdea)_6(mdeaH)_2(N_3)_8(PhCO_2)_4(OH_2)_2] \cdot 4MeCN$ (**21**)

This compound was prepared following the preceding procedure using $ErCl_3 \cdot xH_2O$ (0.067 g). Yield; 43%. Anal. Calcd. (found) for $C_{72}H_{110}Er_4Fe_6N_{34}O_{30}$ (corresponds to $[Er_4Fe_6(\mu_3-OH)_4(mdea)_6(mdeaH)_2(N_3)_8(PhCO_2)_4(OH_2)_2] \cdot 2MeCN$) C, 29.45 (29.26); H, 3.78 (3.12); N, 16.22 (16.55)%. IR (KBr): ν (cm^{-1}) = 3441 (w), 2858 (w), 2066 (vs), 1597 (s), 1557 (s), 1492 (w), 1446 (w), 1391 (s), 1286 (w), 1142 (w), 1085 (s), 1025 (w), 997 (m), 899 (m), 721 (m), 675(w), 578 (w), 510 (w), 464 (w).

6.1.22 Preparation of $[Tm_4Fe_6(\mu_3-OH)_4(mdea)_6(mdeaH)_2(N_3)_8(PhCO_2)_4(OH_2)_2] \cdot 4MeCN$ (**22**)

This compound was prepared following the preceding procedure using $TmCl_3 \cdot 6H_2O$ (0.067 g, 0.25 mmol). Yield; 45%. Anal. Calcd. (found) for $C_{72}H_{110}Tm_4Fe_6N_{34}O_{30}$ (corresponds to $[Tm_4Fe_6(\mu_3-OH)_4(mdea)_6(mdeaH)_2(N_3)_8(PhCO_2)_4(OH_2)_2] \cdot 2MeCN$) C, 29.39 (29.67); H, 3.77 (4.15); N, 16.18 (15.71)%. IR (KBr): ν (cm^{-1}) = 3441 (w), 2858 (w), 2066 (vs), 1597 (s), 1557 (s), 1492 (w), 1446 (w), 1391 (s), 1286 (w), 1142 (w), 1085 (s), 1025 (w), 997 (m), 899 (m), 721 (m), 675(w), 578 (w), 510 (w), 464 (w).

6.1.23 Preparation of $[ErFe_4(\mu_4-O)(mdea)_3(mdeaH)(O_2CPh)_2(N_3)_4] \cdot 2.5MeCN$ (**23**)

A solution of *N*-methyldiethanolamine (0.030 g, 0.025 mmol) in MeCN (20 ml) was added dropwise over 20 minutes to a stirred solution of $ErCl_3 \cdot xH_2O$ (0.067 g), benzoic acid (0.030 g, 0.25 mmol), $FeCl_3$ (0.080 g 0.5 mmol) and NaN_3 (0.034 g, 0.5 mmol) in MeCN (20 ml). The mixture was heated under reflux for 2 hours, after which it was cooled to room temperature and then allowed to stand undisturbed in a sealed vial. Orange needles of **(26)** suitable for X-ray crystallography were obtained after 15 days. The crystals of **(26)** were maintained in mother liquor

for X-ray crystallography or collected by filtration, washed with MeCN and dried. Yield; 45%
 $C_{38}H_{65}N_{18}O_{15}ErFe_4$ (corresponds to $[ErFe_4(\mu_4-O)(mdea)_3(mdeaH)(O_2CPh)_2(N_3)_4] \cdot 2MeCN$
 $\cdot 2H_2O$) C, 32.49 (32.91); H, 4.66 (4.75); N, 17.95 (17.43)%. IR (KBr): ν (cm^{-1}) = 3443 (w), 2858
(w), 2059 (vs), 1594 (s), 1548 (s), 1491 (w), 1447 (w), 1400 (s), 1288 (w), 1261 (w), 1083 (s),
1026 (w), 1000 (m), 898 (m), 721 (m), 660(w), 579 (w), 493 (w), 464 (w).

Chapter 7: Methods of characterization

7.1: FT-IR spectroscopy

Infra-red characterization were performed using a *Perkin Elmer Sperctrum One* spectrometer in the region 400cm^{-1} to 4000 cm^{-1} in transmission mode using 8 scans to resolution of 4 cm^{-1} . Spectra were obtained to provide a fingerprint of the sample. The sample was prepared by mixing the sample with KBr in a *ca.* 1:50 ratio. A disc of the sample, 1 cm in diameter, was obtained by applying 10 tones under vaccum.

7.2: Elemental analysis

The amounts of carbon, hydrogen and nitrogen in most samples were quantitatively analyzed using an *Elementar Vario El* analyzer.

7.3: X-ray powder differation

The purity of crystalline samples was checked using a *STOE Stadi P* X-ray powder diffractometer having a position sensitive detector and a germanium monochromator. Measurement were performed at room temperature using $\text{Mo-K}\alpha'$ radiation ($\lambda = 1.78897\text{ \AA}$). The diffractometer was calibrated using silicon. The data was processed using the software program *WinX^{Pow}*^[112]. Samples were finely ground and fixed between two plastic sheets with grease(*Lithylen*[®]).

7.4: X-ray crystallography

Single crystal structural characterizations have been performed using Bruker SMART Apex CCD and Stoe IPDS II area detector diffractometer. All data sets were measured using graphite monochromated $\text{Mo-K}\alpha'$ radiation^[113]. Structures were solved using direct methods, followed by full-matrix least-squares refinements against F_o^2 using the SHELXTL software package^[113]. The equations for the *R*-factor and goodness of fit *S* used in the structure refinement are:

$$wR_2 = \{\Sigma [w (F_o^2 - F_c^2)^2] / \Sigma [w (F_o^2)^2]$$

$$S = \{\Sigma [w (F_o^2 - F_c^2)^2] / (n-p)\}^{1/2}$$

$$R_I = \{\Sigma ||F_o| - |F_c||\} / \{\Sigma |F_o|\}$$

Where F_o and F_c are the observed and calculated structure factors for each reflection, while n and p are the number of unique reflections (omitting systematic absences) and the total number of parameters, respectively. The weighting factor, w , is defined as:

$$w^{-1} = \{\sigma^2(F_o^2) + (\alpha P)^2 + bP\}$$

where P is;

$$\max(F_o^2, 0) + 2 F_c^2 / 3$$

wR_2 is the function minimized during the refinement process, and all reflections (except those having large negative value or that have been flagged manually using OMIT as ‘bad reflection’) were used in refinement, and for the calculation of S .

7.5: Magnetic measurements

magnetic susceptibility measurements were obtained using a *Quantum Design* MPMS-XL SQUID susceptometer with an external magnetic field of 7 T. The measurements were performed on polycrystalline samples. The magnetic data was corrected for the diamagnetic compound due to the sample holder. The diamagnetic contribution for the sample was calculated using Pascal’s constants^[114].

Chapter 8: Crystallographic data

The crystal data of structures reported in this thesis are presented here. More detailed information can be found in the files on the accompanying CD.

Table 8.01 Crystallographic measurements

Compounds	3	6
Formula	C ₄₀ H ₈₀ N ₂ O ₁₆ Pr ₂	C ₄₀ H ₈₀ N ₂ O ₁₆ Gd ₂
Molar mass g/mol	1126.88	1159.56
Crystal system	monoclinic	monoclinic
Space group	P2 ₁ /n	P2 ₁ /n
a/Å	12.2691(5)	12.1407(5)
b/Å	13.4328(6)	13.5137(5)
c/Å	15.5525(7)	15.4281(6)
α/°	90	90
β/°	96.366 (1)	96.708 (1)
γ/°	90	90
V/ Å ³	2547.53 (19)	2513.90(17)
Z	2	2
T/K	100	100
F(000)	1160	1180
ρ _{calcd} (g/cm ³)	1.469	1.532
μ(Mo-Kα)/mm ⁻¹	1.952	2.679
Diffractometer	Bruker SMART Apex	Bruker SMART Apex
Data measured	20962	17054
unique reflections	5846	5689
R _{int}	0.0194	0.0262
Data with [I>2σ(I)]	5036	4299
parameters/restraints	304/62	304/68
wR ₂ (all data)	0.0542	0.0573
R1 [I>2σ(I)]	0.0207	0.0235
GOF on F ²	1.071	1.014
largest residuals (e Å ⁻³)	+1.10/- 0.47	+1.16/- 0.55

Table 8.01 Crystallographic measurements (continued)

Compounds	7	8	9	10	11
Formula	C ₅₀ H ₉₈ N ₂ O ₂₂ Tb ₄	C ₅₀ H ₉₈ Dy ₄ N ₂ O ₂₂	C ₅₀ H ₉₈ Ho ₄ N ₂ O ₂₂	C ₅₀ H ₉₈ Er ₄ N ₂ O ₂₂	C ₅₀ H ₉₈ N ₂ O ₂₂ Tm ₄
Molar mass g/mol	1715.01	1734.38	1739.03	1748.34	1755.02
Crystal system	triclinic	triclinic	triclinic	triclinic	triclinic
Space group	P-1	P-1	P-1	P-1	P-1
Colour	colourless block	colourless block	colourless block	colourless block	colourless block
a/Å	11.690(2)	11.6333(6)	11.5997(9)	11.5786(6)	11.5849(13)
b/Å	12.590(3)	12.5247(7)	12.4766(10)	12.4649(7)	12.4410(14)
c/Å	12.785(4)	12.7437(7)	12.7131(10)	12.7065(7)	12.6697(15)
α /°	109.679(19)	109.759(1)	109.529(1)	109.510(1)	108.982(2)
β /°	98.642(19)	98.639(1)	98.669(1)	98.647(1)	98.675(2)
γ /°	102.994(17)	102.900(1)	102.859(1)	102.853(1)	102.897(2)
$V/\text{Å}^3$	1673.2(7)	1651.0(3)	1639.0(2)	1634.14(15)	1633.20(3)
Z	1	1	1	1	1
T/K	150	100	100	100	100
$F(000)$	848	852	856	860	864
$\rho_{\text{calcd}} (\text{g}/\text{cm}^3)$	1.702	1.739	1.7613	1.7765	1.7843
$\mu(\text{Mo-K}\alpha)/\text{mm}^{-1}$	4.243	4.542	4.84	5.152	5.449
Diffractionmeter	Bruker SMART Apex	Bruker SMART Apex	Bruker SMART Apex	Bruker SMART Apex	Bruker SMART Apex
Data measured	9504	13701	11391	11442	11085
unique reflections	5913	7209	6537	7106	6917
R_{int}	0.0890	0.0275	0.0339	0.0282	0.0347
Data with [$I > 2\sigma(I)$]	3005	5848	4724	5660	5097
parameters/restraints	349/87	349/87	361/90	379/92	358/3
wR_2 (all data)	0.1488	0.1024	0.1129	0.1034	0.0996
$R1$ [$I > 2\sigma(I)$]	0.0693	0.0426	0.0483	0.0430	0.0409
GOF on F^2	0.959	1.057	1.014	1.025	1.009
largest residuals ($e \text{ Å}^{-3}$)	+0.97/-1.95	+2.71/-0.82	+1.60/-0.95	+2.51/-0.86	+2.15/-0.94

Table 8.01 Crystallographic measurements (continued)

Compounds	13a	13b	13c	14
Formula	C ₇₄ H ₈₈ Dy ₄ N ₈ O ₂₀	C _{68.9} H _{90.8} Dy ₄ N ₇ O ₂₂	C ₆₈ H ₈₅ Dy ₄ N ₇ O ₂₀	C _{51.5} H _{68.5} Ho ₄ N _{5.5} O _{21.5}
Molar mass g/mol	2019.09	2019.09	2019.09	1768.03
Crystal system	monoclinic	monoclinic	monoclinic	monoclinic
Space group	P2 ₁ /n	P2 ₁ /n	P2 ₁ /c	P2 ₁ /c
Colour	colourless block	colourless block	colourless block	colourless block
a/Å	15.2067(11)	18.9483(6)	18.5279(15)	19.0132(8)
b/Å	29.4721(16)	15.4400(5)	20.4829(17)	17.2017(7)
c/Å	19.6601(13)	25.3766(8)	21.2615(18)	21.1723(9)
α/°	90	90	90	90
β/°	107.091(5)	95.164(1)	108.582(1)	114.54(1)
γ/°	90	90	90	90
V/ Å ³	8422.0(9)	7394.1(4)	7666.8(11)	6299.11(5)
Z	4	4	4	4
T/K	150	100	100	100
F(000)	4048	3973	3864	3424
ρ _{calcd} (g/cm ³)	1.624	1.814	1.707	1.865
μ(Mo-Kα)/mm ⁻¹	3.577	4.074	3.925	5.045
Diffractometer	Stoe IPDS II	Bruker SMART Apex	Bruker SMART Apex	Bruker SMART Apex
Data measured	53847	54193	50713	41371
unique reflections	17813	16108	31862	13222
R _{int}	0.0914	0.0312	0.0579	0.0434
Data with [I>2σ(I)]	12486	14480	22778	10368
parameters/restraints	817/2	817/2	847/45	752/33
wR ₂ (all data)	0.2901	0.0762	0.1631	0.0951
R1 [I>2σ(I)]	0.1079	0.0330	0.0616	0.0437
GOF on F ²	1.533	1.085	1.071	1.067
largest residuals (e Å ⁻³)	+2.20/-2.44	+1.70/-0.76	+2.38/-1.29	+1.94/-1.47

Table 8.01 Crystallographic measurements (continued)

Compounds	15	18	22	23
Formula	C _{68.90} H _{90.80} Er ₄ N ₇ O ₂₂	C ₇₀ H ₁₃₁ Dy ₃ Fe ₇ N ₂₅ O ₃₅	C ₇₆ H ₁₁₆ Tm ₄ Fe ₆ N ₃₆ O ₃₀	C ₃₉ H _{62.50} N _{18.50} O ₁₃ ErFe ₄
Molar mass g/mol	2038.13	2761.45	3024.87	1389.23
Crystal system	monoclinic	triclinic	Orthorhombic	triclinic
Space group	P2 ₁ /n	P-1	Pca2 ₁	P-1
Colour	colourless block	Orange red	Orange red	Orange red
a/Å	18.9241(9)	14.2482(17)	30.2863(11)	10.9935(8)
b/Å	15.3619(9)	17.446(2)	21.2097(8)	27.9038(20)
c/Å	25.3848(8)	21.224(2)	17.1584(6)	17.9521(13)
α/°	109.510(1)	90.430(2)	90	90
β/°	98.647(1)	92.445(2)	90	97.601(1)
γ/°	102.853(1)	98.504(2)	90	90
V/ Å ³	7347.41(9)	5212.4(11)	11021.9(7)	5458.6(7)
Z	4	2	4	4
T/K	100	100	100	100
F(000)	4005	2772	5984	2808
ρ _{calcd} (g/cm ³)	1.842	1.759	1.823	1.690
μ(Mo-Kα)/mm ⁻¹	4.600	3.152	4.034	3.615
Diffractometer	Bruker SMART Apex	Bruker SMART Apex	Bruker SMART Apex	Bruker SMART Apex
Data measured	50604	44477	70705	41620
unique reflections	16703	24716	22489	24096
R _{int}	0.0627	0.0389	0.0378	0.0305
Data with [I>2σ(I)]	13091	19922	19775	23066
parameters/restraints	841/5	1213/7	1451/121	1342/9
wR ₂ (all data)	0.1013	0.1753	0.0754	0.0633
R1 [I>2σ(I)]	0.0430	0.0551	0.0316	0.0249
GOF on F ²	1.038	1.071	1.020	0.994
largest residuals (e Å ⁻³)	+1.88/-2.14	+2.891/-1.56	+1.29/-0.73	+0.90/-0.59

Chapter 9: Bibliography

- [1] G. L. Verschuur. *Hidden attraction, The Mystery and History of Magnetism*. Oxford University Press, Oxford 1993.
- [2] W. Plass. *Chem. unserer Zeit*. **1998** 32 , 323.
- [3] a) Hadfield, D., *Permanent Magnets and Magnetism*, Iliffe Books, Ltd. New York, ch. 1. Encyclopedia Britannica. b) A. H. Murrish. In *The physical principles of Magnetism*. Jhon Wiley and Sons, New York **1980**.
- [4] J. S. Miller. *Inorg. Chem.* **2000**. 39 , 4392.
- [5] B. Pilawa. *Ann. Phys.* **1999**. 8 , 191.
- [6] J. S. Miller, A. J. Epstein. *Ang. Chem. Int. Ed.* **1994**. 33 , 385.
- [7] (a) A. Caneschi, D. Gatteschi, R. Sessoli, A. L. Barra, L.C. Brunel, M. Guillot. *J. Am. Chem. Soc.*, **1991**, 113, 5873. (b) D. Gatteschi, R. Sessoli, A. Cornia. *Chem. Commun.* **2000**, 725.
- [8] T. Lis. *Acta Crystallogr.*, **1980**. B36, 2042.
- [9] R. L. Carlin. In *Magnetochemistry*. Springer-Verlag, New York **1986**.
- [10] F.E. Mabbs, D.J. Mchin, *Magnetism and Transition Metal Complexes*, Chapman and Hall, **1973**.
- [11] C.J. O'Connor, *Prog. Inorg. Chem.*, **1982**, 29, 203.
- [12] O. Kahn. In *Molecular Magnetism*. Wiley-WCH Inc., Weinheim **1993** 211.
- [13] C. Kittel, *Introduction to Solid State Physics*, 2nd Ed., J. Willey and Sons, New York, **1953**.
- [14] F. Palacio, *Introduction to physical techniques in molecular magnetism*, University of Zaragoza, Zaragoza **1999**.
- [15] M. Munto, J. G. Segura, J. Campo, M. Nakano, N. Ventosa, D.R. Molina, J. Vaciara. *J. Mat. Chem.* **2006**, 16, 2612.
- [16] L. Thomas, F. Lioni, R. Ballou, D. Gatteschi, R. Sessoli, B. Barbara. *Nature*, **1996** 383, 145.
- [17] (a) G. Aromí, E. K. Brechin. *Struct. Bonding*, **2006**, 122; (b) G. Christou, D. Gatteschi, D. N. Hendrickson, R. Sessoli, *MRS Bull.*, **2000**, 25, 66. (c) D. Gatteschi, R. Sessoli. *Angew. Chem. Int. Ed.* **2003**. 42 , 268 reference therein. (d) R. Sessoli, D. Gatteschi, A. Caneschi,

- M. A. Novak. *Nature*, **1993**, *365*, 141. (e) M. N. Leuenberger, D. Loss. *Nature*, **2001**, *410*, 789
- [18] (a) W. Wernsdorfer, N. A. -Alcalade, D.N. Hendrickson, G. Christou. *Nature*, **2002**, *416*, 406; (b) W. Wernsdorfer, S.Bhaduri, R. Tiron, D.N. Hendrickson and G.Christou. *Phys. Rev. Lett.*, **2002**, *89*, 197201.
- [19] T. Mallah, S. Auberger, C. Verdaguer, P.Veillet *J.Chem.Soc. Chem.Commun.* **1995**, 61-62.
- [20] Z. J. Zhuang, H. Seino, Y. Mizobe, M. Hidai, A. Fujishima, S. Ohkoshi, K. Hashimoto. *J.Am.Chem.Soc.* **2000**, *122*, 2952.
- [21] J. Larionova, M. Gross, M. Pilkington, H. Andres, H. Stoeckli-Evans, H. U. Güdel, S. Decurtins. *Angew.Chem.Int.Ed.Engl.* **2000**, *39*, 1605.
- [22] P. A. Berseth, J. J.Sokol, M. P. Shores, J. L Heinrich, J.R Long. *J.Am.Chem.Soc.* **2000**, *122*, 9655.
- [23] A. M Ako, I. J. Hewitt, V. Mereacre, R. Clerac, W.Wernsdorfer, C.E. Anson, A. K. Powell. *Angew.Chem.Int.Ed.* **2006**, *45*, 4826.
- [24] (a) O. L. Sydora, P. T.Woleczanski, E. B. Lobkovsky. *Angew. Chem., Int. Ed.* **2003**, *42*, 2685 and references cited therein. (b) R. W.Saalfrank, I. Bernt, E. Uller, F. Hampel. *Angew. Chem., Int. Ed. Engl.* **1997**, *36*, 2482. (c) A. Caneschi, A. Cornia, A. C. Fabretti, D. Gatteschi. *Angew. Chem., Int. Ed.* **1999**, *38*, 1295. (d) S. P. Watton, P. L. Fuhrmann, E. Pence, A. Caneschi, A. Cornia,; G. L. Abbati, J. S. Lippard. *Angew. Chem., Int. Ed. Engl.* **1997**, *36*, 2774. (e) C. Can˜ada-Vilalta, T. A. O'Brien, E. K. Brechin, M. Pink, E. R. Davidson, G. Christou. *Inorg. Chem.* **2004**, *43*, 5505. (f) L. F. Jones, D. M. Low, M. Helliwell, J. Raftery, D. Collison, G. Aromi', J. Cano, T. Mallah, W. Wernsdorfer, E. K. Brechin, E. J. L. McInnes. *Polyhedron* **2006**, *25*, 325. (g) H. C. Yao, J. J. Wang, Y. S. Ma, O. Waldmann, W. X. Du, Y. Song, Y. Z. Li, L. M. Zheng, S. Decurtins, X. Q. Xin. *Chem. Commun.* **2006**, 1745.(h) K. L. Taft, C. D. Delfs, G. C. Papaefthymiou, S. Foner, D. Gatteschi, S. J. Lippard. *J. Am. Chem. Soc.* **1994**, *116*, 823. (i) A. Cornia, M. Affronte, A. G. M. Jansen, G. L. Abbati, D. Gatteschi. *Angew. Chem., Int. Ed.* **1999**, *38*, 2264. (j) O. Waldmann, J. Schu˜lein, R. Koch, P. Müller, I. Bernt, R. W. Saalfrank, H. P. Andres, H. U. Güdel, P. Allenspach. *Inorg. Chem.* **1999**, *38*, 5879. (k) O. Waldmann, R. Koch, S. Schromm, J. Schu˜lein, P. Müller, I. Bernt, R. W. Saalfrank, F. Hampel, E. Balthes. *Inorg. Chem.* **2001**, *40*, 2986.

- [25] (a) B. Xu, N. D. Chasteen. *J Biol Chem* **1991**, *266*, 19965. (b) K. L. Taft, G. S. Papaefthymiou, S. J. Lippard. *Science* **1993**, *259*, 1302. (c) S. M. Gorun, G. S. Papaefthymiou, R. B. Frankel, S. J. Lippard. *J. Am. Chem. Soc.* **1987**, *109*, 4244. (d) A. K. Powell. *Struct. Bonding (Berlin)* **1997**, *88*, 1.
- [26] (a) A. L. Feig, S. J. Lippard. *Chem Rev.* **1994**, *94*, 759. (b) E. L. Muetterties, L. J. Guggenberger, *J. Am. Chem. Soc.* **1974**, *96*, 1748. (c) A. W. Addison, T. Nageswara Rao, J. Reedjik, J. van Rijn, G. E. Verschoor, *J. Chem. Soc., Dalton. Trans.*, **1984**, 1349.
- [27] K. Wieghardt, K. Pohl, I. Jibril, G. Huttner. *Angew Chem Int Ed.* **1984**, *23*, 77.
- [28] A. L. Barra, P. Debrunner, D. Gatteschi, C.E. Schulz, R. Sessoli. *Europhys Lett.* **1996**, *35*, 133.
- [29] C. Sangregorio, T. Ohm, C. Paulsen, R. Sessoli, D. Gatteschi. *Phys Rev Lett.* **1997**, 78464.
- [30] D. J. Price, F. Lioni, R. Ballou, P.T. Wood, A.K. Powell. *Philos Trans R Soc Lond Ser A-Math Phys Eng Sci.* **1999**, *357*, 3099.
- [31] J. C. Goodwin, R. Sessoli, D. Gatteschi, W. Wernsdorfer, A. K. Powell, S. L. Heath *J Chem Soc-Dalton Trans.* **2000**, 1835. A. K. Powell, S. L. Heath, D. Gatteschi, L. Pardi, R. Sessoli, G. Spina, F. Del Giallo and F. Pieralli. *J. Am. Chem. Soc.* **1995**, *117*, 2491.
- [32] (a) A. L. Barra, A. Caneschi, A. Cornia, F.F. de Biani, D. Gatteschi, C. Sangregorio, R. Sessoli, L. Sorace. *J Am Chem Soc.* **1999**, *121*, 5302. (b) S. M. Gorun, G. C. Papaefthymiou, R. B. Frankel, S. J. Lippard *J Am Chem Soc.* **1987**, *109*, 3337.
- [33] (a) S. Aime, M. Botta, M. Fasano, E. Terreno. *Chem. Soc. Rev.* **1998**, *27*, 19. b). B.T. Kilbourn. *J. of Metals*, **1988** May, 22. c) J. B. Hedrick. *Ceramic Bulletin.* **1988**, *67*, 858.
- [34] S.S. Bao, L. F. Ma, Y. Wang, L. Fang, C. J. Zhu, Y. Z. Li, L. M. Zheng *Chem. Eur. J.* **2007**, *13*, 2333.
- [35] N. Ishikawa, M. Sugita W. Wernsdorfer. *J. Am. Chem. Soc.* **2005**, *127*, 3650.
- [36] W.S. Liu, T.Q. Jiao, Y.Z. Li, Q.Z. Liu, M.Y. Tan, H. Wang, L.F. Wang. *J. Am. Chem. Soc.* **2004**, *126*, 2280.
- [37] J. Tang, I. Hewitt, N. T. Madhu, G. Chastanet, W. Wernsdorfer, C. E. Anson, C. Benelli, R. Sessoli and A. K. Powell. *Angew. Chem. Int. Ed.* **2006**, *45*, 1729.
- [38] R.E.P. Winpenny. *Adv. Inorg. Chem.*, **2001**, *52*, 1.
- [39] A. M. Ako, I. J. Hewitt, V. Mereacre, R. Clérac, W. Wernsdorfer, C. E. Anson, and A. K. Powell. *Angew. Chem. Int. Ed.*, **2006**, *45*, 4926.

- [40] A. J. Tasiopoulos, A. Vinslava, W. Wernsdorfer, K. A. Abboud, G. Christou. *Angew. Chem. Int. Ed.*, **2004**, *43*, 2117.
- [41] S. S. Bao, L. F. Ma, Y. Wang, L. Fang, C. J. Zhu, Y. Z. Li, L.-M. Zheng *Chem. Eur. J.* **2007**, *13*, 2333.
- [42] A. Messimeri, C. Papadimitriou, C. P. Raptopoulou, A. Escuer, S. P. Perlepes, and A. K. Boudalis. *Inorg. Chem. Commun.*, **2007**, *10*, 800.
- [43] K. A. Thiakou, V. Bekiari, C. P. Raptopoulou, V. Psycharis, P. Lianos, and S. P. Perlepes. *Polyhedron*. **2006**, *25*, 2869.
- [44] H. Nozary, S. Torelli, L. Guénée, E. Terazzi, Gérald Bernardinelli, B. Donnio, D. Guillon, and C. Piguet. *Inorg. Chem.* **2006**, *45*, 2989.
- [45] S. V. Eliseeva, M. Ryazanov, F. Gumy, S. I. Troyanov, L. S. Lepnev, J.-C. G. Bünzli, and N.P. Kuzmina. *Eur. J. Inorg. Chem.* **2006**, 4809.
- [46] G. Novitchi, S. Shova, J. P. Costes, O. Mamula, M. Gdaniec. *Inorg. Chim. Acta*, **2005**, *358*, 4437.
- [47] R. Baggio, R. Calvo, M. T. Garland, O. Peña, M. Pereg, A. Rizzi. *Inorg. Chem.* **2005**, *44*, 8979.
- [48] D. John, W. Urland. *Eur. J. Inorg. Chem.* **2005**, 4486.
- [49] A. M. Atria, R. Baggio, M. T. Garland, J. C. Muñoz, O. Peña. *Inorg. Chim. Acta.* **2004**, *357*, 1997.
- [50] J. P. Costes, J. M. Clemente-Juan, F. Dahan, Fr. Nicodème, M. Verelst. *Angew. Chem. Int. Ed.* **2002**, *41*, 323.
- [51] S. Liu, L. Gelmini, S. J. Rettig, R. C. Thompson, C. Orvig. *J. Am. Chem. Soc.* **1992**, *114*, 6081.
- [52] T. Yi, S. Gao, B. Li. *Polyhedron*. **1997**, *17*, 2243
- [53] R. Baggio, R. Calvo, M. T. Garland, O. Peña, M. Pereg, A. Rizzi. *Inorg. Chem.* **2005**, *44*, 8979.
- [54] J. P. Costes, J. M. Clemente-Juan, F. Dahan, Fr. Nicodème, M. Verelst. *Angew. Chem. Int. Ed.* **2002**, *41*, 323
- [55] H. Hou, G. Li, L. Li, Y. Zhu, X. Meng, Y. Fan. *Inorg. Chem.* **2003**, *42*, 428.
- [56] A. Rohde, W. Urland. *Z. Anorg. Allg. Chem.* **2004**, *630*, 2434.
- [57] A. W. H. Lam, W. T. Wong, S. Gao, G. Wen, and X. X. Zhang. *Eur. J. Inorg. Chem.* **2003**, 149.

- [58] W. P. W. Lai, W. T. Wong, B. K. F. Li, K. W. Cheah. *New J. Chem.* **2002**, *26*, 576.
- [59] N. Ishikawa, M. Sugita, W. Wernsdorfer. *Angew. Chem. Int. Ed.* **2005**, *44*, 2931.
- [60] N. Ishikawa, M. Sugita, T. Ishikawa, S. Koshihara, Y. Kaizu. *J. Am. Chem. Soc.* **2003**, *125*, 8694
- [61] (a) M. Murugesu, A. Mishra, W. Wernsdorfer, K. A. Abboud G. Christou. *Polyhedron* **2006**, *25*, 613. (b) G. W. Urbain, P. Weiss, F. Trombe. *Compte Rendus* **1935**. *200* 2132. (c) M. Sagawa, S. Fujimura, N. Togawa, H. Yamamoto and Y. Matsuura. *J. Applied Physics*. **1984**, *55* 2083 (d) J. J. Croat, J. F. Herbst, R. W. Lee and F. E. Pinkerton. *J. Applied Physics*. **1984**, *55* 2079 (e) G. C. Hadjipanayis, R. C. Hazelton and K. R. Lawless. *J. Applied Physics*. **1984** *55* 2073 (f) J. J. Becker. *J. Applied Physics*. **1984** *55* 2067 (g) N. C. Koon, B. N. Das. *J. Applied Physics*. **1984**. *55* 2063
- [62] (a) A. Mishra, A. J. Tasiopoulos, W. Wernsdorfer, K. A. Abboud, G. Christou. *Inorg. Chem.* **2007**, *46*, 3105. (b) H. Nagel, A. Menth. Goldschmidt. *Informiert.* **1975**, *35* 42. (c) W. E. Wallace, R. S. Craig, H. O. Gupta, S. Hirose, A. Pedziwiatr, E. Oswald, E. Schwab. *IEEE Trans. Magnetics*. **1984**, *20* 1599. (d) M. H. Ghandehari, R. E. Golden and K. L. McNutt. *IEEE Trans. Magnetics*. **1984**. *20* 1611 (e) A. E. Ray, W. A. Soffa, J. R. Blachere and B. Zhang. *IEEE Trans. Magnetics*. **1987**, *23* 2714. (f) M. Sagawa, S. Fujimura, N. Togawa, H. Yamamoto and Y. Matsuura. *J. Applied Physics*. **1984**, *55* 2083
- [63] A. Mishra, W. Wernsdorfer, S. Parsons, G. Christou, E. K. Brechin. *Chem. Commun.* **2005**, 2086.
- [64] A. Mishra, W. Wernsdorfer, K. A. Abboud, G. Christou. *J. Am. Chem. Soc.* **2004**, *126*, 15648.
- [65] C. M. Zaleski, E. C. Depperman, J. W. Kampf, M. L. Kirk, V. L. Pecoraro. *Angew. Chem. Int. Ed.* **2004**, *43*, 3912.
- [66] F. Mori, T. Ishida, T. Nogami. *Polyhedron* **2005**, *24*, 2588.
- [67] T. Hamamatsu, K. Yabe, M. Towatari, S. Osa, N. Matsumoto, N. Re, A. Pochaba, J. Mrozinski, J.-L. Gallani, A. Barla, P. Imperia, C. Paulsen, J.-P. Kappler. *Inorg. Chem.* **2007**, *46*, 4458.
- [68] J.-P. Costes, M. Auchel, F. Dahan, V. Peyrou, S. Shova, W. Wernsdorfer. *Inorg. Chem.* **2006**, *45*, 1924.
- [69] V. Mereacre, A. M. Ako, R. Clérac, W. Wernsdorfer, I. J. Hewitt, C. E. Anson, A. K. Powell. *Chem. Eur. J.* **2008**, *14*, 3577.

- [70] (a) M. Murugesu, A. Mishra, W. Wernsdorfer, K. A. Abboud G. Christou, *Polyhedron* **2006**, 25, 613. (b) G. W. Urbain, P. Weiss, F. Trombe, *Compte Rendus* **1935**, 200 2132. (c) M. Sagawa, S. Fujimura, N. Togawa, H. Yamamoto and Y. Matsuura, *J. Applied Physics*.**1984**, 55 2083 (d) J. J. Croat, J. F. Herbst, R. W. Lee and F. E. Pinkerton, *J. Applied Physics*. **1984**, 55 2079 (e) G. C. Hadjipanayis, R. C. Hazelton and K. R. Lawless, *J. Applied Physics*. **1984** 55 2073 (f) J. J. Becker. *J. Applied Physics*. **1984** 55 2067 (g) N. C. Koon, B. N. Das. *J. Applied Physics*. **1984**.55 2063
- [71] M. Ferbinteanu, T. Kajiwara, K.-Y. Choi, H. Nojiri, A. Nakamoto, N. Kojima, F. Cimpoesu, Y. Fujimura, S. Takaishi, M. Yamashita. *J. Am. Chem. Soc.* **2006**, 128, 9008.
- [72] R.W. Saalfrank, T. Nakajima, N. Mooren, A. Scheurer, H. Maid, F. Hampel, C. Trieflinger, J. Daub. *Eur. J. Inorg. Chem.* **2005**, 1149.
- [73] D. Foguet-Albiol, T.A. O'Brien, W. Wernsdorfer, B. Moulton, M.J. Zaworotko, K.A. Abboud, G. Christou. *Angew. Chem., Int. Ed.* **2005**, 44 897.
- [74] E.M. Rumberger, S.J. Shah, C.C. Beedle, L.N. Zakharov, A.L. Rheingold, D.N. Hendrickson, *Inorg. Chem.* **2005**, 44, 2742.
- [75] E.M. Rumberger, L.N. Zakharov, A.L. Rheingold, D.N. Hendrickson. *Inorg. Chem.* **2004**, 43 6531.
- [76] (a) R.W. Saalfrank, I. Bernt, E. Uller, F. Hampel. *Angew. Chem., Int. Ed.* **1997**, 36 2482 (b) R.W.Saalfrank, C Deutscher,. S. Sperner, T. Nakajima, A.M. Ako, E. Uller, F. Hampel, F. W. Heinemann. *Inorg. Chem.* **2004**, 43, 4372.
- [77] R.W. Saalfrank, I. Bernt, M.M. Chowdhry, F. Hampel, G.B.M. Vaughan, *Chem.Eur. J.* **2001**. 7, 2765.
- [78] R.W. Saalfrank, A. Scheurer, I. Bernt, F.W. Heinemann, A.V. Postnikov, V. Schünemann, A.X. Trautwein, M.S. Alam, H. Rupp, P. Müller. *Dalton Trans.* **2006**, 2865
- [79] D. Foguet-Albiol, K.A. Abboud, G. Christou. *Chem. Commun.* **2005**, 4282.
- [80] B. Biswas, S. Khanra, T. Weyhermüller, P. Chaudhuri. *Chem. Commun.* **2007** 1059.
- [81] T. Kemmitt, N.I. Al-Salim, G.J. Gainsford. *Aust. J. Chem.* **2002**, 55 513.
- [82] T. Kemmitt, L.G. Hubert-Pfalzgraf, G.J. Gainsford, P. Richard. *Inorg. Chem. Commun.* **2005**, 8 1149
- [83] J. Le Bris, L.G. Hubert-Pfalzgraf, S. Daniele, J. Vaissermann, *Inorg. Chem. Commun.* **2007**, 10, 80.

- [84] E. Kh. Lermontova, A. A. Selina, S. S. Karlov, A. V. Churakov, J. A. K. Howard, Y. F. Oprunenko, M. Y. Antipin, J. Sundermeyer, G. S. Zaitseva. *J. Organomet. Chem.* **2006**, *691*, 5710.
- [85] S. Mishra, J. Zhang, L.G. Hubert-Pfalzgraf, D. Luneau, E. Jeanneau. *Eur. J. Inorg.Chem.* **2007**, 602.
- [86] J. Zhang, L. G. Hubert-Pfalzgraf, D. Luneau. *Polyhedron.* **2005**, *24*, 1185.
- [87] a) S. Koizumi, M. Nihei, T. Shiga, M. Nakano, H. Nojiri, R. Bircher, O. Waldmann, S. T. Ochsenbein, H. U. Güdel, F. Fernandez-Alonso, H. Oshio, *Chem. Eur. J.* **2007**, *13*, 8445-8453; b) L. Lecren, W. Wernsdorfer, Y. Li, O. Roubeau, H. Miyasaka, R. Clerac, *J. Am. Chem. Soc.* **2005**, *127*, 11311-11317; c) A. Mishra, W. Wernsdorfer, K. A. Abboud, G. Christou, *J. Am. Chem. Soc.* **2004**, *126*, 15648-15649; d) M. Moragues-Canovas, E. Riviere, L. Ricard, C. Paulsen, W. Wernsdorfer, G. Rajaraman, E. K. Brechin, T. Mallah, *Adv. Mater.* **2004**, *16*, 1101-1105.
- [88] Y.Z. Zheng, Y. Lan, C. E. Anson, A. K. Powell. *Inorg. Chem.* **2008**, *47*, 10813.
- [89] N. N. Greenwood, A. Earnshaw, Chemistry of the elements; Pergamon Press: Oxford, **1985**
- [90] M. L. Kahn, J. P. Sutter, S. Golhen, P. Guionneau, L. Ouahab, O. Kahn, D. Chasseau. *J. Am. Chem. Soc.* **2000**, *122*, 3413.
- [91] J. H. van Vleck, The Theory of Electric and Magnetic Susceptibility, Oxford University Press, **1932**.
- [92] K. Kambe. *J. Phys. Soc. Jpn.* **1950**, *5*, 48.
- [93] C. Benelli, D. Gatteschi, *Chem. Rev.* **2002**, *102*, 2369.
- [94] G. Abbas, Y. Lan, G. Kostakis, C. E. Anson, A. K. Powell. *Inorg. Chim. Acta* **2008**, *361*, 3494.
- [95] T. Ellis, M. Glass, A. Harton, K. Felting, J. C. Huffman, J. B. Vincent. *Inorg. Chem.* **1994**, *33*, 5522.
- [96] R. Bagai, K. A. Abboud, G. Christou. *Dalton Trans.* **2006**, 3306.
- [97] A. M. Ako, V. Mereacre, I. J. Hewitt, R. Clérac, L. Lecren, C. E. Anson, A. K. Powell, *J. Mater. Chem.* **2006**, *16*, 2579.
- [98] T. C. Stamatatos, A. K. Boudalis, Y. Sanakis, C. P. Raptopoulou. *Inorg. Chem.* **2006**, *45*, 7372.

- [99] A. K. Boudalis, N. Lalioti, G. A. Spyroulias, C. P. Raptopoulou, A. Terzis, A. Bousseksou, V. Tangoulis, J.-P. Tuchagues, S. P. Perlepes. *Inorg. Chem.* **2002**, *41*, 6474.
- [100] Z. Xie, S. Wang, Q. Yang, T. C. W. Mak. *Organometallics* **1999**, *18*, 1578.
- [101] R. Anwender, F. C. Munck, T. Priermeier, W. Scherer, O. Runte, W. A. Herrmann. *Inorg. Chem.* **1997**, *36*, 3545.
- [102] M. L. Kahn, R. Ballou, P. Porcher, O. Kahn, J. P. Sutter, *Chem. Eur. J.* **2002**, *8*, 525.
- [103] E. L. Muetterties, L. J. Guggenberger. *J. Am. Chem. Soc.* **1974**, *96*, 1748.
- [104] M. G. B. Drew. *Coord. Chem. Rev.* **1977**, *24*, 179.
- [105] (a) C. Aronica, G. Pilet, G. Chastanet, W. Wernsdorfer, J.-F. Jacquot, D. Luneau. *Angew. Chem.* **2006**, *118*, 4775.(b) V. Chandrasekhar, B. M. Pandian, R. Azhakar, J. J. Vittal, R. Clérac, *Inorg. Chem.* **2007**, *46*, 5140.(c) V. Mereacre, A. M. Ako, R. Clérac, W. Wernsdorfer, I. J. Hewitt, C. E. Anson, A. K. Powell. *Chem. Eur. J.* **2008**, *14*, 3577.
- [106] W Anthony, Addison, T. Nageswara Rao, J. Reedijk, J. v. Rijn, G. C. Verschoor, *Dalton Trans.* **1984**, 1349.
- [107] WinX^{Pow} 1.07, Stoe & Cie GmbH, Darmstadt, 2000.
- [108] G.M. Sheldrick, SHELXTL 5.1, Bruker AXS Inc., Madison, WI, USA **1997**.
- [109] *Theory and application of Molecular Paramagnetism*, E. A. Bordeaux, L.N. Mullay, Eds, John Willey & Sons, New York, **1976**.

Appendix A: List of inorganic compounds

- 1 [La₂^{III}(mdeaH₂)(piv)₆]
- 2 [Ce₂^{III}(mdeaH₂)(piv)₆]
- 3 [Pr₂^{III}(mdeaH₂)(piv)₆]
- 4 [Nd₂^{III}(mdeaH₂)(piv)₆]
- 5 [Sm₂^{III}(mdeaH₂)(piv)₆]
- 6 [Gd₂^{III}(mdeaH₂)(piv)₆]
- 7 [Tb₄^{III}(μ₃-OH)₂(mdeaH)₂(piv)₈]
- 8 [Dy₄^{III}(μ₃-OH)₂(mdeaH)₂(piv)₈]
- 9 [Ho₄^{III}(μ₃-OH)₂(mdeaH)₂(piv)₈]
- 10 [Er₄^{III}(μ₃-OH)₂(mdeaH)₂(piv)₈]
- 11 [Tm₄^{III}(μ₃-OH)₂(mdeaH)₂(piv)₈]
- 12 [Tb₄^{III}(mdea)₂(mdeaH)₂(PhCO₂)_{4.5}(NO₃)_{1.5}]
- 13a [Dy₄^{III}(mdea)₂(mdeaH)₂(PhCO₂)₆]·4MeCN (**13a**)
- 13b [Dy₄^{III}(mdea)₂(mdeaH)₂(PhCO₂)₆]·0.3mdeaH₂·1.7MeCN·1.4H₂O
- 13c [Dy₄^{III}(mdea)₂(mdeaH)₂(PhCO₂)₆]·3MeCN
- 14 [Ho₄^{III}(mdea)₂(mdeaH)₂(PhCO₂)_{4.5}(NO₃)_{1.5}]
- 15 [Er₄^{III}(mdea)₂(mdeaH)₂(PhCO₂)₆]·0.3mdeaH₂·1.7MeCN·1.4H₂O
- 16 [Gd₃^{III}Fe₇^{III}(μ₄-O)₂(μ₃-OH)₂(N₃)₆(mdea)₇(PhCO₂)₄]·5MeCN
- 17 [Tb₃^{III}Fe₇^{III}(μ₄-O)₂(μ₃-OH)₂(N₃)₆(mdea)₇(PhCO₂)₄]·5MeCN
- 18 [Dy₃^{III}Fe₇^{III}(μ₄-O)₂(μ₃-OH)₂(N₃)₆(mdea)₇(PhCO₂)₄]·7MeOH
- 19 [Er₃^{III}Fe₇^{III}(μ₄-O)₂(μ₃-OH)₂(N₃)₆(mdea)₇(PhCO₂)₄]·5MeOH
- 20 [Ho₄^{III}Fe₆^{III}(μ₃-OH)₄(mdea)₆(mdeaH)₂(N₃)₈(PhCO₂)₄(OH₂)₂]·4MeCN
- 21 [Er₄^{III}Fe₆^{III}(μ₃-OH)₄(mdea)₆(mdeaH)₂(N₃)₈(PhCO₂)₄(OH₂)₂]·4MeCN
- 22 [Tm₄^{III}Fe₆^{III}(μ₃-OH)₄(mdea)₆(mdeaH)₂(N₃)₈(PhCO₂)₄(OH₂)₂]·4MeCN
- 23 [Er^{III}Fe₄^{III}(μ₃-O)(Mdea)₃(MdeaH)(O₂CPh)₂(N₃)₄]

Appendix B: List of organic compounds

N-methyldiethanolamine

Pivalic acid

Benzoic acid

Appendix C: List of abbreviations

mdeaH ₂	<i>N</i> -methyldiethanolamine
pivH	Pivalic acid
PhCO ₂ H	Benzoic acid
Me	Methyl
MeOH	Methanol
MeCN	Acetonitrile
mg	milligram
ml	milliliter
mmol	millimole
IR	infrared
SQUID	super-conducting quantum interference device
ac	alternating current
dc	direct current
D	zero-field splitting parameter
K	Kelvin
Oe	Ørsted
<i>H</i>	magnetic field
Hz	Hertz
<i>M</i>	magnetisation
<i>T</i>	temperature
T	tesla
HS	high spin
T _c	critical temperature
h	hour
χ	molar magnetic susceptibility
χ'	in-phase magnetic susceptibility
χ''	out-of-phase magnetic susceptibility
μ_B	bohr magneton
U_{eff}	effective energy barrier
cm ³	cubic centrimeters

SMM	Single Molecule Magnet
Ln	Lanthanide

Appendix D: List of figures

Fig. 1.1	The alignment of magnetic moments (a) ferromagnets, (b) antiferromagnets and (c) for ferrimagnets.	5
Fig. 1.2	(a) The plot of χT and (b) the plot of $1/\chi$ as a function of Temperature for paramagnetic, ferromagnetic, antiferromagnetic and ferrimagnetic materials.	7
Fig. 1.3	The plot of magnetic susceptibility as a function of temperature for paramagnetic, ferromagnetic, antiferromagnetic materials.	7
Fig. 1.4	Structure of $[\text{Mn}_{12}\text{O}_{12}(\text{CH}_3\text{COO})_{16}(\text{H}_2\text{O})_4] \cdot 2\text{CH}_3\text{COOH} \cdot 4\text{H}_2\text{O}$. ^[8] Colour code: blue Mn^{3+} , green Mn^{4+} red oxygen, grey carbon and white hydrogen.	9
Fig. 1.5	Energy diagram showing the relative positions of the zero-field split M_S levels of an $S_T = 10$ system, and the barrier mediating between the $M_S = +10$ and the $M_S = -10$ states	10
Fig. 1.6	The magnetic hysteresis loops of Mn12-Ac are shown at the indicated temperatures. ^[16]	10
Fig.1.7	An example of ac susceptibility measurements as a function of temperature at different frequencies, and as a function of frequency at different temperatures (a, c) in-phase and (b, d) out-of-phase signals.	11
Fig. 1.8	An example of τ versus $1/T$ plot obtained from both temperature and frequency dependent ac susceptibility measurements under zero dc field.	12
Fig. 1.9	$[\text{Fe}_8\text{O}_2(\text{OH})_{12}(\text{tacn})_6]^{8+}$ (left). Hydrogen atoms are omitted for clarity and tacn = 1,4,7-triazacyclononane. Magnetic studies (right).	15
Fig. 1.10	$[\text{Fe}_{19}(\text{metheidi})_{10}(\text{OH})_4\text{O}_6(\text{H}_2\text{O})_{12}](\text{NO}_3)$ (left). Hydrogen atoms are omitted for clarity and metheidi = <i>N</i> -(1-Hydroxymethylethyl) iminodiacetic acid. Magnetic studies (right)	16

Fig. 1.11	[Fe ₄ (OMe) ₆ (dpm) ₆] (left). Hydrogen atoms are omitted for clarity and dpm = dipivaloylmethane. Magnetic studies (right).	17
Fig. 1.12	TBA[(Pc) ₂ Tb _{0.02} Y _{0.98}] (left). Hydrogen atoms are omitted for clarity and Pc = phthalocyanine. Magnetic studies (right).	19
Fig. 1.13	[Dy ₃ (μ ₃ -OH) ₂ L ₃ Cl(H ₂ O) ₅]Cl ₅ ·19H ₂ O (left). Hydrogen atoms are omitted for clarity. Magnetic studies (right).	19
Fig. 1.14	[Fe ₂ Ho ₂ (OH) ₂ (teaH) ₂ (O ₂ CPh) ₆] (left). Hydrogen atoms are omitted for clarity and tea = triethanolamine. Magnetic studies were carried out for Dy analogue (right).	21
Fig. 1.15	Structure of [Fe(bpca)(μ-bpca)Dy(NO ₃) ₄] (left). Hydrogen atoms are omitted for clarity and bpca = bis(2-pyridylcarbonylamine). Magnetic studies (right).	22
Fig. 1.16	Coordination modes of ligand mdeaH ₂ (mode I ^[81–85, 87, 90, 91] , mode II ^[88] , mode III ^[86, 92] , mode IV ^[80] , mode V ^[93] , mode VI ^[81, 87, 89] , mode VII ^[89] , mode VIII ^[89] , mode IX ^[89, 94] , mode X ^[92])	23
Fig. 1.17	Common coordination modes of the carboxylate group.	24
Fig. 3.1	Crystal structure of [Pr ₂ (mdeaH ₂) ₂ (piv) ₆] (3). Methyl groups corresponding to the minor disorder component of the two pivalate ligands and all H atoms are omitted for clarity. Grey, red, blue, and green spheres represent C, O, N and Pr, respectively.	29
Fig. 3.2	X-ray powder diffraction: (a) calculated for 3 based on the single crystal X-ray structure; (b) measured for complex 2 .	30
Fig. 3.3	The 2D supramolecular structure for 3 showing the hydrogen bonds in red dotted lines.	30
Fig. 3.4	Temperature dependence of χT product for 1–6 at 1000 Oe.	32
Fig. 3.5	Temperature dependence of the χT product for compound (Gd ₂) 6 at 1000 Oe; Inset: the fit of the Brillouin function to the M versus H/T data of compound 6 . The red solid line is the best fit; the dots are the experimental data	33
Fig. 3.6	Molecular structure of 8 . lavender, red, blue and grey spheres represent Dy, O, N and C, respectively. All H atoms are omitted for clarity.	35
Fig. 3.7	The structure of the [Ln ^{III} ₄ (μ ₃ -OH) ₂] ¹⁰⁺ butterfly core in 8 , which lies	

	on an inversion center. Dy(1) and Dy(1') represent “body” sites and Dy(2) and Dy(2') “wingtip” sites.	37
Fig. 3.8	Temperature dependence of the χT products for compounds 7–11 at 1000 Oe.	38
Fig. 3.9	Field dependence of magnetisation at indicated temperatures for compound 7.	39
Fig. 3.10	Field dependence of the magnetisation at indicated temperatures for 8.	39
Fig. 3.11	Field dependence of magnetisation at indicated temperatures for compound 9.	39
Fig. 3.12	Field dependence of magnetisation at indicated temperatures for compound 10.	40
Fig. 3.13	Field dependence of magnetisation at indicated temperatures for compound 11.	40
Fig. 3.14	Temperature dependence of the in-phase (left) and out-of-phase (right) components of the ac magnetic susceptibility, for 8 under zero dc field.	41
Fig. 3.15	Frequency dependence of the in-phase (left) and the out-of-phase (right) ac susceptibility component at different temperature for compound 8 under zero dc field.	41
Fig. 3.16	τ versus $1/T$ plot for 8 obtained from frequency dependent ac susceptibilities under zero dc field.	41
Fig. 3.17	Frequency dependence at 1.8 K of the in-phase (left) and the out-of-phase (right) ac susceptibility components at different dc fields for 8.	42
Fig. 3.18	Frequency dependence at 1.8 K of the in-phase (left) and the out-of-phase (right) ac susceptibility components at different dc fields for 8.	43
Fig. 3.19	τ versus $1/T$ plot for 8 under 800 Oe dc field obtained from Fig. 3.18.	43
Fig. 3.20	X-ray powder diffraction: for 13 based on the single crystal X-ray structure.	44
Fig. 3.21	Structure of compound 13a. Grey, red, blue and lavender spheres represent C, O, N and Dy, respectively.	46
Fig. 3.22	The structure of the Dy ₄ ^{III} core of 13a.	47
Fig. 3.23	Temperature dependence of the χT products for compounds	

	14–17 at 1000 Oe.	48
Fig. 3.24	Field dependence of magnetisation at indicated temperatures for compound 12 .	49
Fig. 3.25	Field dependence of magnetisation at indicated temperatures for compound 13 .	49
Fig. 3.26	Field dependence of magnetisation at indicated temperatures for compound 14 .	50
Fig. 3.27	Field dependence of magnetisation at indicated temperatures for compound 15 .	50
Fig. 3.28	Temperature dependence of the in-phase (left) and out-of-phase (right) components of the ac magnetic susceptibility for 12 under zero dc field.	51
Fig. 3.29	Temperature dependence of the in-phase (left) and out-of-phase (right) components of the ac susceptibility for 13 under zero dc field. components of the ac magnetic susceptibility under zero dc field for 15 .	51
Fig. 3.30	Frequency dependence of the in-phase (left) and the out-of-phase (right) ac susceptibility components at different temperature for compound 13 under zero dc field.	52
Fig. 3.31	τ versus $1/T$ plot for 13 obtained from frequency dependent ac susceptibility measurements under zero dc field.	52
Fig. 3.32	Frequency dependence at 1.8 K of the in-phase (left) and the out-of-phase (right) ac susceptibility components at different dc fields for 12 .	53
Fig. 3.33	Frequency dependence at 2 K of the in-phase (left) and the out-of-phase (right) ac susceptibility components at different dc fields for 13 .	53
Fig. 3.34	Frequency dependence at 7 K of the in-phase (left) and the out-of-phase (right) ac susceptibility components at different dc fields for 13 .	53
Fig. 4.1	Structure of $[\text{Dy}_3^{\text{III}}\text{Fe}_7^{\text{III}}(\mu_4\text{-O})_2(\mu_3\text{-OH})_2(\text{N}_3)_6(\text{mdea})_7(\text{PhCO}_2)_4]$ in 18 . Hydrogen atoms are omitted for clarity. Grey, red, blue, green and lavender spheres represent C, O, N, Fe and Dy, respectively.	59
Fig. 4.2	Structure of the $[\text{Dy}_3^{\text{III}}\text{Fe}_7^{\text{I,II}}(\mu_4\text{-O})_2(\mu_3\text{-OH})_2]^{24+}$ core in the cluster of 18 .	59
Fig. 4.3	Temperature dependence of the χT products for compounds 16–19 at 1000 Oe.	60
Fig. 4.4	Field dependence of magnetisation at indicated temperatures	

	for compound 16 .	61
Fig. 4.5	Field dependence of magnetisation at indicated temperatures for compound 17 .	62
Fig. 4.6	(a) Field dependence of magnetisation at indicated temperatures for compound 18 (left). (b) Hysteresis measurements of compound 18 at 1.8 K with a sweeping rate of 0.002 T/s. (right).	63
Fig. 4.7	Plot of dM/dH versus H for compound 18 ..	63
Fig. 4.8	Field dependence of magnetisation at indicated temperatures for compound 19 .	63
Fig. 4.9	Plot of dM/dH versus H for compound 19 .	64
Fig. 4.10	Temperature dependence of the in-phase (left) and out-of-phase (right) components of the ac magnetic susceptibility for 17 under zero dc field.	65
Fig. 4.11	Frequency dependence at 1.8 K of the in-phase (left) and the out-of-phase (right) ac susceptibility component at different dc fields for 17 .	65
Fig. 4.12	Temperature dependence of the in-phase (left) and out-of-phase (right) component of the ac magnetic susceptibility for 18 under zero dc field.	66
Fig. 4.13	Frequency dependence of the in-phase (left) and out-of-phase (right) ac susceptibility component at different temperatures for 18 under zero dc field.	66
Fig. 4.14	τ versus $1/T$ plot for 18 obtained from both temperature- and frequency-dependent ac susceptibility measurements under zero dc field.	66
Fig. 4.15	Frequency dependence of the in-phase (left) and the out-of-phase (right) ac susceptibility components at 3.8 K at different dc fields for 18 .	67
Fig.4.16	Magnetization (M) versus applied dc field (H) hysteresis loops for single crystals of 18 at the indicated temperatures and a fixed sweep rate of 0.035 T/s. The magnetization is normalized to its saturation value M_s .	68
Fig. 4.17	Magnetization (M) vs time decay plots in zero dc field for a single crystal of 18 . The The magnetization is normalized to its saturation value M_s .	68
Fig. 4.18	Arrhenius plot of the relaxation time (τ) versus $1/T$ for a single crystal of 18 using data obtained from ac susceptibility and the dc magnetization decay measurements of Fig. 4.17. The dashed line is the fit of data in the thermally	

	activated region to the Arrhenius equation; see the text for the fit parameters.	69
Fig. 4.19	Molecular structure of $[\text{Fe}_6^{\text{III}}\text{Tm}_4^{\text{III}}(\mu_3\text{-OH})_4(\text{mdea})_6(\text{mdeaH})_2(\mu\text{-benzoate})_4(\text{N}_3)_8(\text{OH}_2)_2]$. Organic H atoms and minor disorder components omitted for clarity; intramolecular hydrogen-bonds are shown as dotted lines.	70
Fig. 4.20	Two views of the structure of the core of $[\text{Fe}_6^{\text{III}}\text{Tm}_4^{\text{III}}(\mu_3\text{-OH})_4(\text{mdea})_6(\text{mdeaH})_2(\mu\text{-benzoate})_4(\text{N}_3)_8(\text{OH}_2)_2]$. Azide and benzoate ligands, and C-H hydrogen atoms, omitted for clarity.	71
Fig. 4.21	Temperature dependence of the χT product at indicated applied magnetic fields for 20-22 .	72
Fig. 4.22	Field dependence of magnetisation at indicated temperatures for 20 .	73
Fig. 4.23	Field dependence of magnetisation at indicated temperatures for compound 21 .	74
Fig. 4.24	Field dependence of magnetisation at indicated temperatures for 22 .	74
Fig. 4.25	Temperature dependence of the in-phase (left) and out-of-phase (right) components of the ac magnetic susceptibility, for 20 under zero dc field.	75
Fig. 4.26	The molecular structure of $[\text{Er}^{\text{III}}\text{Fe}_4^{\text{III}}(\mu_3\text{-O})(\text{mdea})_3(\text{mdeaH})(\text{O}_2\text{CPh})_2(\text{N}_3)_4] \cdot 2.5\text{MeCN}$ (23). Hydrogen atoms are omitted for clarity. Grey, red, dark blue, green and pale blue spheres represent C, O, N, Fe and Er, respectively.	76
Fig. 4.27	Structure of the core of $[[\text{Fe}_4^{\text{III}}\text{Er}^{\text{III}}(\mu_4\text{-O})(\text{mdea})_3(\text{mdeaH})(\mu\text{-benzoate})_2(\text{N}_3)_4]$. Azide and benzoate ligands, and C-H hydrogen atoms, omitted for clarity.	77
Fig. 4.28	Temperature dependence of χT product for compound 23 .	78
Fig. 4.29	Field dependence of magnetization at indicated temperatures for compound 23 .	79
Fig. 4.30	Plot of dM/dH versus H for compound 23 .	79

Appendix E: List of tables

Table 3.1	Selected bond distances (Å) for complexes of compounds 3 and 6 .	31
Table 3.2	Comparison of the χT products at room temperature between the expected ^[93] and the experimental values for compounds 1-6 .	33

Table 3.3	Selected distances (Å) and bond angles (°) for the cores of compounds 7–11 .	36
Table 3.4	Comparison of the dc magnetic data for compounds 7-11 .	38
Table 3.5	Unit cell measurements of compounds 12-15 .	47
Table 3.6	Comparison of the dc magnetic data for compounds 12-15 .	48
Table 4.1	Unit cell measurements of compound 16-19 .	60
Table 4.2	Comparison of dc magnetic data for compounds 16-19 .	62
Table 4.3	Unit cell measurements of compound 20-22 .	72
Table 4.4	Comparison of the magnetic data for compounds 20-22 .	75
Table 4.5	Selected bond lengths (Å) of compound 23 .	77

Appendix F: List of schemes

Scheme 1.	ML ₅ five coordinate geometry complex	15
Scheme 2	The synthetic route from Ln(NO ₃) ₃ ·6H ₂ O to compounds 3-8, 9-13 and 14-17 .	55
Scheme 3	The synthetic route of compounds 16-19, 20-22 and 23 .	81

ACKNOWLEDGEMENTS

I feel great pleasure in expressing my ineffable thanks to my ever encouraging and inspirational, supervisor **Prof. Dr. Annie. K. Powell**. Her personal interest thought provoking guidance, valuable suggestions and discussions enabled me to complete this tedious work. She really encouraged all my attempts during this research work.

I am also thankful to **Dr. Chris Anson** for undertaking all of the intricate crystallographic measurements and data solving. I would also like to thank him for thought provoking discussions and valuable suggestions.

I would like to thank Dr. Yanhua Lan for performing the SQUID measurements of all the compounds and for their magnetic studies, also to Dr. Wolfgang Wernsdorfer for magnetic interpretations. My special thanks to Dr. Lianne Beltran and Dr. Valeriu mareacre whose suggestions enabled me to present my results in the best possible way.

A deep sense of gratitude and indefinable thanks are owed to Dr. George E. Kostakis for being a great friend. He gave me main inspirational and useful tips in writing manuscripts.

Thanks are due to Getraud Amschlinger for all her help and great cooperation in official matters. Thanks to Rolf Lehman for technical assistance. I am also thankful to Dr. H. Henke for his valuable suggestions and garden parties which are memorable events during my stay in Karlsruhe. At university Karlsruhe, i am thankful to Fr.S. Lude for providing elemental analysis, Fr. G. Kuhn Frau S. Böcker for their help in chemical stores.

I would like to thank all group members for giving friendly environment and support.

The acknowledgement may remain incomplete if I don't mention very special friends Dr. Usman Anwar, Kartik Mondal, Salman Ahmad, Zeeshan Majeed and Sven for their wonderful company throughout this period.

This all is the fruit of untiring efforts, lot of prayers, encouragement and guidance of my loving parents. I have no words to explain the encouragement and financial support of my respectable brother. I have to thank my life partner for her encouragement and patience. Special thanks to all friends, relatives and well wishers who remember me in their prayers.

Curriculum Vitae

Ghulam Abbas

Insterburger Str.02, Z# 113

76139 Karlsruhe

Date of Birth 02-01-1977
Place of Birth Sialkot, Pakistan
Nationality Pakistani
Marital status Married

Education 1982-1987 Primary school Gopal Pur, Sialkot.
1987-1992 Comprehensive school, sialkot.
1992-1994 Govt. Murray College, Sialkot.

1997-1999 B.Sc in Chemistry
Govt. College, Lahore.

2000-2002 M.Sc in Chemistry
Quaid-I-Azam University Islamabad.

2002-2004 M.Phil in Chemistry
Quaid-I-Azam University Islamabad

Jan.2006-Apr.2009 Ph.D in Chemistry
University Of Karlsruhe(TH) Germany
Supervisor: Prof. Dr. Annie K. Powell

Publications

Ghulam Abbas, Yanhua Lan, George Kostakis, Christopher E. Anson, Annie K. Powell. *An investigation into lanthanide-lanthanide magnetic interactions in a series of [Ln₂(mdeaH₂)₂(piv)₆] dimers.* *Inorganica Chimica Acta* **2008**, 361, 3494-3499.

Rare earth metal complexes: A systematic study on the heavier lanthanide series reveal the formation of tetramers $[Ln_4(\mu_3-OH)_2(mdeaH)_2(piv)_8]$, possessing a butterfly core with a SMM behavior for the Dy compound. Ghulam Abbas, George E. Kostakis, Yanhua Lan, Wolfgang Wernsdorfer, Christopher E. Anson, and Annie K. Powell to be submitted.

Poster Presentation

Karlsruhe-Strasbourg bilateral meetings on progress in Supramolecular Chemistry (5 Dec.2008). **G. Abbas.** *An Approach Towards Rare Earth Nanomagnets.*

The search For New Molecular Based Magents Containing Vanadium.

International Karlsruhe Nanoscience Workshop (Oct.8-10, 2007)

G.Abbas, M.U.Anwar R.Kania, S.Mukherjee, C. Anson and Annie.K.Powell

Conferences attended

- 2008** 1st Chemical Link Karlsruhe-Strasbourg Strasbourg, France. Karlsruhe-Strasbourg bilateral meetings on progress in Supramolecular Chemistry June 9th 2008. **Oral Presentation** on “An approach towards rare earth nanomagnets.”
- 2007** International Karlsruhe Nanoscience Workshop Oct.8-10.
- 2006** European Conference on Molecular Magnetism (ECMM) Oct.10-15
Tomar, Portugal.

